Morphology and Thermal Behavior of Single Crystals of Polystyrene-Poly(ethylene oxide) Block Copolymers

Houssam Hamie

Morphology and Thermal Behavior of Single Crystals of Polystyrene-Poly(ethylene oxide) Block Copolymers

Houssam Hamie

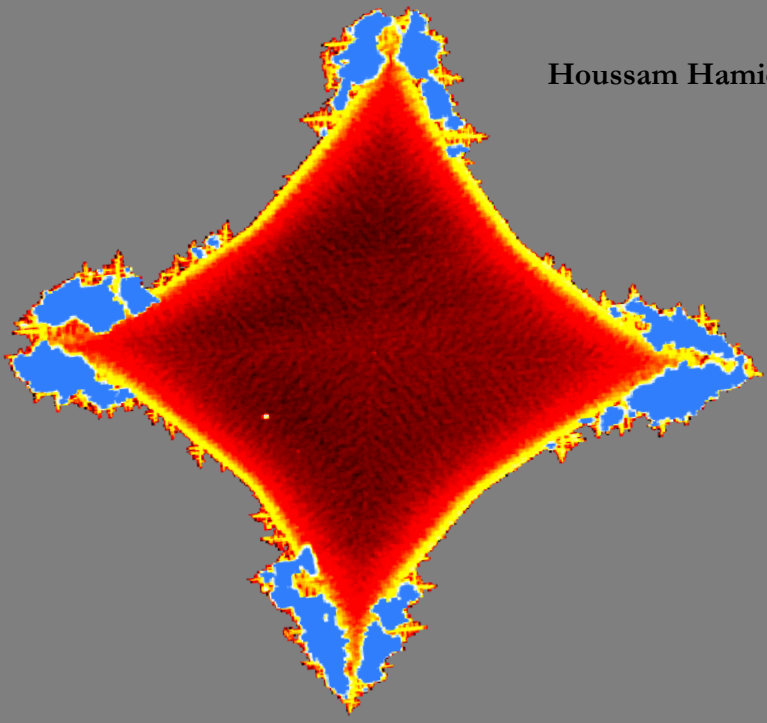

Mulhouse 2010

UNIVERSITÉ DE HAUTE ALSACE

Morphology and Thermal Behavior of Single Crystals of Polystyrene-Poly(ethylene oxide) Block Copolymers

Houssam Hamie

A dissertation submitted to the graduate faculty in partial fulfillment of the requirements for the degree of

DOCTOR OF PHILOSOPHY

Mulhouse 2010

Mulhouse, 2010

THÈSE
Présentée pour obtenir le titre de

DOCTEUR DE L'UNIVERSITÉ DE HAUTE-ALSACE

Spécialité :
Chimie des Matériaux

Par
Houssam HAMIE

Sujet:

Morphology and Thermal Behavior of Single Crystals of Polystyrene-Poly(ethylene oxide) Block Copolymers

Composition du jury:

Prof. T. EZQUERRA : Rapporteur
Dr. O.V. BORISOV : Rapporteur
Prof. N. GOSPODINOVA : Examinateur
Prof. T. HAMIE : Examinateur
Dr. D.A. IVANOV : Promoteur

For my Father

And my Mother

Preface

Along the history of human thinking, science has always been a tool to deepen the basic understanding of the surrounding world while ensuring the dissemination of the acquired knowledge and continuity. The progress in this direction was always associated with the search for and availability of new materials. The actual 21th century reveals the quest of materials science for smaller and smaller functional objects aiming at miniaturization and intelligence of materials suited for a wide range of applications from biology to telecommunications. It's the Nano century.

The Nano century needs continuously improving measurements tools, as the materials science develops simultaneously and the novel materials allow new advanced techniques to emerge, and the cycle continues, and powerful new techniques make it possible to continuously review the previously acquired knowledge aiming at better understanding.

In the general philosophical context, this work can be viewed as a part of this global development, targeting fine

measurements at the nanoscale and understanding the structure and thermal behavior of materials.

Single crystals of polystyrene-poly(ethylene oxide), PS-*b*-PEO, were studied as early as in the 60's, starting with the work by *Lotz* and *Kovacs* from the Institut Charles Sadron in Strasbourg. These researchers pioneered the research on single crystals of crystalline-amorphous block copolymers, for which the interaction of the amorphous and crystallizable blocks could be specifically addressed contributing to the general understanding of the molecular mechanisms of polymer crystallization.

Our work benefited from the capacity of the Atomic Force Microscopy (AFM) technique invented in the mid 80's and since then extensively applied to polymer materials. This technique continues to reveal its great universality by the simple way and capacity to monitor the *in-situ* behavior of materials under controlled conditions of atmosphere and temperature. However, AFM still remains an essentially surface characterization technique, and therefore is not designed to probe the interior structure of materials. For this purpose, the X-ray scattering techniques are of interest to probe the materials bulk structure from the Angstrom to

nanometer range being applicable for different sample environments such as solutions, real-time heating, fiber melt-spinning, hot molding and many others. The high brilliance of the third generation of synchrotron sources such as the ESRF and the development of new detection and acquisition tools makes it possible to monitor in a fraction of a second the materials structural evolution in order to address the process kinetics and propose accurate models accounting for the mechanisms of structural transitions.

This work has been focused on the semicrystalline morphology and morphological evolution of single crystals of PS-*b*-PEO. By monitoring the semicrystalline morphology in static conditions but also in the course of heating ramps, we attempted to reveal the role of the amorphous block in the structure formation and thermal behavior of these crystals. In this work, the *in-situ* AFM and temperature-controlled simultaneous small- and wide-angle X-ray scattering techniques were mainly used. These two techniques, despite their differences, nicely complemented each other providing a wealth of structural information and eventually contributing to our understanding of these complex systems.

Tables of contents

Glossary

Abbreviations, Acronyms and Symbols

N	Degree of polymerization within a polymer chain
PE	**P**oly(**E**thylene)
PEO	**P**oly(**E**thylene **O**xide)
PS	**P**oly(**S**tyrene)
PS-b-PEO	**P**oly(**S**tyrene)-*block*-**P**oly(**E**thylene **O**xide)
IF	**I**ntegral **F**olding
NIF	**N**on **I**ntegral **F**olding
FC	**F**olded **C**hain crystal
EC	**E**xtended **C**hain crystal
$\boldsymbol{ODT}$	**O**rder **D**isorder **T**emperature
ΔG	Gibbs free energy change
hkl	Miller indices
(hkl)	Miller indices for a given plane
{hkl}	Miller indices for a set of equivalent planes
[hkl]	Miller indices for directive axis
$\boldsymbol{T_c}$	Crystallization temperature
$\mathbf{P2_1/a\text{-}C2h^5}$	Space group of crystalline poly(ethylene oxide)
$\boldsymbol{T_d}$	Dissolution temperature in a given solvent
$\boldsymbol{T_d^0}$	Equilibrium dissolution temperature
$\boldsymbol{\Delta T}$	Degree of supercooling in a given solvent $\Delta T = T_d^0 - T_c$
$\boldsymbol{\sigma_e}$	Fold surface energy
$\boldsymbol{\Delta H_d}$	Enthalpy of dissolution in a given solvent

ΔH_m	Enthalpy of melting in the bulk
T_m	Melting temperature in the bulk
T_g	Glass transition temperature
T_m^0	Equilibrium melting temperature
ΔS	Entropy
N_A	Avogadro's number
ρ_{PEO}^c	PEO crystal density
ρ_{PEO}^a	PEO amorphous density
ρ_{PEO}	Average PEO density accounting for crystalline and amorphous fractions
ρ_{PS}	PS density
L_B	Overall lamellae thickness, measured from SAXS long period
L_c	PEO crystal thickness, measured from 1D CF & IDF
L_a	Amorphous thickness, measured from 1D CF & IDF
L_f	Length of one fold
L	Contour length of PEO chain
L_u	Length of one monomer of PEO $-[CH_2-CH_2-O-$
ε	amorphous over crystalline PEO length Ratio
M_u^{PEO}	Mass of one monomer $-[CH_2-CH_2-O]-$
M_n^{PEO}	Number average molecular weight of PEO
M_n^{PS}	Number average molecular weight of PS
M_{fold}	Mass of one fold

$M_{crystal}^{PEO}$	Mass of crystalline stem of PEO
M_{fold}^{PEO}	Mass of one fold of PEO at the crystalline surface
M_{cilia}^{PEO}	Mass of one PEO cilia
ν_c	Volume fraction of PEO crystal over the total volume of diblock
ν_a	Volume fraction of PS over the total volume of diblock
W_{PEO}	Weight fraction of PEO
W_{PS}	Weight fraction of PS
σ	Tethering density of PS brush
$\mathbf{n}$	Degree of folding
V^{PS}	Volume of amorphous PS
V_c^{PEO}	Volume of crystalline PEO
V_a^{PEO}	Volume of amorphous PEO
$\emptyset_c$	Volume crystallinity
$\emptyset_l$	Linear crystallinity deduced from 1D CF or IDF
χ_c	Weight crystallinity
S	Lamellae basal surface
$\mathbf{A_n}$	Lamella basal surface occupied by one chain folded n times
$\mathbf{A_s}$	Lamella basal surface occupied by one PEO site
$\mathbf{A_0}$	Lamella basal surface occupied by one unit cell of crystalline PEO
$\mathbf{a, b, c}$, $\boldsymbol{\beta}$	Parameters of the PEO unit cell

Chapter I Literature Review

In this chapter, we review the classical theories of polymer crystallization and describe the effect of thermal annealing on the semicrystalline morphology. Due to its wide acceptance, the Lauritzen-Hoffman theory of polymer crystallization is presented in some detail. The crystallization/melting process of polymer crystals is considered using the Gibbs-Thomson plots. The mechanisms of chain refolding in the course of thermal annealing are described. The object of this study, i.e. semicrystalline-amorphous block copolymers PS-b-PEO are introduced, and their crystallization behavior is specified. Finally, the aims and scope of the thesis are summarized.

I.1 Macromolecules and crystallization

Polymer is a chain-like molecule consisting of repeating subunits, the so-called monomers[1]. The basic parameter used to describe the polymer chain, after having specified its chemical constituents, is the number of repeat units, N, termed the "degree of polymerization" (DP). The DP can reach several millions for ultra-high molecular weight polymers. Fabrication of such long chains without error in a sequence of successive operations is a remarkable chemical challenge leading to the definition of the second important physical characteristics of a polymer sample, the polydispersity[2-4].

First evidences for polymer crystallization appeared in the 1920's when the newly introduced technique of X-ray diffraction was applied to synthetic and natural polymers. In contrast to low molar mass compounds and inorganic matter, the Bragg reflections were relatively broad. In view of the fact that synthetic polymers in the melt consist of long chains with important variation of the chain length, with a high degree of chain interpenetration and entanglement, it was not easy to understand how crystallization can ever occur in such system upon cooling.

Crystallization considerably alters the physical and mechanical properties of polymer systems. It is noteworthy that crystallization is not limited to linear polymer chains such as polyethylene (PE) and polyethylene oxide (PEO), but also occurs for more complicated polymer architectures such as brushes.

I.1.1 *First model of the semicrystalline polymer: the fringed micelle*

In the 1930's, when the scientific community started to accept the idea of long chain molecules, *Abitz, Gerngross and Herman* [5] introduced the so-called fringed micelle model for polymers in the solid state (e.g., Fig. I.1). In this model, the chain molecules pass through many crystallites, and the crystals act as physical cross-links. This model could explain at that time many phenomena such as swelling and the lower density of polymers in the solid state compared with the unit-cell density, and, last but not least, the broad Bragg reflections when shined by X-rays.

I.1.2 *Crystal building block: the crystalline lamella*

Single crystals have been identified in the course of crystallization from dilute solution[6], at first in polyethylene by

Till, Keller and Fischer simultaneously in 1957[7-9] and subsequently in a large number of other polymers[10]. All polymer single crystals grown from dilute solution have the same general appearance; they consist of thin platelets or lamellae about 10 nm thick. The size, shape and regularity of the crystals depend on their growth conditions. Such factors as solvent, temperature, concentration, and rate of growth are important. The precipitate, obtained by lowering the temperature of the solution, is in a finely dispersed form. When deposited and examined by the electron microscope, it revealed small platelets shown in figure I.2. The electron diffraction experiments on such crystals give patterns characteristic of single crystals, and indicate that the molecules are close to the normal to the lamellae.

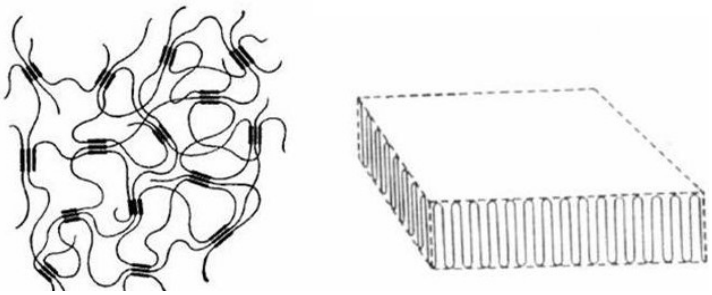

Fig. I.1 Schematic representation of the fringed micelle concept (left) and folded-chain lamellar crystal (right).

Crystallization into relatively well-defined single crystals is limited to supercooled dilute solutions. In the case of

crystallization from concentrated solutions or from polymer melts, various morphologies can be obtained, ranging from axialites, dendrites to spherulites. In contrast to crystallization from dilute polymer solutions, where the chain hardly overlap, the crystallization mechanism in supercooled melt is not very well understood. Even in the case of dilute solutions, the mechanism of polymer crystallization on the molecular scale is not settled yet and is, in fact, one of the issues considered in this thesis.

I.1.3 *Evidence of chain folding*

The evidence of folding was shown in the pioneering works of *Keller*[9]. Technical development of electron microscopy and the possibility to examine samples in direct and reciprocal space allowed this great discovery in polymer science. Based on electron-diffraction patterns, *Keller*[9] concluded in 1957 that the direction of the polymer chains run perpendicular to the basal plane of the crystals and since the length of the polymer molecules exceed by many times the crystal thickness, the polymer chains must be folded many times. The phenomenon of folded-chain crystallization in polymer molecules triggered a large interest in the polymer community.

Observations of single crystals immediately raised the problem of how the long chains are accommodated within the crystal entity. Comparison of the left and right panels of figure I.2 leads to only one reasonable solution. The layers in figure I.2 are close to 10 nm thick, as far as it is possible to conclude from the electron micrographs. The diffraction pattern reveals that the **c** (molecular) axis is perpendicular to the platelet, i.e. that one is seeing the crystal along the projection as in figure I.2. The thickness of the individual layer can be measured from the electron micrographs and is always found to be in the range of 10 nm. However, it is clear that these materials consist of long chains with lengths which exceed many times the layer thickness, and also the chains are of non-uniform length. Therefore the chains cannot be accommodated by the layers in the orientation identified by the diffraction pattern, unless they are folded back on themselves many times, the straight stems of the folded molecule forming the crystal lattice. In the literature, one can find an even earlier proposition of chain folding based on a less well-defined and less stable system of a polycrystalline film of gutta-percha, which attracted less attention at the time "*the macromolecules are folded back and forth upon themselves in such a way that adjacent sections remain parallel*"[11].

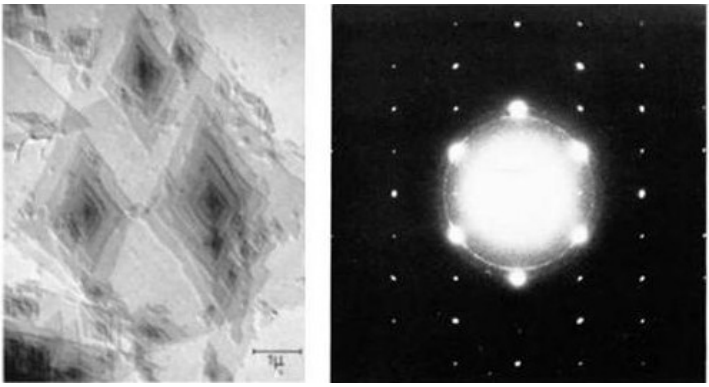

Fig. I.2 Typical solution-grown crystal of polyethylene. Electron micrograph and the corresponding electron diffraction pattern in the same orientation.

I.1.3.1 **Random reentry or "switchboard" model**.

In contrast to the regularly folded lamellar crystal (cf. Fig. I.1), the "switchboard" model proposed by *Flory*[12] describes a crystal with chains randomly folding back onto the same lamella, or even participating in adjoining lamellae. The lamellar surfaces consist of loops of varying sizes and the amount of adjacent reentry is small and not a necessity.

I.1.4 ***Lateral habit of the crystalline lamella***

The lateral habit of solution-grown single crystals has been the subject of many experimental and theoretical studies. In the case of PE, lozenge, truncated lozenge, lenticular and rounded shapes were identified in different crystallization conditions.

For small molecular weight PEO (3-10 Kg/mol) single crystals grown from the melt, *Kovacs* and coworkers[13-15], described a variety of shapes, called pathological shapes. These lamellae crystallized in once folded or extended chain conformation, can have square, hexagonal or rounded habits. For the lateral habit dependency of PS-*b*-PEO, *Lotz*[16] reports that the crystal shape depends on the crystallization temperature and the ratio of the amorphous PS to crystalline PEO block. The formation of the anisotropic single crystal morphology implies that the growth rate along one specific crystallographic direction is faster than along the others. Therefore, the nucleation barrier for crystallization at growth fronts corresponding to specific crystallographic directions is different.

I.1.5 *Lamellar thickness*

The thickness of the crystals is governed by the crystallization conditions and it is determined mainly by the degree of undercooling ΔT as $l_c = \frac{K_l}{\Delta T}$, where K_l is a material constant[17]. In fact K_l is related to the melting enthalpy and the surface free energy in a given crystallization conditions and it can be written as $K_l = \frac{2\sigma_e T_d}{\Delta h_d}$.

I.1.6 *Crystalline structure of PEO*

The crystalline structure of PEO is a 7_2 helix with symmetry isomorphous to the point group *D7*[18]. Here, the 7_2 helix means that seven monomeric units turn two times along the c axis within one unit cell. Four 7_2 helical chains constitute the unit cell with parameters, a = 8.05 Å, b = 13.04 Å and c (chain axis) = 19.48 Å, with β = 125.4° and corresponding to the space group $P2_1/a$-C2h.

A triclinic crystalline modification with a=0.471, b=0.444, c=0.712 nm, α=62.8, β=93.2 and γ=111.4° was found in a PEO sample stretched about two-fold after necking at room temperature[19]. As indicated by the authors, the planar zigzag chains pass through the unit cell. After the tension is removed, the chain conformation turns back to the 7_2 helix conformation quickly.[20]

PEO can adopt different crystal modifications in the complex forms when it is blended with small molecules such as urea, thio-urea[21,22], $HgCl_2$ [23] or resorcinol[24].

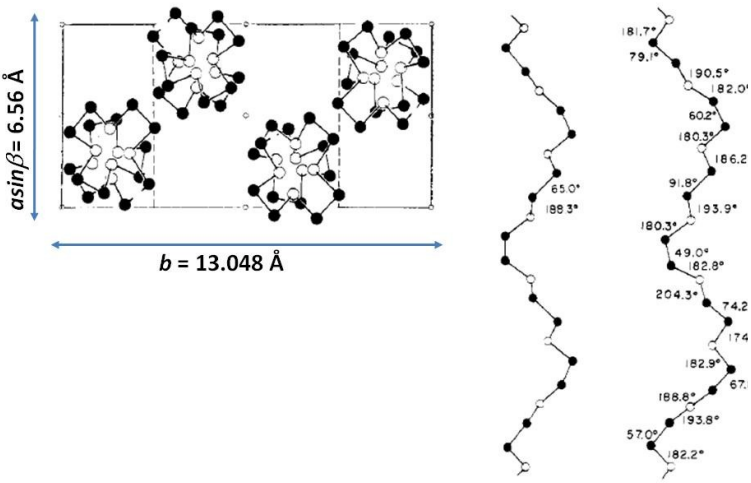

Figure I.3 Crystal structure of PEO (left) and molecular model of a real PEO helix (right) from Takahashi[25].

I.1.7 *Chain and fold packing direction within single crystals of PS-b-PEO*

The crystalline structure and chain orientation within one individual single crystal of PS-*b*-PEO was obtained with the help of the selected-area ED. A typical diffraction pattern for a single crystal is shown in figure I.4. Four main 120 spots related to the most densely packed plane are visible, with supplementary weaker 010 spots. The electron diffraction pattern showed in Figure I.4 indicates that the *a** and *b* axes of the unit-cell are parallel to the diagonal of the crystal. This indicates that the electron beam travels parallel to the chain

axis, i.e. the chain axis is normal to the basal plane of the single crystal. However, the thickness of the crystals is ≈10 nm, whereas the length of the PEO chains is usually much larger, which obviously means that the PEO chains must be folded. Therefore the single crystals displayed in figure I.4 actually have a sandwich structure, in which the crystalline core is delimited by more disordered areas of folded PEO segments and of amorphous PS.

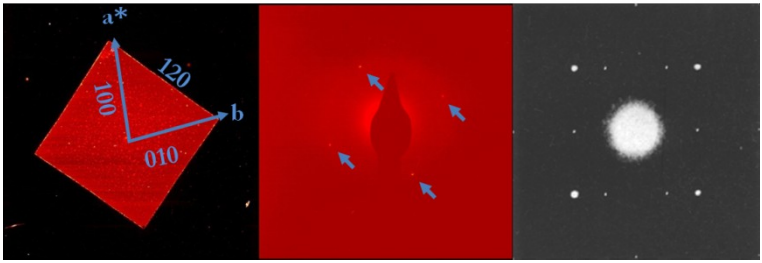

Figure I.4: Square-shaped single crystal of PS-b-PEO (40-680) crystallized at 30°C.The growth facets are bounded by four {120} plans, the sectors are limited by the (100) and (010) axes (left). Typical electron diffraction pattern showing four {120} spots (middle) and the one reproduced from *Lotz*[26] (right).

The diffraction patterns shown in figure I.4 (middle) are highly beam sensitive, which leads to the degradation of the crystal within typically 30 seconds. The weak reflections are

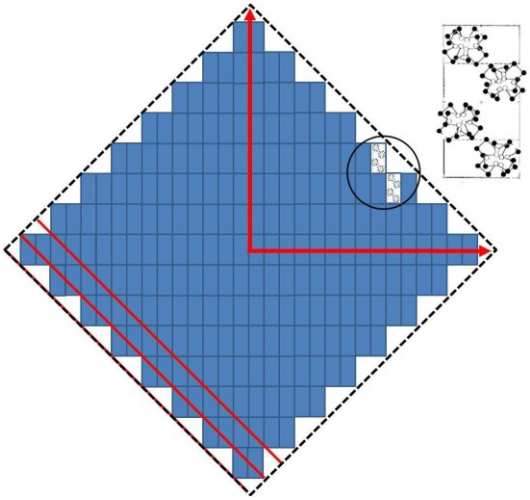

Figure I.5: Model of chain packing of PEO; $a^*=a\sin\beta=0.656$nm, $b=1.304$ nm. The folds are supposed to be parallel to the {120} plane.

even more beam sensitive than the strongest ones and we were unable to reproduce them in our laboratory.

The major fold orientation of high molecular weight PEO single crystals grown from dilute solution is along the {120} planes[27,28]. This was first proposed by *Lotz*, et al.[29] and *Balta Calleja*, et al.[30], and was demonstrated later by the PE decoration method by *Lotz* and *Wittmann*[27] and later by direct AFM observations[31].

I.1.8 *Chain-folding in PS-b-PEO single crystals*

PEO has been extensively used to address the integral and nonintegral folding (NIF) structure. *Kovacs* et al.[32-34] pioneered this issue by pointing out the relationship between linear growth rate, single crystal morphology, and the integral folding (IF) structure. By using time-resolved small-angle X-ray scattering (SAXS), *Cheng* and coworkers[35-43] demonstrated the existence of NIF structure. Systematic studies indicated that the NIF crystals form first in the early stage of crystallization as an intermediate stage with respect to the IF crystals. The formation of NIF's is due to the lower nucleation barrier[44], i.e., most favorable kinetics. However, the NIF crystals are thermodynamically less stable than the IF crystals, which leads to the subsequent transformation from NIF crystals to the more stable IF crystals by a lamellar thickening or thinning process.

Further studies on the effect of chain end group and molecular weight indicate that the NIF to IF transition is increasingly hampered upon increasing the size of end group or molecular weight[35].

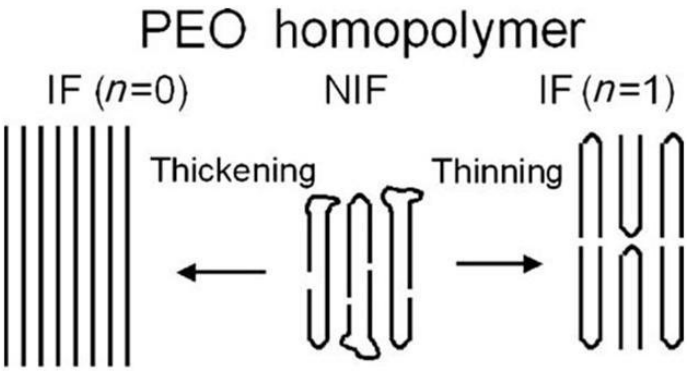

Figure I.6: Schematic representation of possible folded structures in the PEO homopolymer.

As far as the molecular architecture is concerned, it is interesting to address the described IF or NIF forms for the PEO block copolymers, as it was done by *Stühn* et al.[45] The covalent connection with an amorphous segment, e.g., polystyrene PS, significantly changes the possibility of the chain reconfiguration in the crystalline state. Intuitively, the formation of NIF crystals as an intermediate stage seems in this case very unfavorable, as the PS should always be rejected from the crystalline core. This is indeed what is found in the study.

When the NIF crystals transform into the IF crystals, the LMW PEO chains take sliding diffusion motion along the crystallographic c-axis, resulting in the apparent thickening or

thinning of lamellar crystals. This molecular diffusion motion is cooperative, which may involve two or more chain stems, folds, and chain ends moving simultaneously. Therefore, the NIF/IF crystal transformation exhibits a strong dependence on the molecular architecture[35]. In particular, upon increasing the end group size of the LMW PEOs, thickening and thinning processes are increasingly hampered[46]. For the LMW PEOs with large end groups, e.g. –OC(CH3)3 and –OC6H5, the life time of the NIF crystals can be very long.

In the bulk, the diblock copolymers may form microphase separation structures. In the strong or medium segregation limit regime, away from the order–disorder transition (ODT), the crystallization of PEO blocks will take place within the ordered phase structures. The original ordered phase may be either destroyed if the PEO crystallization temperature (T_c) is higher than the glass transition temperature of amorphous blocks T_g^a or remained intact, especially when $T_c<T_g^a$. The formation of PEO extended-chain crystals is largely impeded, mainly because the amorphous blocks accommodated on lamellar surfaces will be stretched when the tethering density is increased. Thermodynamically, the final crystal morphology of PEO diblock copolymers reflects the balance between an enthalpic driving force to minimize the fold surface energy

and the entropic term resulting from stretching of amorphous blocks[47].

Kovacs et al.[16] shows that for short PEO chains the fold length ranges from 1.5 to 3.5 nm, which includes between 5 and 12 unit monomers. The melting temperature T_m and enthalpy of fusion have been measured, by DSC, for folded chain crystals of low molecular weight PEO fractions ranging from 3000 to 10000. These crystals are formed by molecules folded a small integer number of times, *n*, and show unusual thermal stability on heating. Extending the theoretical treatment of *Flory* and *Vrij* to folded chain crystals, a reasonable estimate was derived for the respective surface free energy contributions of chain ends and chain folds. The results suggest considerable hydrogen bonding for the case of OH termination, with a bonding energy of 3.1 Kcal/mole, when the crystal surface contains only the chain ends. Hydrogen bonding is essentially destroyed by chain folding. Further analysis leads to an estimate of the contour length of cilia, associated with chain ends and to that of chain folds, on the average, to 2.8 and 3.5 monomer units, respectively. The chain folds must thus be sharp, involving mainly adjacent re-entry. Finally, an analytical expression is derived showing the separate dependence of T_m on the chain length and *n*, which

determine the crystal thickness. Critical comparison of this relationship to that commonly used for determining surface free energies from linear T_m vs $1/Lc$ plots shows that the latter only applies accurately to chains of infinite length.

From these results a picture of the surface of PEO crystals emerges. The chain ends protrude the crystal on average by 2.8 monomer units. The chain folds occur as short loops with adjacent re-entry, since they each contain only 3.5 monomer units on average. It should be pointed out that these estimated lengths for cilia and chain folds are only approximate. Nevertheless, for crystals of about 15 nm thick, these estimates lead to an amorphous content of the order of 10 per cent which is consistent with the average crystallinity of the samples investigated, as derived above from unpublished dilatometric measurements.[48]

I.2 Theories of polymer crystallization

After the discovery of the folded chain polymer crystals, a number of suggestions were made to explain the regularity of folding. Two major theories have been developed and applied to experimental results. One, developed by *Peterlin, Fischer and Reinhold*[49], suggests that the fold period is determined thermodynamically, corresponding to a minimum in the free

energy density of the crystal at the crystallization temperature. The other theory suggested independently by *Lauritzen and Hoffman*[50,51] and is based on a kinetic approach.

Kinetic theories assume that the observed lamellar thickness corresponds to the crystal which grows fastest, and is not necessarily the most stable crystal. One of the intriguing questions remaining in this field is: why do polymer chains fold upon crystallization instead of forming exclusively extended chain crystals? The trivial answer on this question could be that the kinetic energy barrier towards folded-chain crystals is lower and, therefore, this process occurs at a faster rate as compared with the formation of extended chain (EC) crystals. In the other words, crystallization is largely controlled by kinetics. As a consequence, the Gibbs free energy of folded-chain crystals is higher than that of the equilibrium extended-chain crystals, and they will melt accordingly at a lower temperature.

I.2.1 *Thermodynamic considerations: Gibbs-Thomson equation for polymer crystal melting*

From the thermodynamic viewpoint, the free energy G of polymer crystal below its melting point T_m has a lower free

energy than the liquid state. Figure I.7 schematically shows variation of the Gibbs free energy of a liquid and crystal with temperature. The necessary (but not sufficient) criterion for any spontaneous phase transformation for a process at constant temperature and pressure is a negative value of ΔG. In the case of polymer crystals, one has to differentiate between the equilibrium melting temperature T_m^0 and the actual melting temperature,T_m, which is dependent on the fold length, or crystal thickness.

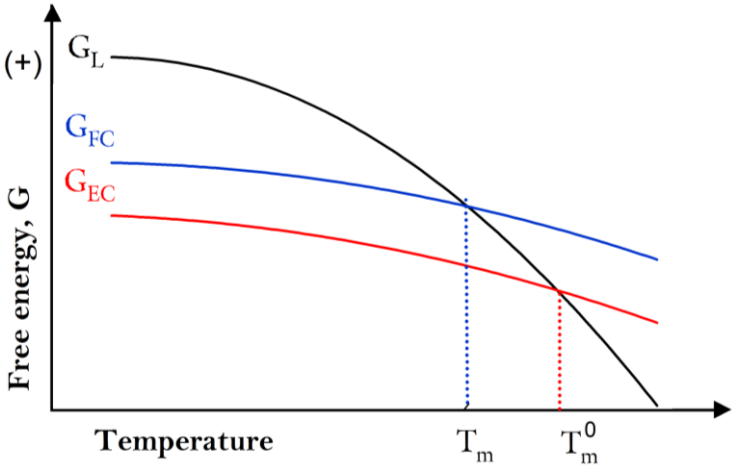

Fig. I.7 temperature variation of the Gibbs free energy G for the liquid state, folded-chain (FC) and extended-chain (EC) polymer crystal.

The thermodynamic driving force for crystallization from a liquid state to a folded-chain crystal at a given crystallization temperature T_c, can be written as:

$$\Delta G = \Delta H - T\Delta S \qquad \text{I.1}$$

At the equilibrium melting temperature, T_m^0 , ΔG = 0 and

$$T_m^0 = \frac{\Delta H}{\Delta S} \qquad \text{I.2}$$

Substituting Eq. I.2 into I.1 gives:

$$\Delta G = \frac{\Delta H(T_m^0 - T)}{T_m^0} \qquad \text{I.3}$$

At a particular crystallization temperature T_c, the driving force for crystallization can be approximated as:

$$\Delta G = \frac{\Delta H(\Delta T)}{T_m^0} \qquad \text{I.4}$$

where ΔT is the so-called supercooling, $\Delta T = (T_m^0 - T_c)$. Thus a higher value of ΔH leads to a higher T_m^0; the entropic effects cannot be ignored as well, and are often dominant in determining the value of T_m^0.

I.2.2 *Gibbs-Thomson equation*

Folded-chain crystals are metastable and melt well below the equilibrium melting temperature T_m^0 (cf. Fig. I.7). The main reason for that is the relatively small dimension of the crystals

in the chain direction. Consequently, the surface free energy plays an important role (the surface-to-volume ratio is extremely high for example for a crystal which is 10 nm thick and has a 10 μm lateral side. Due to the surface free energy, the G-value for folded-chain crystals is higher compared with the perfect extended-chain crystals (cf. Fig. I.7).

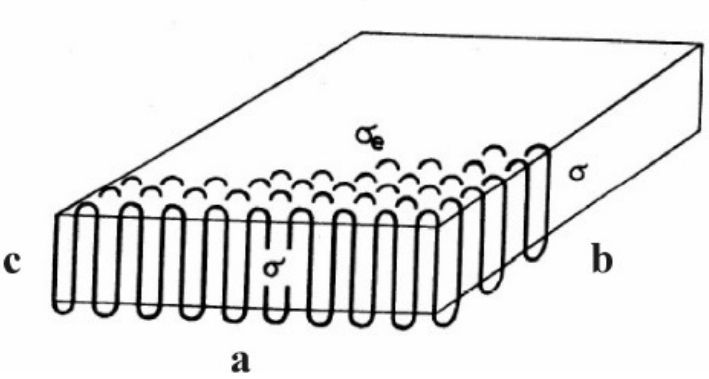

Fig. I.8: Schematic representation of a single polymer crystal.

For a finite-size crystal as shown in figure I.8, the free energy is given by:

$$\Delta G_{crystal}\,(T) = 2xy\gamma_e + 2l(x+y)\gamma - xyl\Delta G_f^{\infty}\,(T) \qquad \text{I.5}$$

At the melting point of the crystal,

$$\left(\Delta G_{crystal}\right)_{T_m} = 0 \qquad \text{I.6}$$

Assuming that

1. there is no thickening possible;
2. $ab \gg l(a+b)$ for thin lamellae with large lateral dimensions;
3. $\sigma_e \gg \sigma$, which holds for most polymers;
4. $a \sim b$ for large lateral dimensions,

Eq. (I.5) becomes:

$$\Delta G_f^{\infty}(T_m) = 2\sigma_e / l \qquad \text{I.7}$$

For an infinite-size crystal at T_m^0, one can write:

$$\Delta G_f^{\infty}(T_m^0) = \Delta H_f^{\infty}(T_m^0) - T_m^0 \Delta S_f^{\infty}(T_m^0) \qquad \text{I.8}$$

and therefore

$$\Delta S_f^{\infty}(T_m^0) = \Delta H_f^{\infty}(T_m^0)/T_m^0 \qquad \text{I.9}$$

For the same infinite crystal at T_m: the free energy is given by:

$$\Delta G_f^{\infty}(T_m) = \Delta H_f^{\infty}(T_m) - T_m \Delta S_f^{\infty}(T_m) \qquad \text{I.10}$$

Assuming that

$\Delta H_f^{\infty}(T_m) = \Delta H_f^{\infty}(T_m^0)$, i.e. the slow temperature dependence is ignored, and

$\Delta S_f^{\infty}(T_m) = \Delta S_f^{\infty}(T_m^0)$ for high T_m's,

it can be easily obtained that:

$$\Delta G_f^{\infty}(T_m) = \Delta H_f^{\infty}(T_m^0) - T_m \Delta S_f^{\infty}(T_m^0) \qquad \text{I.11}$$

$$\Delta G_f^{\infty}(T_m) = \Delta H_f^{\infty}(T_m^0)[1 - \frac{T_m}{T_m^0}] \qquad \text{I.12}$$

Comparing eq. Eq. (I.7) and eq. (I.12), one gets:

$$2\sigma_e / l = \Delta H_f^{\infty}(T_m^0)[1 - \frac{T_m}{T_m^0}] \qquad \text{I.13}$$

This can be written in the conventional form of the Gibbs-Thomson equation:

$$T_m = T_m^0 \left[1 - \frac{2\sigma_e}{l \Delta H_f^{\infty} T_m^0}\right] \qquad \text{I.14}$$

The equation provides one of the convenient ways for estimating the value of the equilibrium melting point T_m^0, and obtaining the surface energy σ_e. These quantities are determined by plotting the observed melting points T_m vs $\frac{1}{l_c}$ where the value of σ_e can be computed from the slope, and

the intercept gives the value of T_m^0. The lamellar thickness l_c can be typically obtained by SAXS or sometimes TEM, whereas T_m is usually obtained by DSC. Previously, quite a number of authors attracted the attention to the complications of this method, for example due to thickening of the crystals.

Apart from the melting point depression described by the Gibbs-Thomson equation, one has to bear in mind that the crystal thickness should also correlate with the crystallization temperature. Early on, it was observed that the crystallization temperature determined the fold length of a crystal in such a way that the fold length increased for higher crystallization temperatures[52,53]. For a given polymer-solvent system it was also proved that the fold length increases with crystallization temperature.[10] However, the effect of the solvent on the fold length proved to be more point to establish for various experimental reasons.[54] Generally, when a given sample is crystallized in two different solvent powers, the thickness of the platelets was found to be

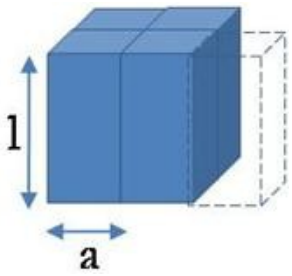

Fig. I.9: Schematic representtation of a nucleus with thickness l, width a, formed by ν chains.

mainly sensitive to the degree of supercooling, which directly depends on the solvent quality. This was figured out for example for polyethylene crystallization in xylene and octane, where the crystal thicknesses corresponding to the poorer solvent, octane, were displaced towards higher temperatures by the difference in dissolution temperatures. Similar behavior was observed also for PEO.[55]

All the facts mentioned above are a simple consequence of the Gibbs-Thomson equation: the crystals forming at a particular crystallization temperature have to be stable. Therefore the crystal thickness should generally increase with crystallization temperature. The kinetic aspects of the polymer crystal growth will be considered in detail further in Section I.2.5.

I.2.3 *Primary nucleation*

The nucleation theory assumes that the thickness of the primary nucleus equal the thickness of the lamellae. This is however not always true, because the lamella thickness can change for example in response to a change in the crystallization temperature.

Let us consider a nucleus of thickness l containing ν chains each at a distance *a* from each other, organized in a square

array. The excess free enthalpy (Gibb's function) due to the creation of the nucleus is given by:

$$\Delta G = 4la\sqrt{\nu}\,\sigma + 2\nu a^2\sigma_e - \nu a^2 l\Delta f \qquad \text{I.15}$$

where σ, σ_e are the side surface and fold surface free enthalpy per unit area, and $\Delta f \cong \Delta h \Delta T/T_m^0$ is the free enthalpy per unit volume of crystal, Δh is the heat of fusion per unit volume at the equilibrium melting temperature T_m^0, and ΔT the supercooling. Then a critical nucleus size is defined at the maximum of the free enthalpy ΔG as:

$$l^* = \frac{4\sigma_e}{\Delta f} \qquad \text{I.16}$$

and

$$\Delta G^* = \frac{32\sigma^2\sigma_e}{(\Delta f)^2} \qquad \text{I.17}$$

and the rate of formation of a primary nucleus is given by:

$$S \cong \frac{N_A kT}{h} e^{-\frac{\Delta \emptyset}{KT}} e^{-\frac{\Delta G^*}{KT}} \qquad \text{I.18}$$

where N_A is the Avogadro number, kT/h is the frequency of thermally activated vibrations (k being the Boltzmann's

constant and h – the Plank constant) and $\Delta\emptyset$ is the activation energy of transport for a molecule to cross the phase boundary to reach the crystal surface.

I.2.4 *Secondary nucleation*

It is widely accepted that the secondary nucleation is more relevant for the determination of the lamellar thickness than the primary nucleation. In this case, the nucleation will take place at the surface of the already crystalline nucleus. Assuming that the thickness of the substrate is not less than that of the nucleus and that the nucleus is in contact with the substrate, the excess free enthalpy of formation can be written as

$$\Delta G = 2la\sqrt{\nu}\,\sigma + 2\nu a^2\sigma_e - \nu a^2 l\Delta f \qquad \text{I.19}$$

Similarly to equation (1.2) the critical secondary nucleus size is $l^* = \frac{2\sigma_e}{\Delta f}$, which is just the half size of the primary nucleus and

$$\Delta G^* = \frac{4a\sigma\sigma_e}{\Delta f} \cong \frac{4a\sigma\sigma_e T_m^0}{\Delta h \Delta T} \qquad \text{I.20}$$

The free energy for the secondary nucleus thus scales as $(\Delta T)^{-1}$, which is in contrast to the $(\Delta T)^{-2}$dependence predicted for the primary nucleation.

I.2.5 ***Lauritzen-Hoffman theory***

Two main kinetic theories have been proposed for the polymer crystallization including the Lauritzen-Hoffman secondary nucleation (LH) theory[50,51] and Sadler's rough surface or entropic theory[56]. Both models share the assumption of a free energy barrier. The nature of the barrier distinguishes the LH theory from rough surface theory in considering the development of polymer crystals it is necessary to consider both nucleation and crystal growth.

The experimental results that the growth rate is proportional to $\exp(-1/\Delta T)$ and the formation of facetted single crystals in solution strongly suggest that polymer crystallization is nucleation controlled. On this basis, a surface nucleation theory was proposed by *Lauritzen and Hoffman*[50,51]. The LH model quantitatively describes how fast the growth front advances under given crystallization conditions. In this model, the lamellar crystal growth front, which is actually the lateral surface of a lamellar crystal, is thought to be smooth. In the initial stage, as shown in figure I.10, a molecular stem attaches to the smooth crystal substrate, leading to an activated state. This process, which is called surface nucleation or secondary nucleation, generates two new lateral surfaces, leading to an increase of the overall free energy ($\Delta\emptyset_1 =$

$2b_0\sigma l$) as shown in figure I.10. Here, b_0 stands for the thickness of the layer.

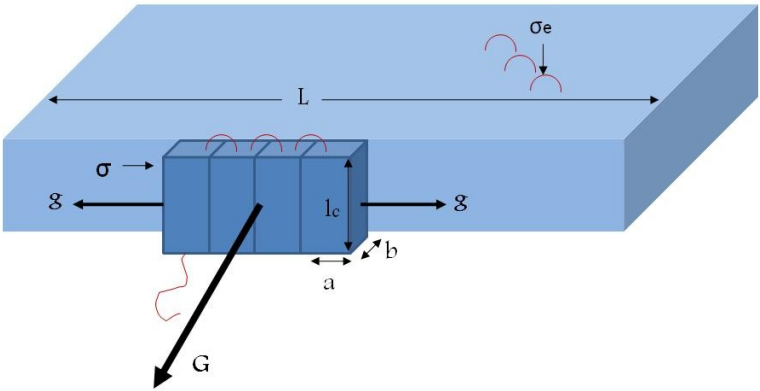

Fig. I.10: Model of surface nucleation and growth of chain folded crystal. The surface nucleus composed of ν stems of length lc, thickness b and width a, forms on a substrate and spreads along the lateral direction with a growth rate *g*. The surface nucleus then completes a layer of thickness b by spreading to crystal width L, causing the crystal to grow in the G direction. Lateral (σ) and fold (σ_e) free energies are indicated.

In the LH theory, this first step is associated with the largest energy barrier and is therefore considered as the rate-determining step. The magnitude of this barrier increases with the lamellar thickness (l). In the second step, the segments become crystallographically registered and a certain free energy ($\Delta\emptyset_2 = -a_0 b_0/\Delta G_f$) is released, where a_0 is the width of the stem. In the following steps, subsequent stems fold back and are deposited adjacent to the attached stems to further lower the

overall free energy until reaching a negative global free energy change. The free energy change associated with this sequential folding process is $\Delta\emptyset_2 = (n-1)a_0b_0(2\sigma_e - l\Delta G_f)$

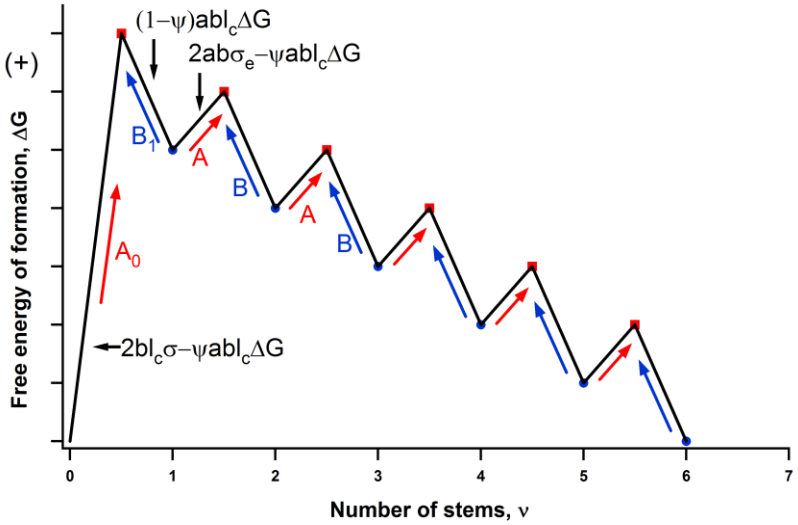

Fig. I.11: Free energy corresponding to the formation of a chain-folded surface nucleus. The diagram shows the relationship of the rate constant A0, B1, A and B to the free energy of the processes involved in the formation and the growth of the surface nucleus as it spreads in the g direction.

With these free energy barriers, the rate constant for each step can be obtained using an Arrhenius expression:

$$A_0 = \beta\, exp\left(-\frac{2b_0\sigma l}{KT}\right) \qquad \text{I.21}$$

$$B_1 = B = \beta \exp\left(-\frac{a_0 b_0 l(\Delta G)}{KT}\right)$$

$$A = \beta \exp\left(-\frac{2a_0 b_0 \sigma_e}{KT}\right)$$

where A_0 is the rate constant for attainment of the activated state, B and B_1 are those for removing an attached stem back to the melt state (here B_1 is for removing the first stem), A is that for the forward reaction for the deposition of each stem when $v \geq 2$, β is a factor that accounts for retardation due to transport of chain segments to or from the growth front and, ΔG is the free energy of fusion at the crystallization temperature.

With these rate equations, the flux of stems of length l over the nucleation barrier can be determined in the general case as:

$$S(l) = N_0 A_0[(A - B)/(A - B + B_1)] \qquad \text{I.22}$$
$$= N_0 A_0(1 - B/A)$$

where N_0 is the number of reacting species which can be defined as, $N_0 = C_0 n_L$, where C_0 is the configurational path degeneracy and n_L is the number of stems with width a_0

comprising the substrate length L. The net flux across the nucleation barrier therefore can be calculated:

$$S_T = \frac{1}{l_u}\int_{2\sigma_e/\Delta G}^{\infty} S(l)dl \qquad \text{I.23}$$

where l_u is the monomer length. Using the definition of surface nucleation rate i:

$$i \equiv \frac{S_T}{L} = \frac{S_T}{n_L a_0} \qquad \text{I.24}$$

one obtains:

$$i = \frac{c_0\beta}{a_0 l_u}\left(\frac{KT}{2b_0\sigma} - \frac{KT}{2b_0\sigma + a_0 b_0 \Delta G}\right)\exp\left(\frac{-4b_0\sigma\sigma_e}{\Delta G KT}\right) \qquad \text{I.25}$$

In the case of PE, for example, $a_0 b_0 \Delta G$ is much less than $2b_0\sigma$. Therefore Eq I.25 can be simplified to become:

$$i = \frac{c_0\beta}{a_0 l_u}\left(\frac{KT}{4b_0 l_u \sigma^2}\right)\exp\left(\frac{-4b_0\sigma\sigma_e}{\Delta G KT}\right) \qquad \text{I.26}$$

Similarly, the initial lamellar thickness (l) can be obtained by performing a statistical mechanical average with the flux being the weight factor:

$$\langle l \rangle = l_g^* = \frac{\frac{1}{l_u}\int_{2\sigma_e/\Delta G}^{\infty} lS(l)dl}{\frac{1}{l_u}\int_{2\sigma_e/\Delta G}^{\infty} S(l)dl} \qquad \text{I.27}$$

This yields

$$l_g^* = c + \frac{KT}{2b_0\sigma}\left(\frac{\Delta G + 4\sigma/a_0}{\Delta G + 2\sigma/a_0}\right) \qquad \text{I.28}$$

$$= \frac{2\sigma_e}{\Delta G} + \delta$$

$$= \frac{2\sigma_e T_m}{\Delta h_f \Delta T} + \delta$$

where : $\delta = \frac{KT}{2b_0\sigma}\left(\frac{\Delta G+4\sigma/a_0}{\Delta G+2\sigma/a_0}\right)$. Under low and moderate undercooling, δ can be approximated as:

$$\delta = \frac{KT}{b_0\sigma} \qquad \text{I.29}$$

Hence the LH theory predicts (eq. I.28) that the initial lamellar thickness is a linear function of $1/\Delta T$, which has been observed experimentally.

The substrate completion rate, g, is defined to be:

$$g \equiv a_0(A - B) \qquad \text{I.30}$$

Using Eq. 1.21, g becomes:

$$g \equiv a_0\beta exp\left(\frac{-2a_0b_0\sigma_e}{KT}\right)\left(1 - \exp\left(\frac{-a_0b_0\delta\Delta G}{KT}\right)\right) \qquad \text{I.31}$$

At low-to-moderate undercooling, the second exponential term in Eq. I.31 can be expanded and using Eq. I.29 and $\Delta G = \Delta h_f \Delta T/T_m$, g can be approximated to be:

$$g \equiv a_0\beta exp\left(\frac{a_0\Delta h_f\Delta T}{\sigma T_m}\right)\exp\left(-\frac{2a_0b_0\sigma_e}{KT}\right) \qquad \text{I.32}$$

It should be noted that, as a coarse model, LH theory treats the attachment of the stems onto the substrate as a one-step process and ignores the entropic character of the nucleation event and subsequent spreading of the stems in the early version of this theory. Later, the segmental nature and entropic origin of the initial surface nucleation process have been considered by *Hoffman*[51]. He correlated the lateral surface free energy σ to the characteristic ratio C_∞ and attributed the free energy barrier of the surface nucleation to an entropic

origin. In the LH model, since there is no new lateral surface generated during completion of the rows, the only free energy barrier during this process is associated with folding (i.e., creation of the fold surface of free energy of σ_e). In addition, this free energy contribution from σ_e is not related to the lamellar thickness, therefore according to Eq. I.32, the substrate completion process weakly depends on the undercooling, as compared to the surface nucleation process which has an exponential dependence on undercooling.

The precious fact about the LH theory is that it explains the kinetics of crystallization in molecular terms, for linear flexible macromolecules which are crystallized from the melt into chain folded lamellae. This theory constitutes perhaps the most widely used methodology to interpret and model the crystallization behavior of a large number of polymers. The theory has evolved substantially since it was first put forward and has been modified to broaden the scope of its predictions.

I.2.6 *Growth regimes*

Independently of the details of the LH theory, the existence of three growth regimes can be defined according to the competition between i and g, as shown in Figure I.12.

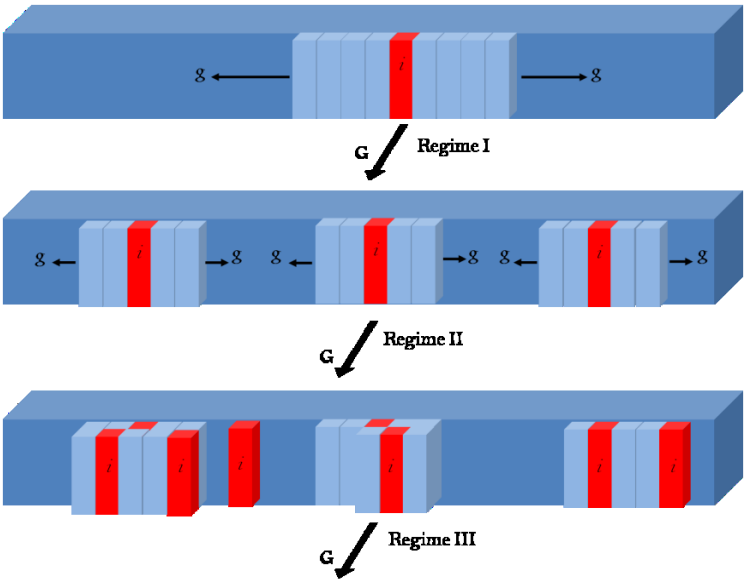

Fig. I.12: Schematics of the secondary nucleation corresponding to the three growth regimes.

At high temperature, the surface nucleation is very slow which controls the overall growth rate G. This temperature range is defined as the mononucleation regime, or regime I, in which G can be expressed as:

$$G_I = b_0 i L \qquad \text{I.33}$$

In the intermediate temperature range, which is defined as regime II, the growth rate is controlled by both i and g and can be expressed as:

$$G_{II} = b_0(2ig)^{1/2} \qquad \text{I.34}$$

When the temperature is lowered further, the nucleation rate would become extremely high, and there is not much space for the nuclei to spread before they impinge on each other. In this case, the growth rate will be determined by the nucleation rate again as in regime I. This temperature range is defined as regime III. Similarly to regime I, the growth rate in regime III also can be given as:

$$G_{III} = b_0 iL' \qquad \text{I.35}$$

I.3 Annealing of polymer crystals

Annealing of polymer crystals can be accompanied by structural modifications taking place at very different spatial scales. This evolution can be particularly complex because, as was shown in Section I.2.2, the nanometer-thick crystalline lamellae form essentially metastable phases for which the melting point depends strongly on the lamellar thickness[57]. Therefore it is clear that annealing of semicrystalline materials above the lowest melting point of the constitutive crystals could dramatically change their microstructure. Some aspects of the micro-structure evolution on annealing will be considered in the following sections.

I.3.1 *Crystal thickness on annealing, recrystallization*

Heating an isothermally crystallized polymer is not always accompanied just by melting of the crystallites according to their stability. In many cases, the melting is immediately followed by formation of a new crystal. The recrystallization processes can have very different mechanisms, as compared to the initial melt-crystallization.

Another situation is encountered in annealing of single crystal suspensions. The frequent consequence of the heat treatment is the appearance of picture-frame-type crystals[58,59]. This is believed to be a result of dissolution and recrystallization. The polymer segments at the crystal edges dissolve and re-precipitate on the remaining crystal with a correspondingly higher fold length[59,60]. This gives rise to a thickened edge, which is now more stable against further increase of temperature, and can survive longer than the crystal interior. In the case of annealing of dry crystals, it was observed that the crystals once formed can subsequently thicken.[61] It was proposed that the crystals break up in a lace pattern while retaining the chain orientation normal to the substrate which indicates that the chains refold to a greater fold length. The associated SAXS patterns enabled the

thickening process to be followed quantitatively and established the irreversibility of the process.

I.3.2 *Time and temperature dependence of the long-spacing increase*

The increase of the fold length on annealing is undoubtedly one of the most remarkable properties of chain-folded polymer crystals. The process itself can be studied as a function of the two principal variables, annealing time and annealing temperature. The effect of temperature for two fixed annealing times was already demonstrated by *Keller (cf. references in 10)*. The first combined study of the two variables is due to *Fischer* and *Schmidt*[62] who examined the long-spacing increase of polyethylene single crystals as a function of time at different temperatures. It was found that the long spacing increases logarithmically with time as described by the equation:

$$LB = LB_0 + B(T)\log\left(\frac{t}{t_0} + 1\right) \qquad \text{I.36}$$

where LB_0, is the long spacing at time t_0 and *B(T)* is a constant corresponding to temperature *T*. This much-quoted relation has been well proven on many occasions to account for crystal thickening in the bulk. Nevertheless, it is not always

fully realized that its validity is confined within certain limits, for example the time scaling can change for thickening of isolated single crystals.

I.3.3 *Crystallization and melting lines*

The Gibbs–Thomson equation introduced previously can be also applied to examine in a semi-quantitative way the correlations between the inverse crystal thickness l_C^{-1}, and crystallization temperature T_C. The appearance of the crystallization lines is typical for a variety of polymers [63-66], i.e. in many instances the melting and crystallization lines cross each other (Fig. I.16). As mentioned before, the melting line allows the determination of the equilibrium melting point by linear extrapolation to infinite crystal thickness. If one formally follows the same reasoning for the crystallization line, one can introduce in a similar way the maximum crystallization temperature T_C^{∞}. The physical meaning of this temperature and that of the intersection point of the melting and crystallization lines are not yet understood.

It is however clear that the thermodynamically stable lamellar crystals can exist only at temperatures below the melting line. Therefore, the crystals cannot be formed any

longer when the temperature of intersection between the crystallization and melting lines is reached.

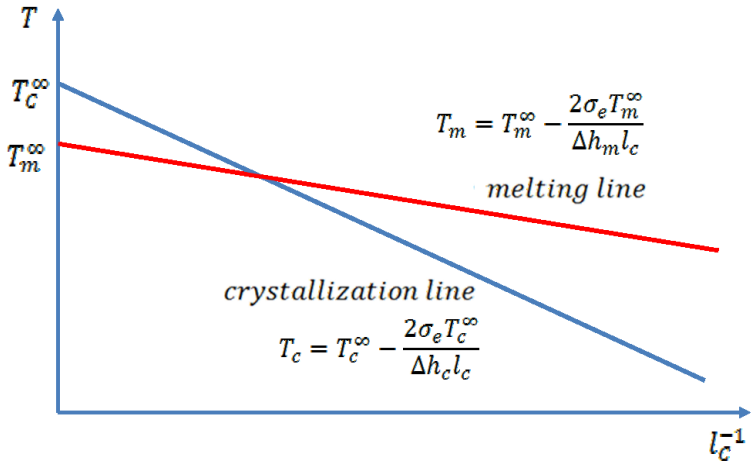

Fig. I.16: Schematic representation of the temperature versus the reciprocal crystal thickness l_c^{-1} showing the crystallization (blue) and melting line (red).

I.3.4 *Molecular mechanisms of the chain refolding*

Generally, the fold-length increase is a consequence of the system tending towards the lowest state of free energy, which is that of the fully-extended chain crystals. However the mechanisms of the chain refolding can strongly differ for various systems and annealing conditions. As mentioned previously, in the case of annealing of crystal suspensions the fold-length increase occurred via successive dissolution and

recrystallization of the chain segments at the crystal edges. For the dry state of the crystals the recrystallization mechanism was first proposed by *Kawai* [67]. He observed from diffraction patterns that during refolding the initial crystal orientation, including directions perpendicular to the chain axis, is preserved. This means that at no instant the memory of the original structure is lost during the refolding. Consequently there could have been no full melting in any portion of the crystal.

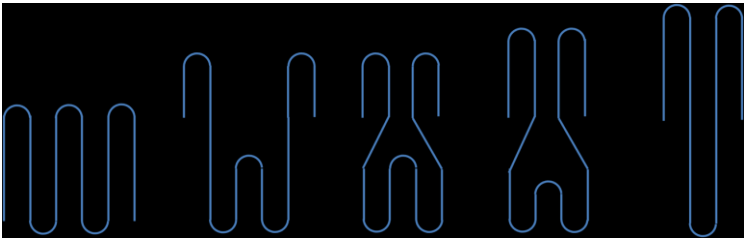

Fig. I.17: Schematic drawing of successive stages of the fold increase in single crystals on annealing.

From many experiments it was evidenced that the overall thickness of melt-crystallized lamellae increases with increasing the annealing temperature. This behavior can be associated with additional crystallization of amorphous portions at the lamellar surfaces, mass transport within the crystal (point defects), or partial intra-chain rearrangement (perfection) of the chain without coordinated displacement of a molecule as a

whole along its molecular chain. This can be described as 'fold dislocation' [68] and is accompanied by a quantum increase in lamellar thickness (cf. Fig. I.17). In the case of nylon single crystal mats[69,70], the doubling and quadrupling of lamellar thickness were observed above a certain threshold temperature.

I.4 Block copolymers

Block copolymers are macromolecules consisting of two or more chemically different polymer segments of a single type of monomer unit, covalently bonded together. The interest in the phase behavior of block copolymer melts stems from the microphase separation that leads to nanoscale ordered morphologies. This subject has been in the focus of a large number of studies due to its potential for various practical applications. Furthermore, in the case of block copolymers with the presence of crystallizable and non-crystallizable blocks, the structure formation leads for example to significant modification of mechanical properties as compared to the homologous crystalline homopolymer when a rubbery or glassy component is introduced. Thus, the influence of the amorphous block on the crystalline block can be very important.[71,72]

It is well documented that semicrystalline block copolymers can exhibit considerable morphological variety, which is due to the two forces driving the structure development: microphase separation between the unlike blocks, which favors the formation of nanometer length scale domains (e.g., spheres, cylinders, lamellae), and crystallization, which favors the formation of alternating amorphous and crystalline layers. For example, when the non-crystallizable block is glassy during crystallization, the phase separated melt structure is usually retained. It means that crystallization occurs within the nanoscale domains defined by microphase separation leading to a "structure-within-structure" morphology. However when the amorphous matrix is rubbery during crystallization, the overall structure can considerably differ from that established by the initial self-assembly in the melt. Combinations of chemically and physically different blocks provide a great number of potential structures for various applications.

The phase behavior of block copolymer melts is, to a first approximation, represented in a morphology diagram in terms of χN and f. Here f is the volume fraction of one block and χ is the Flory–Huggins interaction parameter, which is inversely proportional to temperature, and reflects the interaction

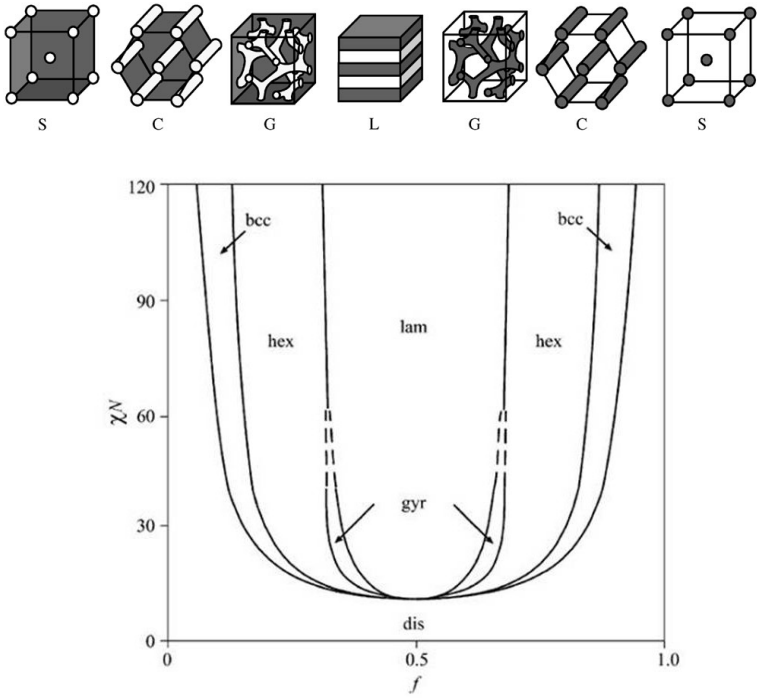

Figure I.13: Phase diagram for symmetric diblock copolymer calculated with the self-consistent field theory. Regions of stability of disordered (dis), lamellar, (lam), gyroid (gyr), hexagonal (hex), and body-centered cubic (bcc) phases are depicted.

energy between different segments (Fig. I.13). In the melt of a diblock copolymer, where both polymer chains are amorphous, a number of ordered structures are stable below the order-disorder transition (ODT), depending on the composition of the copolymer specified by the volume fraction of one component, *f*, the degree of polymerization, N, and the temperature which is contained in the Flory-Huggins

interaction parameter $\chi = A/T + B$, where A and B are constants dependent on the system.

The most commonly studied semicrystalline block copolymer systems are AB diblock copolymers or ABA triblock copolymers, where one block is amorphous and the other semicrystalline. Referring to the above discussion, the changes of state as a function of temperature can design the final morphology according to three key transition temperatures: the order–disorder transition (ODT) temperature, T_{ODT}, the crystallization temperature, T_c, of the crystallizable block, and the glass-transition temperature, T_g, of the amorphous block.

For confined crystallization, the inter-domain connectivity through grain boundary, edge and screw dislocations can play an important role. It is noteworthy that the degree of isolation is the highest in the spherical phase, and decreases for the hexagonal cylinder (Hex) and lamellar (Lam) phases. It was found that when the microdomains were relatively isolated homogeneous nucleation determined the crystallization process. The experimentally accessible T_c's were thus much lower than those in the unconfined crystallization[73].

I.4.1 *Annealing of block copolymers*

Most of the annealing experiments work on semicrystalline diblock copolymers has focused on bulk and thin film systems, in addition to works on annealing in a solvent medium in view to study their aggregates behavior.[74 -76] Thin films of block copolymer have been studied extensively because of their potential applications as templates to fabricate nano-structured materials. These studies aimed at understanding the process of microphase separation and at elaborating new structured material with different mechanical properties suitable for potential applications.[77-79] However, it should be mentioned that a few studies were dedicated to the annealing behavior of diblock copolymer single crystals, which was identified as an objective in its own.[80] Thus *Cheng* and coworkers extended their study on PS-b-PEO systems in the bulk state, and recently also on annealing of individual single crystals and single crystal mats.[81,82]

I.5 Grafted polymer chains

Since our work is focused on single crystals of crystalline-amorphous diblock copolymers, which contain amorphous block tethered to the crystalline surface, it is important to briefly review the behavior of polymer brushes end-grafted to

a surface. Compared to polymers in solution, a new length scale is present in grafted systems: the distance between grafting points $\sqrt{S}$ with S being the average area per polymer chain at the interface (Fig. I.14). Polymer brushes have important technological applications, which range from colloidal stabilization and lubrication to nanoparticle formation at the polymer brush/air interface. In biological sciences, there is a growing interest in polymer brushes as model systems of cell surfaces.

The tethering density is the reciprocal of the area of one tethered chain and is used to describe how close a tethered chain is to its neighbors:

$$\sigma = \frac{1}{S} \qquad \text{I.38}$$

The reduced tethering density Σ, proposed by Kent[83] has been defined as:

$$\Sigma = \sigma \pi R_g^2 \qquad \text{I.39}$$

where R_g is the radius of gyration of a tethered chain at its end free state in the same conditions (i.e., solvent and temperature).

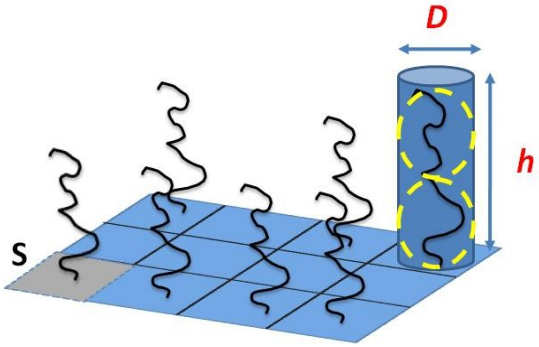

Figure I.14: Schematic drawing of polymer chains grafted on a flat surface.

Such definition provides a parameter which is independent of the molecular weight of tethered chains and the type of solvent used. The physical meaning of Σ can be understood as how many tethered chains are in an area of $\sigma\pi R_g^2$ which is covered by a free chain in the same environment. As illustrated in figure I.15, three brush regimes can be identified, which are characterized by the chain separation and conformation of the grafted chains.

I.5.1 *Polymer brush regimes*

The "true brush" or highly interacting regime can be approached at a significantly high stretching of polymer chains that is typically characterized by $\Sigma \gg 1$ (cf. Fig. I.15). However, this value is strongly affected by excluded volume and can vary from system to system. When tethering is

sufficiently dense the polymer chains are crowded and have to stretch away from the surface or interface to avoid overlapping, sometimes much farther than the typical unstretched size of a chain.

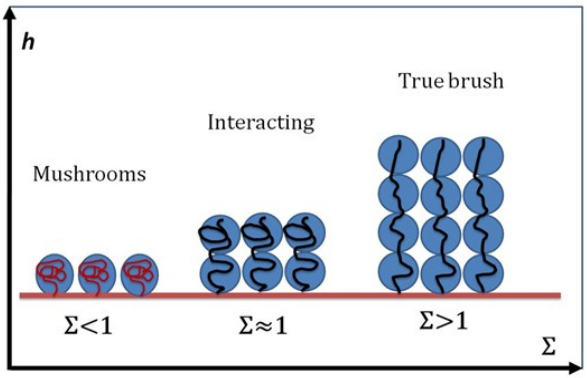

Figure I.15: Schematic representation of the tree different tethering regimes and the thickness of tethered chains (h) versus reduced tethering density (Σ).

When $\Sigma \approx 1$ the size of grafted polymer chains approaches the distance between grafting points, and tethered chains start to interact and overlap. This point is a transition between a single grafted chain (mushroom) regime and a stretched brush regime. The "mushroom" or weakly interacting regime, $\Sigma < 1$, chains don't overlap and the distance between two chains is larger than the unperturbed dimension of the molecules.

I.6 Major characterization techniques for studies of polymer crystallization

The characterization techniques applied to semicrystalline polymers are in continuous evolution. Electron microscopy is probably a unique tool allowing simultaneous observations in both direct and reciprocal space with significant spatial resolution. However, since this technique is typically limited to very thin samples, there was always interest in using X-ray scattering techniques. The advances achieved with the advent of synchrotron radiation and novel acquisition tools allow more precision and accuracy in X-ray scattering measurements on polymers. For example, new micro- and nano-focus facilities open the way of studying polymers with spatial resolution comparable to that of the electron microscopy. The invention of AFM and the widespread usage of this popular technique in the 90's stimulated researchers to undertake studies aimed at visualizing polymer surfaces at the nanoscale. In the next chapter, we will describe in more detail the experimental techniques used in the study. However before starting this discussion, we would like to state the main objectives of our work and the plan of the thesis.

I.7 Aims and scope

The present study is dedicated to the general understanding of polymer crystallization. It focuses on the role of the surface free energy in formation of crystalline lamellar structures and in defining their thermal stability. The system selected for the study is a semi-crystalline diblock copolymer of PS-*b*-PEO. In particular, we studied single lamellar crystals grown from dilute solution. The crystalline lamella represents the basic structural entity of the semicrystalline polymer structure, which is in this case formed without any confinements and constraints imposed by the surrounding medium. We will be interested in the detains of the semicrystalline structure of these objects and their structural evolution during temperature annealing. We believe that the main originality of this study is in the morphological characterization of the system at very different spatial scales such as the atomic scale addressed by WAXS and the lamellar scale addressed with a combination of variable temperature SAXS and AFM. The role of the amorphous PS chains on the final structure will be discussed.

In the second chapter, different samples of diblock copolymers of PS-b-PEO, strategies of single crystal

preparations and technical instrumentations and measurement tools will be described.

In the third chapter, the analysis methodology for AFM images and SAXS/WAXS data are described.

In the fourth chapter, the morphology of single crystals of PS-*b*-PEO diblock copolymers is explored by means of AFM and SAXS/WAXS. The single crystal morphology will be tentatively correlated to the extra free energy of the surface due to the state of the amorphous PS segments tethered to the lamellar surface. The diffrentt regime for amorphous brush and the passage from the mushroom to the true brush regime will be discussed in this context. Also, the configuration of the single crystal in the native mother solution will be presented.

In the fifth chapter, the annealing behavior of individual single crystal and mats of stacked single crystals for different initial morphology will be studied under real time AFM and SAXS/WAXS. A thermodynamic scheme for evolution of the polymer single crystals of diblock copolymers will be presented.

At the end, the general conclusions of the work will be given.

References

1. Yamakawa, H (1971) Modern Theory of Polymer Solutions. Harper & Row, New York
2. de Gennes, PG (1979) Scaling Concepts in Polymer Physics. Cornell University, Ithaca
3. Grosberg, AY; Khokhlov, AR (1994) Statistical Physics of Macromolecules. AIP Press, New York
4. Rubinstein M (2003) Polymer Physics. Oxford University Press, Oxford
5. Abitz,W.; Gerngross, O.; Hermann, K. *Nature* **1930**, *18*, 754
6. Jacodine, R. *Nature* **1955**, *176*, 305
7. Till, P. H. *J. Polym. Sci.* **1957**, *24*, 301.
8. Fischer, E. W. *Z. Naturforsch. Teil A* **1957**, *12*, 753
9. Keller, A. *Philos. Mag.* **1957**, *2*, 1171
10. Geil, P. H. (1963*)* Polymer Single Crystals, Interscience, New York/London.
11. Storcks, K. H. *J. Am. Chem. Soc.* **1938**, *60*, 1753.
12. Flory, P.J. *J. Amer. Chem. Soc.* **1962**, *84*, 2857
13. Kovacs.A. J.; Gonthier, A., *Kolloid. Z. Z.* , **1972**, *250*, 530.
14. Kovacs A. J., Gonthier.A., Straupe.C. *J. Polym. Sci. Polym. Symp.* **1975**, *50*, 283.
15. Kovacs, A. J.; Gonthier.A., Straupe.C. *J. Polym. Sci. Polym. Symp.* **1977**, *59*, 31.
16 Lotz, B; Kovacs, A.J. *Kolloid ZZ Polym.* **1966**, *209*, 97.
17. Keller, A.; Goldbeck-Wood, G.; Hikosaka M., *Faraday Discuss.,* **1993**, *95,* 109.
18. Takahashi, Y. and Tadocoro, H. *Macromolecules* **1975**, *6*, 672.
19. Takahashi, Y.; Sumita, I.; Tadokoro, H. *J Polym Sci, Polym Phys Ed* **1973**, *11*, 2113.
20. Gua, F.; Bu, H.; Zhang, Z. *Polymer* **2000**, *41* 7605–7609.
21. Takahashi, Y.; Tadokoro, H. *Macromolecules* **1973**, *6*, 672.
22. Tadokoro, H.; Chatani, Y.; Yoshihara, T.; Murahashi, S. *Makromol Chem.***1964**, *73*, 109.
23. Yokoyama, M.; Ishihara, H.; Iwamoto, R.; Tadokoro, H. *Macromolecules* **1969**, 2, 184.
24. Spevacek, J. ; Paternostre, Damman, P. ; Draye , A. C. ; Dosière, M. *Macromolecules*, **1998**, *31*, 3612.
25. Bond lengths are fixed to (C–O, 1.43Å; C–C, 1.54Å; C–H, 1.09Å and the bond angles (O–C–C, 110°; C–O–C, 112.0°; and H–C–H, 109.5°).

26 Lotz, B; Kovacs, A.J. ; Bassett, G.A. ; Keller, A. *Kolloid ZZ Polym.* **1966**, *209*, 115.

27. Chen, J.; Cheng, S. Z. D.; Wu, S. S.; Lotz, B.; Wittmann, J. C. *J.Polym.Sci: Part B: Polym.Phys.* **1995**, *33*, 1851.

28. Wittman, J. C.; Lotz, B. *J.Polym.Sci.Polym.Phys.Ed.* **1985**, *23*, 205.

29. Lotz, B.; Kovacs, A.J.; Bassett, G.A.; Keller, A. *Z. Z. Polym.*, **1967**, *209*, 115.

30. Balta Calleja, F.J.; Hay, I.L.; Keller, A. *Kolloid. Z. Z. Polym.*, **1966**, *209*, 128.

31. Snetivy, D.; Vancso, G.J. *Polymer* **1992**, *33*, 432.

32. Kovacs, A.J. ; Gonthier, A. ; Straupe, C. *J Polym Sci Polym Symp* **1977**, *59*, 31.

33. Kovacs, A.J.; Gonthier, A *Kolloid ZZ Polymer* **1972**, *250*, 530.

34. Kovacs, A.J.; Gonthier, A; Straupe C *J Polym Sci Polym Symp* **1975**, *50*, 283.

35. Cheng, S.Z.D.; Zhang, A.Q.; Chen, J.H. *J Polym Sci Polym Lett* **1990**, *28*, 233.

36. Cheng, S.Z.D.; Zhang, A.Q.; Chen, J.H.; Heberer, D.P. *J Polym Sci Part B Polym Phys* **1991**, *29*, 287.

37. Cheng, S.Z.D.; Zhang, A.Q.; Chen, J.H. *J Polym Sci Part B Polym Phys* **1991**, *29*, 311.

38. Cheng, S.Z.D.; Zhang, A.Q.; Barley, J.S.; Chen, J.H.; Habenschuss, A.; Zschack, P.R. *Macromolecules*, **1991**, *24*, 3937.

39. Cheng, S.Z.D.; Chen JH, Barley JS, Zhang AQ, Habenschuss A, Zschack PR *Macromolecules* **1992**, *25*,1453.

40. Cheng, SZD; Wu, S.S.; Chen, J.H.; Zhou, Q.; Quirk, R.P.; von Meerwall, E.D.; Hsiao, B.S.; Habenschuss, A.; Zschack, P.R. *Macromolecules* **1993**, *26*, 5105.

41. Chen, E.Q.; Lee, S.W.; Zhang, A.Q.; Moon, B.S.; Mann, I.; Harris, F.W.; Cheng, S.Z.D.; Hsiao, B.S.; Yeh, F.; von Meerwall, E.D.; Grubb, D.T. *Macromolecules* **1999**, *32*, 4784.

42. Chen EQ, Lee SW, Zhang AQ, Moon BS, Lee SK, Harris FW, Cheng SZD, Hsiao BS, Yeh F *Polymer* **1999**, *40*, 4543.

43. Lee, S.W.; Chen, E.Q.; Zhang, A.Q.; Yoon, Y.C.; Moon, B.S.; Lee, S.K.; Harris, F.W.; Cheng, S.Z.D.; von Meerwall, E.D.; Hsiao, B.S., Verma, R.; Lando, J.B. *Macromolecules* **1996**, *29*, 8816.

44. Keller, A.; Cheng, S.Z.D. *Polymer* **1998**, *39*, 4461.

45. Zhang, F.; Stühn, B. *Colloid Polym Sci* **2007**, *285*, 371.

46. Cheng, S.Z.D.; Wu, S.S.; Chen, J.H.; Zhou, Q.; Quirk, R.P.; von Meerwall, E.D. *Macromolecules* **1993**, 26, 5105.

47. DiMarzio, E.A.; Guttman, C.M.; Hoffman, J.D. *Macromolecules* **1980**, *13*, 1194.
48. Buckley, C. P.; Kovacs, *Colloid and Polymer Science,* **1976***, 8,* 254.
49. Peterlin, A.; Fischer, E.W.; Reinhold, C. *J. Ghent. Phys.* **1962**, *37*, 1403.
50. Hoffman, J.D. and Lauritzen, J.I., Jr. *J. Research NBS*, **1961**, *65A*, 297.
51. Hoffman, J.D. *SPE Transactions*, Oct **1964**, 315.
52. Keller, A.; O'Connor, A. *Nature* **1957**, *180*, 1289.
53. Keller, A.; O'Connor, A. *Faraday Soc Disc* **1958**, *25*, 114.
54. Kawai, T. & Keller, A. *Phil. Mag.* **1965***, 11*, 1165.
55. Bassett, D.C., *Philos. Mag.* **1964**, *10*, 595.
56. Sadler, D. M.; Gilmer, G. H. *Phys. Rev. Lett.* **1986**, *56*, 2708.
57. Strobl, G. *The Physics of Polymers*. Springer, Berlin (1997).
58. Bassett, D. C.; and Keller, A. *Phil. Mag.*, **1962**, *7*, 1553.
59. Holland, V.F. *J. Appl. Phys.* **1964**, *35*, 3235.
60. Blackadder, D.A.; Schleinitz H.M., *Polymer* **1966,** *7*, 603.
61. Statton, W. O.; Geil, P. H. *J. Appl. Polym. Sci.* **1960**, *3*, 357.
62. Fischer, E. W., and G. Schmidt, *Angew. Chem.* **1962,** *74*, 551.
63. Hauser G, Schmidtke J, Strobl G. Macromolecules **1998**; *31*, 6250.
64. Iijima M, Strobl G. *Macromolecules* **2000**, *33*, 5204.
65. Al-Hussein M, Strobl G. *Macromolecules* **2002**, *35*, 8515.
66. Cho T, Heck B, Strobl G. *Colloid Polym Sci* **2004**, *282*, 825.
67. Kawai, T. *Kolloid Z u Z Polymere* **1965**, *201*, 104.
68. Dreyfuss, P.; Keller, A. *J. Macromol. Sci.-Phys.* **1970**, *B4*, 811.
69. Burmester, A. F.; Dreyfuss, P.; Geil, P. H.; Keller, A. *Polym. Lett. Ed.* **1972**, *10*, 769.
70. Rastogi, A.; Spoelstra, A. B.; Goossens, J. G. P.; Lemstra, P. J. *Macromolecules*, **1997**, 30, 7880.
71. Hamley, I. W. *Adv. Polym. Sci.* **1999**, 148, 113.
72. Hamley, I. W. *The Physics of Block Copolymers*, Oxford University Press, Oxford, 1998.
73. Sun, L.; Zhu, L.; Ge, Q.; Quirk, R.P.; Xue, C.; Cheng S.Z.D.; Hsiao, B.S.; Avila-Orta, C.A.; Sics, I.; Cantino, M.E. *Polymer* **2004**, *45*, 2931.
74. Lin, E.K.; Gast, A.P. *Macromolecules* **1996,** *29,* 4432.
75. Hamley, I. W.; Fairclough, J. P. A.; Bates, F. S.; Ryan, A. J. *Polymer* **1998***, 39*, 1429.
76. Liu, L.; Jiang, B.; Zhou, E. *Polymer* **1996**, 37, *17*, 3937.
77. Rangarajan, P.; Register, R. A.; Adamson, D. H.; Fetters, L.J.; Bras, W.; Naylot, S.; Ryan, A. *Macromolecules* **1995**, *28*, 1422.

78. Gallot, B. Liquid Crystalline Order in Polymers. In *Liquid Crystalline Structure of Block Copolymers*; Blumstein, A., Ed.; Academic Press: New York, 1978; pp 192-235.
79. Rangarajan, P.; Register, R. A.; Fetters, L. J. *Macromolecules* **1993**, *26*, 4640.
80. Yang, J.; Zhao, T.; Zhou, Y.; Liu, L.; Li, G.; Zhou, E.; Chen, X. *Macromolecules* **2007,** *40,* 2791.
81. Cheng, S.Z.D., et al. *Macromolecules* **2008**, *41*, 8114.
82. Cheng, S.Z.D., et al. *Macromolecules* **2008**, *41*, 4794.
83. Kent, M. S. *Macromol. Rapid Commun.* **2000**, *21*, 243.

chapter II Experimental

Sample characteristics, crystal preparation and description of techniques

The present chapter is subdivided in two parts. The first one deals with characteristics of the PS-b-PEO diblock copolymers used in the study and the methods of preparation of single crystals. The second part introduces the techniques and provides a description of the experimental setups. The choice of the techniques employed follow the idea of combining observations in direct and reciprocal space to achieve a more detailed structural description of the crystals. The direct-space measurements were performed essentially using Atomic Force Microscopy (AFM) in Tapping Mode whereas the reciprocal space measurements were done using X-ray scattering at the European Synchrotron Radiation Facility (ESRF), Grenoble, France, at beamlines BM26 and ID2. Other techniques which will be briefly described include Optical Microscopy (OM), Scanning and Transmission Electron Microscopy (SEM, TEM) and Differential Scanning Calorimetry (DSC).

II.1 Materials and sample preparation

II.1.1 *Materials*

Materials used in the present study are linear diblock copolymers of **Poly (Ethylene Oxide)-*block*-Polystyrene** denoted as PS-*b*-PEO have the following chemical formula

$$-[CH_2CH_2O]_n - [CH_2CH(C_6H_5)]_m -$$

Table II.1 lists the different samples and their characteristics, as provided by the synthetic chemists with no further characterization or treatments. The samples of PS-*b*-PEO and PS-*b*-PEO-*b*-PS are characterized by their average number molecular mass M_n and the polydispersity index defined as a ratio of the weight average over the number average molecular mass M_w/M_n. The copolymers were received from three different sources (cf. Table II.1.). Thus a series of copolymers was donated by the Laboratoire de Chimie Macromoleculaire of the Ecole National Supérieure de Chimie de Mulhouse (ENSCMu) France and by the Institute of Technical and Macromolecular Chemistry at the RWTH Aachen, Germany. The triblock copolymer samples were purchased from "Polymer Source Inc.". The block copolymers were synthesized by the classical anionic polymerization and their characterization was carried out with the help of Size

Exclusion Chromatography (SEC) and Nuclear Magnetic Resonance (NMR) techniques.[84]

Table II.1. List of PS-b-PEO samples and their molecular distribution characteristics.

PS-*b*-PEO	N_{PS}	N_{PEO}	M_n^{PS}	M_n^{PEO}	M_w/M_n	W***
40-150*	**38**	**148**	**3952**	**6500**	**1.1**	**0.38**
40-250*	**38**	**249**	**3952**	**11000**	**1.1**	**0.26**
40-445*	**38**	**445**	**3952**	**19600**	**1.4**	**0.17**
40-680*	**38**	**704**	**3952**	**30000**	**1.1**	**0.12**
40-220**	**40**	**220**	**4160**	**9680**	**1.09**	**0.3**
40-380**	**40**	**380**	**4160**	**16720**	**1.13**	**0.2**
50-280**	**50**	**280**	**5200**	**12320**	**1.09**	**0.3**
70-270**	**65**	**270**	**6706**	**11880**	**1.13**	**0.36**
95-270**	**95**	**270**	**9960**	**10880**	**1.12**	**0.47**
190-240**	**192**	**240**	**20000**	**10560**	**1.03**	**0.65**
250-350**	**250**	**350**	**26000**	**15400**	**1.04**	**0.62**

*** Donated by the Laboratoire de Chimie Macromoléculaire, Mulhouse, France**

**** Donated by the Institute of Technical and Macromolecular Chemistry at RWTH Aachen, Germany**

***** W is the weight fraction of polystyrene**

The choice of the samples reflect the main line of this study, i.e. to examine a series of diblocks with fixed molecular weights for the crystallizable or the amorphous block. Also,

the focus is put on the samples where the PS blocks are rather short (e.g. 40 monomers), whereas the length of PEO ranges from 680 to 150 monomers. It is expected that the crystallization and melting behavior of these samples will be significantly different, depending on the constitution and amount of each of the copolymers.

II.1.2 *Preparation of PS-b-PEO single crystals from dilute solutions*

Block copolymers with one crystallizable and one amorphous block can undergo crystallization in dilute solutions to form lamellar crystals. To succeed the single crystal preparation, the first condition to respect is to avoid using a selective solvent for one of the blocks. As a non-selective solvent for PS-b-PEO, *Lotz*[16] reports amyl acetate (pentyl acetate), ethyl benzene and xylene. In the same work, he reports that, for the same condition of concentration and temperature, there is no difference observed in the crystal morphology, but in amyl acetate the growth kinetics is 50 times faster[16]. Another described approach could be to use a mixed solvent such as ethyl-benzene/octane solutions with the weight proportion of 1/1.1.

The second important condition to respect is the correct choice of the incubation temperature. Thus, both of the blocks are dissolved above the dissolution temperature T_d. However since the crystallization temperature T_c is lower than T_d, a chain collapse preventing crystallization can occur if T_c is too low. As a result, only a restricted range of incubation, or crystallization, temperatures is allowed for crystal growth. To these limitations in the crystallization temperature range also comes the fact that the amorphous PS block in solution decelerates the crystal growth rate due to the steric repulsion between the PS coils and, consequently, to the increased surface tension σ_e of the crystal. In the other words, the driving force for crystallization, which is a function of temperature, should be large enough to overcome the different entropic and enthalpic barriers of the crystal growth.

Throughout this work, we used the self-seeding approach to grow single crystals. The two essential advantages of self-seeding are the following: first, the growth starts at the same time for all nuclei and gives rise to single crystals identical in shape and size. Second, the concentration of the nuclei, and thereby the final size of the crystalline units, can be efficiently controlled in a wide range by an appropriate thermal treatment of the sample. Figure II.1 shows AFM images of aggregates of

PS-*b*-PEO crystallites obtained by precipitation without self-seeding for PS-*b*-PEO (40-250) and (190-240) at T_c=25°C in amyl acetate.

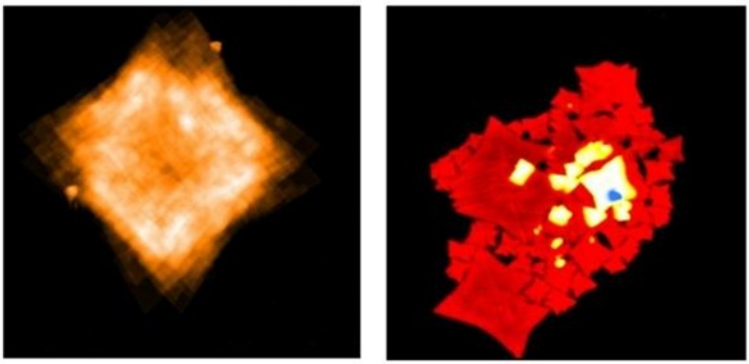

Figure II.1. Aggregates of PS-*b*-PEO crystals obtained upon precipitation from solution without self-seeding. The crystals of PS-*b*-PEO (40-250) and (190-240) grown at T_c=25°C are given in the left and right panels of the figure, respectively.

The first structure (Fig. II.1, left) resembles that of 2D dendrites, and is typical for PS-*b*-PEO copolymers with high and intermediate molecular weight PEO. The second structure (Fig. II.1, right) displays a number of irregular aggregate of single crystals with almost the same shape and thickness but having different sizes. The latter is typical for PS-*b*-PEO copolymers with high molecular weight PS blocks.

Figure II.2 shows a typical product of single crystals grown by the self seeding technique imaged by tapping mode AFM

and STEM, for PS-*b*-PEO (50-280) crystallized at T_c=32°C (left) and PS-*b*-PEO (40-250) crystallized at T_c= 30°C, showing the high uniformity in size and shape of the whole crystal population.

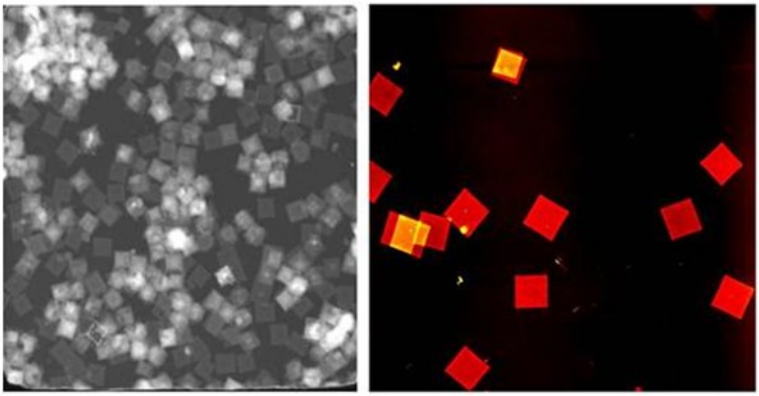

Figure II.2. STEM image of single crystals of PS-b-PEO (50-280) Tc=32°C (left) and AFM height image of single crystals of PS-b-PEO (40-250) T_c= 30°C, showing the uniformity in size and shape.

A typical preparation route was as follows: 1-3mg powder of PS-*b*-PEO diblock copolymer was dissolved in 10-25 ml amyl acetate to form a dilute solution of (0.001-3% wt/wt). The solution was heated to a temperature higher than the dissolution temperature T_d of the diblock in the solvent and kept for about 10-15 minutes to erase the thermal history. The hot solution was transferred to another thermostated bath preset at temperature T_c, and was typically incubated for 24 hours.

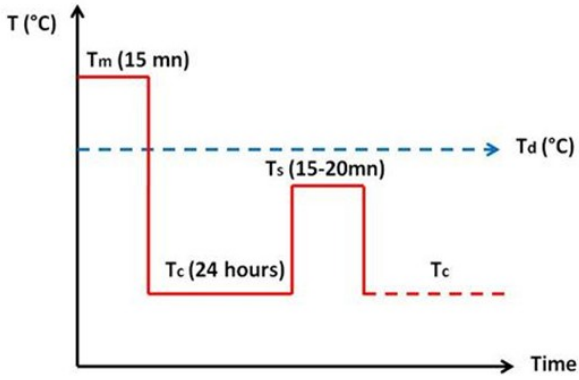

Figure II.3. Typical thermal treatment required for preparation of PS-*b*-PEO single crystals.

After completion of the incubation, the suspension was moved to another thermostated bath at the appropriate self-seeding temperature T_s and held for 15-20 min. Then the solution was again transferred to the previous bath having the same temperature T_c, i.e. the isothermal crystallization temperature. A typical preparation sequence is described in Figure II.3.

For direct microscopic observations, one drop of the crystal suspension was deposited on a flat substrate and the solvent was allowed to evaporate under ambient conditions or under vacuum. For AFM and OM studies the substrate was a silicon wafer while for TEM measurement the substrate was a standard copper TEM grid.

II.1.3 *Preparation of single crystal mats for X-ray investigations*

SAXS/WAXS measurements were performed on mats of single crystals which were collected after sedimentation and evaporation of the remaining solvent under vacuum. Slow sedimentation of single crystals in the mother solution allows obtaining a periodic mat of alternating PS and PEO layers which correspond to a typical two-phase system used for interpretation of the SAXS measurements on semicrystalline polymers.

II.1.4 *Difficulties in sample preparation*

It is well known that PEO is very sensitive to traces of water and oxygen, which could lead to degradation and disorganization of its crystalline structure. This is due to the great affinity of the oxygenic and hydrogenic group to form hydrogen bonding with water or oxygen present in the ambient atmosphere. Thus, manipulation of single crystals of PS-*b*-PEO is very delicate under ambient conditions containing moisture.

However, in the case of diblock copolymers of PS-*b*-PEO, the amorphous PS chains, which are rejected from the crystalline PEO core and covering the top and bottom of the crystal, act as a protective shell against moisture. Once vitrified, PS shell stabilizes the structure against melting and reorganization at elevated temperature. Figure II.4 (left) shows a single crystal of PS-*b*-PEO (40-250) formed at 30°C and kept under ambient air for a week. Circular propagation of the degradation front probably indicates that the process starts in the center and propagates outwards radially.

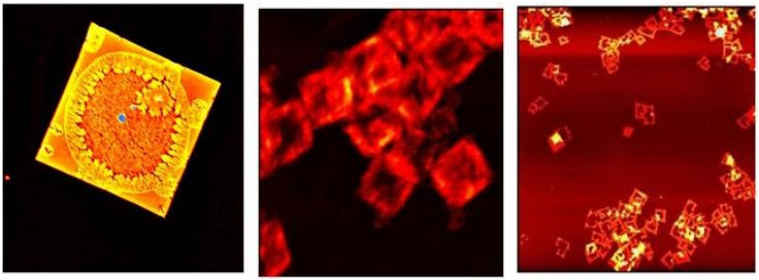

Figure II.4. AFM image of a single crystal of PS-b-PEO (40-250) crystallized at 30°C and kept under ambient air for a week (left). The crystals of PS-b-PEO (190-240) formed at T_c=25°C, which are either taken directly from the "mother" solution (middle) or after washing them with amyl acetate (right).

In our work, we systematically observed that single crystals with high molecular weight (MW) of PEO crystallized at lower crystallization temperature are very sensitive to ambient conditions and consequently are not easy objects for

microscopic investigation. Thus, in the case of high molecular weight PEO the PS shell layer does not sufficiently cover the crystalline lamellae and therefore does not hamper the occasional reorganization of the crystal. On the other hand, lower molecular weights PEO or the crystals crystallized at higher temperature reveal more stability.

Figure II.4 (middle panel) shows single crystals of PS-*b*-PEO (190-240) formed at 30°C. It is clearly seen that some of the material is deposited on the crystal edges and exhibit protruding fingered structures. After washing the crystals before depositing them on a dry substrate, the finger structures disappear. This is indicative of the fact that these structures are formed after deposition of the crystals on the substrate. The structures are not observed for low molecular weight of PS, even if the crystallization in solution is not complete.

Spontaneous structure formation of PS-b-PEO diblocks on surfaces is favorable in air on single crystals formed in solution. *Gast* and coworkers' described "An Intriguing Morphology in Crystallizable Block Copolymers"[85], when crystallizing PS-*b*-PEO (65 EO/80 S repeat units) in dilute solution of cyclopentane. They observe a protruding cylinder

attached to the edges of the square-shaped crystal. According to *Kovacs* and co-workers[86] polarized light microscopy of PS-*b*-PEO solutions in pentanedione provides evidence for cylindrical mesophases having liquid-crystalline order. Other authors also observed such protruding structures and suggested that they are due to a competition between lamellar structure and micelles formation[87].

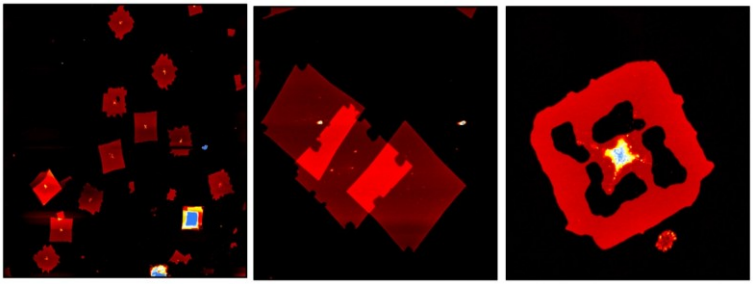

Figure II.5. Room-temperature AFM images of partially-degraded PS-*b*-PEO single crystals formed at 25°C. The images correspond to PS-*b*-PEO (50-280), PS-b-PEO (40-250) and PS-*b*-PEO (40-220) for the left, middle and right panels, respectively.

Summarizing, washing the crystals before sedimenting them on the substrate was found necessary. Unfortunately, it consumes a lot of material and solvent, and can sometimes destroy the crystalline structures as can be seen in figure II.5.

However, the degradation of single crystals does not occur in the same way for all the PS-*b*-PEO diblocks utilized in this study. As can be seen in figures II.5 and II.6 the way the crystals degrade is dependent on the molecular weight ratio of the blocks and on the crystallization temperature. Thus, for a long chain PEO, e.g. PS-*b*-PEO (40-680) (Fig. II.6), which is not completely covered by the PS shell, the destruction starts by rapidly forming holes. The process in this case was so rapid that AFM images taken several minutes after the crystal deposition on the substrate exhibits a completely formed "swiss-cheese" morphology. In the case of longer PS chains (Fig. II.6), the crystal degradation can propagate from the outer edges, from the interior area or from the sectors axes.

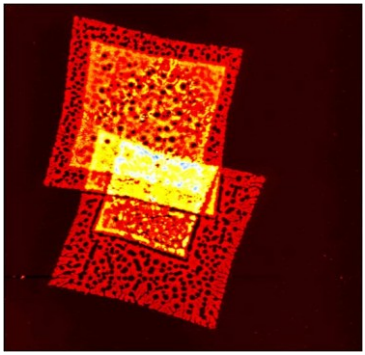

Figure II.6. Room temperature AFM image of solution grown single crystals of PS-*b*-PEO (40-680) formed at 30°C.

Investigations on single crystal mats by means of SAXS can also come across some technical difficulties. Thus the

mats are prepared by sedimentation of the material from the solvent, but the material present in the solvent does not crystallize entirely, especially for the high molecular weight of PS. Therefore the excessive amorphous material can be deposited on or in-between the crystals, which can make the micro-structural parameters such as determined from SAXS studies rather sensitive to the details of the preparation conditions.

II.2 Experimental techniques

II.2.1 *Direct-space techniques - microscopy*

II.2.1.1 Atomic Force microscopy (AFM)

Since the invention of Scanning Tunnel Microscope (STM) by Binning *et al.* a whole family of Scanning Probe Microscopy (SPM) techniques has been developed. Among the large family of the SPMs, the most used and spread technique is Atomic Force Microscopy (AFM). The success of AFM is due to the relatively simple handling, high magnification down to the nanometer scale, no particular exigency for sample preparation, rapid measurement, possibility of working at different conditions as high temperature, controlled atmosphere, pressure, 3D visualization of measured object and

no need for special infra-structure. By these capacities, AFM imposed itself as an efficient alternative to optical and electron microscopy. Furthermore, nowadays AFM is not limited to topographical measurement, but allows accessing rigidity, softness, viscosity, elasticity, adhesion, roughness, electric and magnetic fields.

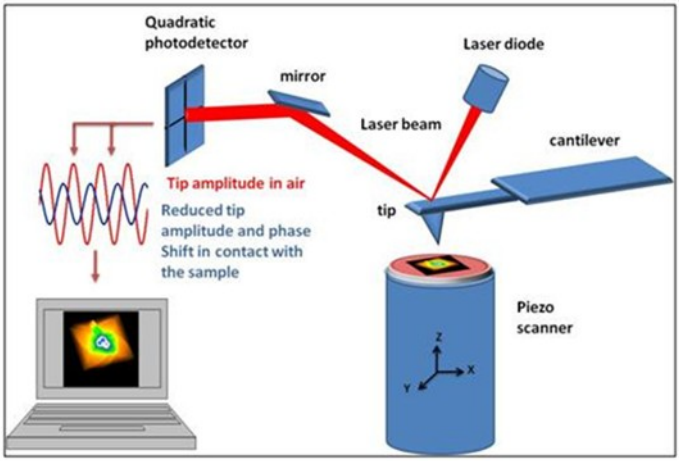

Figure II.7. Schematic drawing of principal components of AFM operating in Tapping Mode.

The functioning principle and major components of AFM are illustrated in figure II.7. When the probe, for instance a sharp tip supported on a micro-cantilever, approaches the surface it feels either repulsive or attractive forces of physical (or chemical) nature.

Forces on the order of a few Nano-Newtons which cause the cantilever to deflect vertically or horizontally, are detected on a quadratic photo-detector sensitive to a laser beam reflected from the cantilever backside. A piezo-scanner capable of moving in angstrom steps, allows the probe to scan a given surface in two directions. The heights detected at each local point are converted to a topographic image matrix or other desired image format.

II.2.1.2 Tapping mode AFM (TM-AFM)

Intermittent-contact known widely as Tapping-Mode (TM-AFM) was developed in the earlier 90's by Digital Instruments in order to allow AFM extending their measurement capacity to involve soft polymeric and biological sample. In TM-AFM the probe is driven close to its resonance frequency above the sample surface, and hence the contact with the sample is very short and the forces exerted on sample are mainly normal to its surface. Another advantage of TM-AFM is that when oscillate near a viscous or elastic surface, the phase of the probe trajectory function is shifted in response to the material mechanics.

In this work, the TM-AFM measurements were performed on a MultiMode microscope equiped with a Nanoscope IV

controller. The probes were standard commercial rectangular shape silicon cantilevers with typical force constant of 21-98 N/m and resonant frequencies of 146-236 KHz.[88]

II.2.2 *Optical microscopy (OM)*

Optical microscopy is capable of resolving structural details on the order of 1 μm, limited by the aperture of the objective lens and wavelength of light. For block copolymers, it allows assessment of melting and crystallization. In this work, we used an Olympus BX51 microscope equipped with a Linkam hot stage to examine the PS-*b*-PEO single crystals. All images were taken in reflection mode using a white light source. Since single crystals are very thin, within typically 10 nm thickness, optical microscope wasn't the main tool in our work. It was mainly used to take a first look on the single crystals population distribution and the sample uniformity.

II.2.3 *Electron Microscopy*

Electron Microscopy experiments were performed with two different microscopes. For Electron Diffraction, a Philips CM200 Transmission Electron Microscope equipped with a lanthanum hexaboride filament and operated at 200 kV. For imaging, Scanning Electron Microscopy (SEM) and Scanning Transmission Electron Microscopy (STEM) experiments were

carried out using a FEI Quanta 400 operated at 30 kV with a tungsten filament.

II.2.3.1 Transmission Electron Microscopy (TEM)

An important advantage of TEM is its capability to combine observations in both direct space and reciprocal space (diffraction mode). In direct space, the image of a thin sample is formed by the unscattered electrons passing through the film without diffraction, the diffracted electrons being stopped by a diaphragm. The contrast in such an image is entirely due to the electrostatic charge density variations in the sample. In the diffraction mode, the image is formed by the diffracted beam. The diffraction pattern can give information on the atomic structure of the sample.

II.2.3.2 Scanning & Transmission Electron Microscopy (STEM)

STEM is similar to SEM except that the electrons pass through the sample to reach the detector placed below. It has the advantage to give information on features present in thin films while being less destructive for sensitive samples than TEM.

The accelerated electron beam is focused on a narrow spot on the sample surface to be analyzed. The interaction between

the sample and the electrons generate secondary electrons of a low energy that are subsequently amplified and detected. The intensity of the signal is relevant to the nature of the material and the sample topography. The image is obtained by scanning the beam over the sample.

II.2.4 *Reciprocal space techniques: X-Ray scattering (SAXS/WAXS)*

The advantages of reciprocal space measurements are in many instances the rapidity, the possibility of the in situ sample monitoring down to the millisecond scale, investigation of bulk samples, as well as universal and relative simplicity of the sample preparation.

II.2.4.1 Experimental set-ups

Synchrotron X-ray radiation sources are characterized by high brilliance. In addition, these sources allow for a relatively wide energy variation. The different beamlines provide a great variety of experimental setups ranging from standard scattering experiments in transmission to more specialized applications like micro- and nano-focus X-ray diffraction or grazing incidence scattering. In this work, X-ray measurements, at small and wide angles were carried out at the

European synchrotron Radiation Facility ESRF, Grenoble, at the ID02 and BM26 beamlines.

II.2.4.1.1 BM26 at the ESRF

The X-ray beam at BM26 beamline (cf. Fig. II.8) is generated by a bending magnet. Once produced, the X-ray beam travels through a first slit of a Si (111) double-crystal monochromator, followed by a meridionally focusing mirror, two further slits, before reaching the sample at 47 meters from the source.

Ion chambers placed directly upstream and downstream the sample allow to monitor the photon flux of the incoming and transmitted X-ray beam essential for intensity and absorption correction to the collected data which is extremely important while performing real time measurements.

The SAXS detector is a 2D Multiwire Proportional Counters gas detector (MWPC), 512x512 pixels, 13.3x13.3 cm^2 , with a counts rate of 1000 Cs/sec/channel and spatial resolution of 400-500μm. The SAXS detector is moveable from 1.4 up to 10 meters away from the sample. A Charge Coupled Device (CCD) WAXS camera is mounted in front of the scattered beam, above the entry of the SAXS tube, allowing simultaneous SAXS and WAXS measurements.

II.2.4.1.2 ID02 at the ESRF

The ID02 beamline (cf. Fig. II.8) is characterized by a high brilliance due for the undulator source of the X-ray beam. ID02 is especially designed to probe soft matter and related systems with up to millisecond time resolution.

The beamline optics consists of a Si (111) monochromator, a focusing torroidal mirror, two collimation slits, one before the monochromator at 29 m and the other after the mirror at 50 m and two further guard slits located at 53 m and directly before the sample at 55 m.

Figure II.8. Experimental hutch at the BM26 beamline showing the SAXS installation (left). The setup for the real-time simultaneous SAXS and WAXS measurements at beamline ID2 at the ESRF, Grenoble, France (right).

The standard beam size is 200 μm x 400 μm with a low divergence of 20 μrad x 40 μrad, and a fixed wavelength around 0.1 nm (12.4 keV).

The SAXS detector is a FReLoN Kodak CCD which is a fiber optically coupled CCD based on Kodak KAF-4320 image sensor. Mounted on a wagon inside the 12 m detector tube the sample-to-detector distance can be varied from 1 m to 10 m. The combined SAXS/WAXS setup can provide a frame rate of 10 images per second.

II.3 Thermal analysis techniques

II.3.1 *Differential Scanning Calorimetry (DSC)*

Differential Scanning Calorimetry (DSC) is the most frequently used thermal analysis technique in polymer science. The principle of a heat-flux DSC consists in measuring the difference in heat flows between a sample and reference as a function of temperature. The differences in heat flow arise when the sample absorbs or releases heat due to thermal effects such as melting, crystallization, chemical reactions, polymorphic transitions, vaporization and other processes. Specific heat capacities and changes in heat capacity during a

glass transition can also be determined from the difference in the heat flow.

A Mettler-Toledo heat-flux DSC 822^e was used. The apparatus calibration was done with a standard calibrant as In and the sample chamber was kept under a constant flux of nitrogen. Inside a sealed aluminum pan, typically from 1 to 3 mg of PS-b-PEO single crystal mats and 5-10 mg of bulky materials was used for measurements. Special care was taken as to the thermal history of samples and heating ramp rates to be used.

II.3.2 *In situ observations at variable temperatures*

II.3.2.1 Time-resolved SAXS/WAXS measurements

Different sample environments are available at the ID2 and BM26 beamlines. Real-time measurements were performed using a standard Linkam heating stage, (THMS600/TMS94 at ID2 and HFS 191 at BM26). It performs fast temperature ramping and quenching (up to 80 °C/min, with stability of 1 °C) over a wide temperature range from -100 to 600 °C.

II.3.2.2 In-situ Tapping Mode AFM measurements

In-situ AFM investigations of the morphology evolution were performed using a TM-AFM with the help of a special accessory designed for measurements in a controlled environment and temperature. The hermetic furnace, incorporated within a JVH type scanner, is controlled with temperature stability better than 0.1 ºC and ranging from room temperature up to 250°C. Figure II.9 shows the different components and accessories of the high-temperature AFM accessory.

Figure II.9. Digital Instruments MultiMode microscope head with the thermal accessory installed (right); temperature controller (middle) and components of the thermal accessory assembled on the piezo-scanner (left).

II.4 References

84. Hurtrez, G, Study of PS-PEO and PEO-PS-PEO block copolymers (in French). PhD Thesis. University Haute Alsace, France; 1992.
85. Gast, A.P.; Vinson, P.K.; Cogan-Farinast, K.A. *Macromolecules* **1993**, *26*, 1774.
86. Wittmann, J. C., Lotz, B., Candau, F., Kovacs, A. J. *J. Polym Sci., Polym. Phys.* **1982**, *20*, 1341.
87. Huang, W.; Luo, C.; Zhang. J. ; Yu, K. ; Han, Y. *Macromolecules* **2007**, *40*, 8022.
88. Magonov, S. N.; Yerina, N. A.; Ungar, G.; Reneker, D.H.; Ivanov, D.A. *Macromolecules* **2003**, *36*, 5637.

chapter III Data processing and analysis

In this chapter the details of the data reduction and analysis are described for the main experimental techniques employed in the study.

III.1 AFM image analysis and processing

As all instrumentation, SPM imaging generates results that may contain artifacts and should be examined with care. There are four primary sources of artifacts in images measured with atomic force microscopes. They are: Probes, Scanners, Image Processing and eventually external vibrations.

As described in chapter II, the raw data files were collected on Nanoscope software from Digital Instruments Inc. as Nanoscope file format. Treatments and morphological analysis of the data were performed with home-built routines and procedures running in IGOR Pro (Wavemetrics Ltd) software[89,90].

III.1.1 *Artifact sources*

III.1.1.1 Probe Artifacts

Images measured with an atomic force microscope always present a combination of the probe geometry and the morphology features being imaged. If the probe is much smaller than the features size, the probe-generated artifacts will be minimal and the dimensional measurements derived from the images will be accurate. In this way the lateral resolution in the x-y direction is limited by the probe shape

and dimensions, the probes used in this study are commercial silicon probes with a typical apex radius less than 15nm.

III.1.1.2 Scanner Artifacts

Scanners that move the sample in the X, Y and Z directions are typically made from piezoelectric ceramics. However, when a linear voltage ramp is applied to the piezoelectric ceramics, the ceramics motion is highly nonlinear. Furthermore, the piezoelectric ceramics exhibit hysteresis effects. Often the images measured by AFM include a background "Bow" and a background "Tilt" that are stronger than the features of interest. In such cases the background must be subtracted from the image, i.e. the often called "leveling" or "flattening".

III.1.2 *Preprocessing (flattening)*

Before any morphological treatment of AFM images, the first step is to correct the background caused during image acquisition (sample tilt, scanner bow / nonlinearities, z-drift, line skips, etc.). There are two common approaches to leveling:

- Surface flattening, 0 to 4th order polynomial function;
- Line-by-line flattening, 0 to 4th order polynomial function.

The background can be either linear or polynomial with order typically going up to four. The flattening type and order is generally in relation with the scan size.

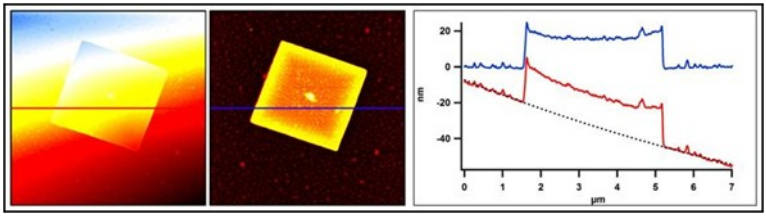

Figure III.1. Typical AFM height images, non-flattened (right) and flattened (middle). The non-flattened cross-section was fitted using a mask and then subtracted with a linear background (dashed line).

In figure III.1 (left), we show non-flattened AFM height images with one corner higher than other due to a sample tilt. The correction was made by firstly excluding the featured object from the image, and then fitting each scan line, either in X or Y direction, to a linear line, and then the linear background was subtracted from each line, as shown on the right panel of the image.

III.1.3 *Image Processing and Morphological Evaluation*

After correction for the background, AFM height images are subject for further analysis to evaluate the different morphologies of the samples.

III.1.3.1 Histogram Calculation

The histogram of an AFM height image represent the distribution of the different Z (height) values within the image matrix. The histograms in Igor Pro were calculated using 512 bins to obtain the required height resolution. It is noteworthy that higher bin numbers cause the histogram to be noisy. The y value of the histogram is the total of number of input values (Z) that fall within each bin. The first piece of information conveyed by the histogram, is the height of the object, as well as its shape. The latter can be accessed from the shape of the thickness distribution of. As shown in figure III.2, two major peaks appear in the histogram, which correspond to the substrate and object. The object peak can be clearly seen as a trimodal peak. During annealing of the single crystals, the evolution of the histogram allows a direct

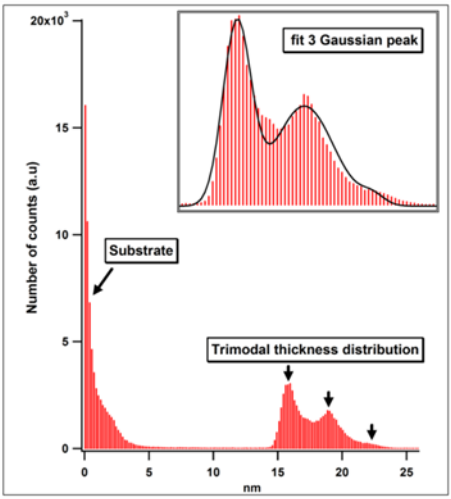

Figure III.2. Typical histogram of a topographic AFM image, with a trimodal thickness distribution.

quantification of the lamellar re-organization and melting. Furthermore, the histogram is essential for the operations of the image edge detection and thresholding, which will be discussed in the next section. Thus the discrimination of different thickness levels is performed by thresholding and extracting a localized and specific range of thickness on the basis of the histogram's statistics.

III.1.3.2 Thicknesses discrimination

Thicknesses discrimination is performed with the help of the image thresholding operation. First, the image thresholding operation detects the edges of sudden changes of the height values over all the range of the image. Then, the edges detected are converted to a mask waves to define an

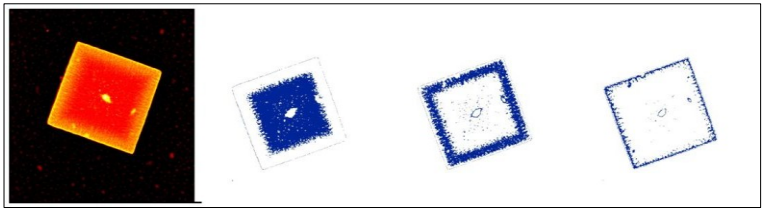

Figure III.3. Initial AFM image and three thresholding views highlighting the regions of interest.

automatic region of interest (ROI) on the basis of the height jumps. Afterwards, the image is binarized . The ROI is assigned to 1 and the rest of the image to 0, and then this

matrix is multiplied by the initial image matrix. That operation returns an image of only the selected ROI, while assigning the rest to zero.

III.1.3.3 Quantitative morphology analysis

The morphology of the object was quantified in the IGOR Pro routines by means of its perimeter, area, volume, rectangularity, circularity, and the maximum of height distribution from the histograms.

W_circularity is defined as a ratio of the square of the perimeter to (4*pi*objectArea). This value approaches 1 for a perfect circle.

W_rectangularity is defined as a ratio of the area of the particle to the area of the inscribing (non-rotated) rectangle. This ratio is pi/4 for a perfect circular object and unity for a non-rotated rectangle.

M_ParticlePerimeter is defined as masking image of particle boundaries. It is an unsigned char wave that contains 0 values for the object boundaries and 64 for all other points.

M_ParticleArea is defined as a masking image of the area occupied by the particles. It is an unsigned char wave that contains 0 values for the object

boundaries and 64 for all other points. It is also different from the input image in that the particles smaller than the minimum size, specified by the flag /A, are absent.

M_Particle is defined as a masking image of both the area and the boundary of the particles. It is an unsigned char wave that contains the value 16 for object area, the value 18 for the object boundaries and the value 64 for all other points.

A typical particle analysis consists of three steps. First we performed a preprocessing of the image. This may include noise removal or reduction, background adjustments and thresholding. Once the binary image is obtained, the second step is to execute the **ImageAnalyzeParticles** operation. Issues related to the preprocessing have been discussed above in this chapter. We will assume that we are starting with a preprocessed, clean, binary image which contains some particles.

III.1.3.4 Volume of the object

The object volume is calculated by integration of the area of the histogram corresponding to the object of interest, which means the multiplication of a given height by their

corresponding surface. Thus, before performing the integration, the scale of the y axis is converted to a surface dimension scale. Knowing that the y axis of the histogram is a number of pixels, we convert each pixel to its metric dimension, which is the total number of pixels divided by the calibrated surface area of the image.

Upon calculating the object volume, one can know the volume fractions of the copolymer blocks the crystalline and amorphous volume. Defining the crystalline and amorphous thickness as L_c and L_a, respectively, one obtains:

$$V = V^{PS} + V^{PEO} = V^{PS} + V_c^{PEO} + V_a^{PEO} \qquad \text{III.1}$$

In the above equation, V is the total volume of the crystal calculated from the histogram; V^{PS} -the volume of the amorphous PS layer; V_c^{PEO} and V_a^{PEO} are the crystalline and the amorphous volumes of the PEO block.

On the other hand, the average mass molecular weight for different samples of copolymers is known[91] , and the mass ratio **w** can be written as:

$$w = \frac{M_n^{PEO}}{M_n^{PS}}$$

$$= \frac{\left[\rho_{PEO}^{c} + \rho_{PEO}^{a}\left(\frac{1-\emptyset_c}{\emptyset_c}\right)\right] V_c^{PEO}}{\rho_{PS} V^{PS}} \qquad \text{III.2}$$

In Eq. III.2, $\emptyset$ is the volume crystallinity, or the crystalline fraction of PEO, and is given by:

$$\emptyset_c = \frac{V_c^{PEO}}{V_c^{PEO} + V_a^{PEO}} \qquad \text{III.3}$$

In fact, mass crystallinity in the case of polymer single crystal grown from dilute solution is related to the amorphous quantity or volume of non-crystallized PEO segments forming the folds, bridge chains or cilia. The mass crystallinity is defined by:

$$\chi_c = \frac{M_c^{PEO}}{M_c^{PEO} + M_a^{PEO}} \qquad \text{III.4}$$

In the other hand the mass of a chain involved within the crystal, is distributed between the crystalline part, and the amorphous part in the cilia and fold, thus, we can write:

$$M_n^{PEO} = M_{crystal}^{PEO} + M_{fold}^{PEO} + M_{cilia}^{PEO} \qquad \text{III.5}$$

Replacing the mass in its equivalent in length dimension, which is given by $M_n^{PEO} = \frac{pLM_u^{PEO}}{l_u}$, where p is the degree of polymerization, l_u the unit length of PEO monomer assumed to be equal in the crystalline and amorphous state, and L is the contour or total length of the chains. Thus we can rewrite equation III.5 in another form in terms of lengths as:

$$L = l_{crystal}^{PEO} + l_{fold}^{PEO} + l_{cilia}^{PEO} \qquad \text{III.6}$$

If the chains contain n+1 crystalline stems, meaning that there are n folds, however only one cilia can be engaged in termination of the PEO block, since the other extremity is linked to the PS block. Therefore we can write:

$$L = (n+1)L_c + nL_f + L_{cilia} \qquad \text{III.7}$$

Then we can deduce the degree of crystallinity by combining equations III.7 and III.4 :

$$\chi_c = \frac{L_c}{L} = \frac{1}{n+1}\left(1 - n\frac{L_f}{L} + \frac{L_{cilia}}{L}\right) \qquad \text{III.8}$$

In fact, if we neglect the unit length of monomer difference between the crystalline and amorphous phases, we can assume that the volume and mass crystallinity is identical.

Now by combining equations III.1 and III.2 one can find the crystalline volume V_c^{PEO} to be:

$$V_c^{PEO} = \frac{\emptyset_c w \rho_{PS}}{\emptyset_c \rho_{PEO}^c + (1-\emptyset_c)\rho_{PEO}^a + w\rho_{PS}} V \qquad \text{III.9}$$

And we can deduce the crystalline and amorphous thicknesses, L_c and L_a, by dividing the volume over the surface of the crystal, as follows:

$$L_c = \frac{V_c^{PEO}}{S} \qquad \text{III.10}$$

$$L_a = \frac{V^{PS} + (\frac{1-\emptyset_c}{\emptyset_c})V_c^{PEO}}{S} \qquad \text{III.11}$$

After rearrangement one finds the expression for the L_c:

$$L_c = \left(\frac{w\rho_{PS}}{\rho_{PEO}^c - \rho_{PEO}^a}\right) LB - \left(\frac{\rho_{PEO}^a + w\rho_{PS}}{\rho_{PEO}^c - \rho_{PEO}^a}\right) L \qquad \text{III.12}$$

where LB stands for long period.

III.2 X-ray data analysis

In this section, procedures and methods of data reduction and processing are described. 2D scattering patterns are used as raw data for the experiments carried out at the BM26 beamline. The results from ID2 beamline are obtained as 1D scattering curves after correction at the beamline. Home-built procedures written in IGOR Pro are used in the data reduction.

III.3 Primary SAXS and WAXS data treatment

Correction for the sensitivity of the detector

Detectors, used for the detection of small angle scattering data are usually gas-filled multi-wire proportional counters (MWPC). MWPC counters are formed of one- or two-dimensional arrays (often 512x512 channels) of parallel wires held at high voltage in a mixed gas filled atmosphere. The principle of operation of gas detectors is based on the

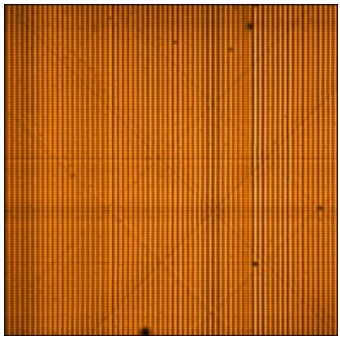

III.4. Typical 2D SAXS pattern of the response of the MWGFD detector to a radioactive source.

collection and amplification of photo-electrons, liberated in a suitable gas mixture by the photoelectric effect when the X-rays pass through the gas volume. But, each channel of the detector does not have a uniform response to the incident X-ray photons (cf. Fig. III.4). To compensate for this effect one has to divide the collected raw data patterns by the detector sensitivity pattern acquired as a response signal to a radioactive source.

In the second step the measured intensities are normalized for the intensity of the incoming beam and sample absorption.

III.3.1.1 Calibration of the s vector

In order to compute the s vector corresponding to the X-ray image on an area detector, standards like silver behenate (AgBe) powder were used systematically. AgBe has the specificity to have intense isotropic scattering over a wide s range, in both SAXS and WAXS regions. The first order Bragg reflection is known to be at 58.4 Å.

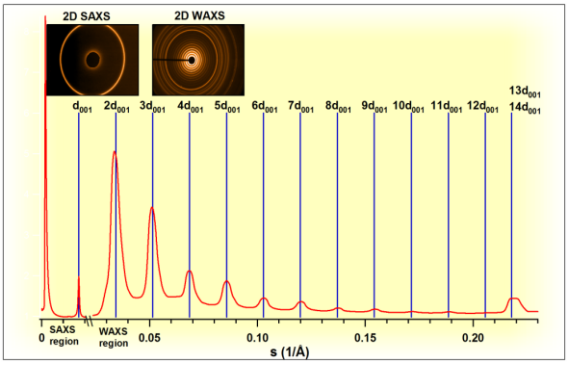

Reflection	s, 1/Å	d, Å
d_{001}	0.017	58.37
$2d_{001}$	0.034	29.185
$3d_{001}$	0.051	19.456
$4d_{001}$	0.068	14.593
$5d_{001}$	0.085	11.674
$6d_{001}$	0.102	9.728
$7d_{001}$	0.119	8.338
$8d_{001}$	0.137	7.296
$9d_{001}$	0.154	6.485
$10d_{001}$	0.171	5.837
$11d_{001}$	0.188	5.306
$12d_{001}$	0.205	4.864
$13d_{001}$	-	-
$14d_{001}$	0.217	4.591

Figure III.5. Calibration of the norm of the s-vector using AgBe.

The pattern center is determined by finding the geometrical centre of the equidistant diffraction rings. Thereafter the detector to sample distance is calculated using the equation $n \lambda = 2 d \sin\theta$. Due to small angles in SAXS patterns, one diffraction peak is normally enough to obtain an accurate calibration, as shown in figure III.5.

For the WAXS calibration, more care should be exercised, as the detector does not show a linear relation of the norm of s with the radius. More peaks, normally between 7 and 12 orders of reflection of AgBe will be identified and used in the calibration.

III.3.1.2 Background correction

Scattering that does not originate exclusively from the sample but also from the sample environment (air-scattering,

scattering on windows, solvent scattering, etc.) an appropriate background scattering should be subtracted from the collected data. The experimental data and background should first be normalized as described above.

III.3.1.3 Correction for the case of isotropic scatterers (Lorenz correction)

The Lorenz correction is applied to the data in order to account for the geometry of isotropic samples. It is performed by multiplying the intensity of each data point by the corresponding surface of the reciprocal space sphere, i.e. the s-value squared. However, this correction is only valid for isotropic samples. In the case of oriented samples such as the single crystal mats, the Lorenz factor can be different.

III.4 SAXS data evaluation by direct method

Two main approaches are available to deduce structural information contained in a given SAXS data. The direct method applies a model function (e.g. paracrystalline model) directly to the experimental data in reciprocal space while the indirect method basically uses Fourier transforms of the scattering intensity to evaluate the sample structure.

III.4.1.1 Bragg reflections

After integration of the 2D scattering pattern, the intensity of the scattering curve is plotted versus the modulus of the scattering vector s. The first useful information obtained is the position of intensity peak maxima along s. For a lamellar system, of alternating electron density perpendicular to the incident X-ray beam, the position of the first peak obeys the Bragg's law and the position of higher order if any, is multiplied by an integer number n (2 for the second peak). Thus, according to Bragg's law the average separating distance between two different correlated electron densities, called the long period or Bragg reflection LB is given by:

$$n\lambda = 2(LB)\sin\theta \qquad \text{III.13}$$

For small angles $\sin\theta \cong \theta$, and hence $n\lambda = 2(LB)\theta$, replacing $\frac{2\theta}{\lambda}$ with S, the long period is obtained from the first order peak maxima by $LB = \frac{1}{s}$.

In the case of non-lamellar structure, the position of the higher order relative to the first one is given by their ratio as shown in Table III.1.

The model applied in this case is the two phase system with alternating electron density values with a sharp separating boundary.

Structure	Ratio s/s^*
Lamellar	1: 2: 3: 4: 5: 6…
Hexagonal	1: √3: 2=√4: √7: 3=√9: √11…
Cubic bcc	1: √2: √3: 2=√4: √5: √6 …
Cubic fcc	1: √(4/3): √(8/3): √(11/3): 2=√(12/3): √(16/3) …
Cubic gyroid	1: √(4/3): √(7/3): √(8/3): √(10/3): √(11/3): 2=√(12/3): √(13/3)

Table III.1 Ratios of s/s* for Bragg reflections from various structures

Figure III.6 shows a typical 2D SAXS pattern from a PS-*b*-PEO mat of stacked single crystals illuminated perpendicularly to the c axis of the crystals.

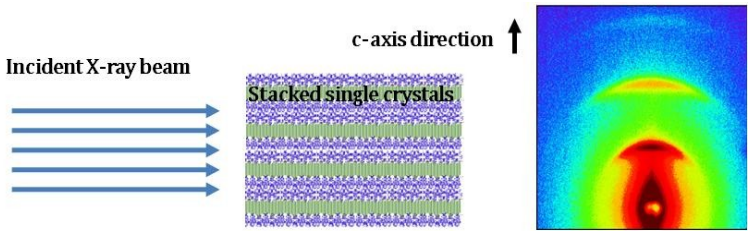

Figure III.6. Sketch of stacked single crystals of PS-b-PEO illuminated perpendicular to the c-axis of the crystals, and a typical oriented 2D SAXS pattern with up to three orders of Bragg reflections and a central diffuse scattering.

The 2D SAXS pattern in Fig. III.6 shows two kinds of scattering typical of dense polymeric systems such as discrete interferences and diffuse central scattering. The diffuse

scattering could result from the micro-voids present in the sample. The micro-voids may be unfilled spaces between the lamellae[92-94]. Discrete interferences appear on the meridian of the 2D SAXS pattern. Up to three orders of the main interference maximum are detected revealing the existence of a periodic structure.

III.4.1.2 Chain Orientation from oriented 2D patterns

Plots of the scattered intensity, $I(\varphi)$, as a function of the azimuthal angle φ, exhibit preferential orientations for scattering from mats of single crystals of PS-*b*-PEO in both wide and small angles. A quantitative evaluation of the degree of orientation of the SAXS and WAXS 2D pattern can be obtained using the Herman's orientation function given as:

$$f = \frac{3\langle \cos^2 \varphi \rangle - 1}{2} \qquad \text{III.14}$$

where φ is the azimuthal angle and $\langle \cos^2 \varphi\, \varphi \rangle$ is given by:

$$\langle \cos^2 \varphi \rangle = \frac{\int_{\varphi_1}^{\varphi_2} I(\varphi) \cos^2 \varphi \sin \varphi d\varphi}{\int_{\varphi_1}^{\varphi_2} I(\varphi) \sin \varphi d\varphi} \qquad \text{III.15}$$

$I(\varphi)$ is the scattering intensity and the limits of integration are between φ_1 and φ_2. The Herman's orientation function f assumes a value of 1 for a system with perfect orientation of the scattering entities parallel to the director and $-1/2$ for the

case where the orientation of scattering entities is perpendicular to the director. For samples with no orientation the value of *f* is zero.

III.5 SAXS data analysis : the case of a two-phase model

III.5.1.1 The ideal two-phase model

The two-phase model is defined as a stratified system containing layers with different electron densities ϱ_e, where the boundary between these two phases is sharp. Figure III.7 shows the electron density variation along the normal to the layers, illustrating discrete steps in the electron density values corresponding in our case either to the PS or PEO blocks. The real system can have a diffuse phase boundary, which can be detected for example from the behavior of the correlation function close to the origin.

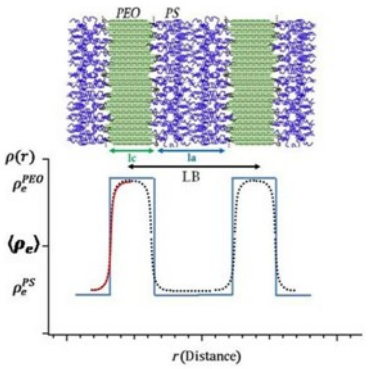

III.7. Sketch depicting the electron density profile for the ideal two-phase system with sharp (continued line) and sigmoidal gradient boundaries (dashed line).

III.5.1.2 Porod law

The Porod law describes asymptotic scattering of an ideal two phase system. It predicts that the intensity I(s) scales as to s^{-4} and that the proportionality constant, the Porod constant K_p, is related to the specific area of the boundaries separating the two phases It can be written as:

$$\lim_{s\to\infty} I(s) = \frac{K_p}{s^4} \qquad \text{III.16}$$

where K_p is given by $K_p = \frac{(\Delta\rho)^2 S}{8\pi^3}$ and S is the specific inner surface.

III.6 Calculation of the 1D correlation function $\gamma_1(r)$

The one-dimensional electron density correlation function $\gamma_1(r)$ is related to the scattering intensity by a Fourier transform. However, several corrections are necessary before proceeding with the Fourier operation. Since the intensity curve is collected over a finite range of s values, the curves may require extrapolation on both sides of the s-interval. The extrapolation to zero s-value can be performed using the Debye–Bueche model[95] as follows:

$$I(s) = \frac{C}{(1 + 4\pi^2\xi^2 s^2)^2} \qquad \text{III.17}$$

In Eq. III.17, C is a constant and ξ is the inhomogeneity length. C and ξ can be determined from the plot of $I(s)^{-0.5}$ versus s^2 using the intensity data in the low s-region. Some other options of acquisition of the low s-value have included linear or polynomial extrapolations of this part of the SAXS curve. However, as was shown in figure III.6 a diffuse scattering is typical for mats of stacked lamellae. To eliminate this effect, the intensity curves at low angles were cut just before the first order interference.

In the case where the interface between the two layers is not sharp (cf. section III.5.1.2), the extension of intensity to large s-values is accomplished according to the Porod–Ruland[96] model:

$$\lim_{s\to\infty} I(s) = \frac{K_p}{s^4} e^{-4\pi^2 s^2 \sigma^2} \qquad \text{III.18}$$

In Eq. III.18 the exponential term accounts for the presence of the crystal/amorphous interface (σ is related to the thickness of the transition layer between crystalline and amorphous regions in lamellar stacks). In this work, the data was fitted in the range $0.01 \leq s \leq 0.03$ Å^{-1} with Eq. III.18, substituted by the fitting results and extrapolated to $s = 0.1$Å^{-1} after subtracting the constant background B. The background is the result of the density fluctuation, leading to a departure

from linearity as depicted from Porod's law, and should be corrected with a function of the form:

$$B = a + bs^n \quad \text{or} \quad B = ae^{-bs^2} \qquad \text{III.19}$$

In Eq. III.19, *a*,*b* and n are constants.

The fully corrected intensity $I_C(s)$ was used to compute the one-dimensional correlation function corresponding to the electron density fluctuations perpendicular to the lamellar basal plane[97]:

$$\gamma_1(r) = \frac{\int_0^\infty I_c(s)s^2 \cos(2\pi rs)\, ds}{\int_0^\infty I_c(s)s^2 ds} \qquad \text{III.20}$$

In the other words, the electron density correlation function is obtained from the real part of the Fourier transform of the fully corrected intensity. The choice of the value for the Lorenz correction will be discussed later. The final form for the computation of the correlation function is as follows:

$$\gamma_1(r) = Re\left\{\int_0^\infty (I_c(s) - B)s^n e^{(2\pi isr + 4\pi^2 s^2 \sigma^2)} ds\right\} \qquad \text{III.21}$$

The correlation function is normalized to unity at the origin.

III.6.1.1 Analysis of the correlation function $\gamma_1(r)$

Figure III.8 shows the micro-structural parameters that can be obtained from the 1D-correlation function. This interpretation assumes that the sample has an ideal lamellar morphology, i.e. it consists of alternating crystalline and amorphous layers forming stacks that are large enough not to affect the small-angle scattering.

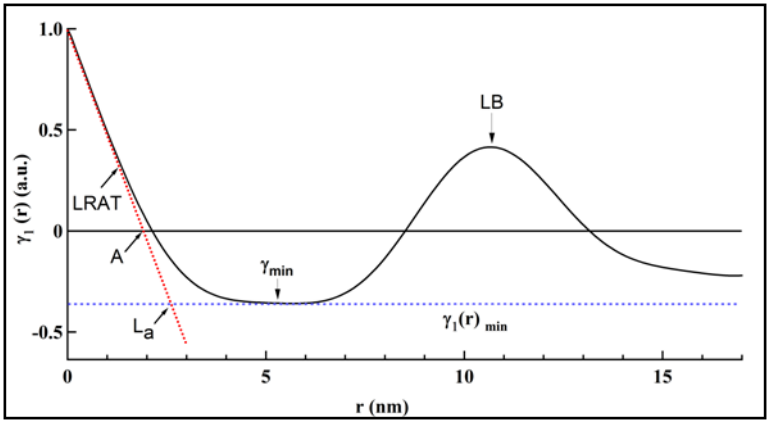

III.8. 1D-correlation function and the main parameters used for its analysis.

The one-dimensional correlation function approach, following the original contribution of *Vonk* and *Kortleve*[97], was designed for homogeneous ideal two-phase systems where a series of triangles centered at $r = 0$, LB, $2LB$, etc., reflect correlations of the lamella with its next neighbors, second neighbors, etc. At the origin, the correlation function forms

the so-called "self-correlation triangle". The horizontal line that passes through the bases of the triangles is called the "baseline". The determinations of *LB*, L_c, L_a, and $\Phi_L=L_c/LB$ may be realized by locating the first minimum and maximum in the correlation function. The long period L_p or LB referred to as the Bragg peak, is estimated from the position of the first maximum of $\gamma_l(r)$. On the other hand, the negative ordinate, γ_{min}, is related to crystallinity Φ_L, as follows

$$\gamma_{\min} = \frac{-\emptyset_l}{1-\emptyset_l}, for\ \emptyset_l < 0.5$$
$$\gamma_{\min} = \frac{1-\emptyset_l}{-\emptyset_l}, for\ \emptyset_l > 0.5 \qquad \text{III.22}$$

So, the first minimum of the 1D correlation function can be used to determine the value of Φ_L if this minimum is flat. Also, the intersection of the linear regression to the self-correlation triangle with the baseline directly yields a value for L_C or La according to the value of Φ_L (e.g., it provides L_C if Φ_L < 0.5).

An alternative way to calculate Φ_L is the solution of the so-called quadratic expression (Q.E.):

$$A = \emptyset_l(1-\emptyset_l)LB \qquad \text{III.23}$$

where A equals the intersection of the LRAT (linear regression to the self-correlation triangle) with the abscissa ($\gamma 1(r) = 0$). This equation yields two possible values for Φ_L. One value is lower than 0.5, the other solution is equal to $(1 - \Phi_L)$. Independent information on the sample crystallinity is needed to decide which solution of Q.E. gives the true value. The lamellar and amorphous layer thicknesses can then be calculated for example as:

$$Lc = \emptyset_l LB, \qquad La = (1 - \emptyset_l) LB \qquad \text{III.24}$$

III.6.2 *The interface distribution function approach*

Further details of the micro-structure of the two-phase system can be analyzed using the interface distribution function (IDF) developed by *Ruland*[98]. The IDF provides a series of the distance distributions with alternating signs, which are composed together (cf. Fig. III.9).

III.6.2.1 Calculation of the interface distribution function $g_1(r)$

The interface distribution function, denoted in this manuscript as $g_1(r)$, can be calculated by two different ways:

1- by the second derivative of the 1D correlation function $\gamma_1(r)$:

$$g_1(r) = \frac{\delta^2(\gamma_1(r))}{\delta r^2} = \gamma_1''(r) \qquad \text{III.25}$$

2- as a Fourier transform of the interference function $G_1(r)$ which is the Fourier transform of the scattering intensity after subtraction of the Porod law:

$$g_1(r) = \int_{-\infty}^{+\infty} G(s)\cos(sr)\,ds \qquad \text{III.26}$$

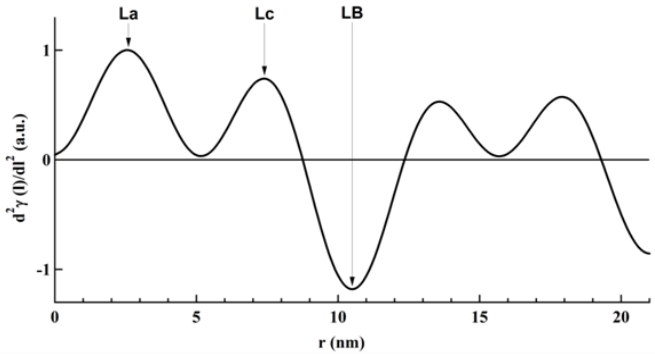

Fig. III.9. The interface distribution function.

This IDF represents the probability distribution of finding two interfaces separated by a distance *r.* The values of the IDF are negative if the two phases are the same and *vice versa.* As shown by *Stribeck* and *Ruland*[99] from the analysis of this function one can obtain LB, L_c, L_a and the width of the corresponding distributions.

III.6.2.2 Impact of Lorenz correction on the IDF and CF

As mentioned previously, the Lorenz correction is applied for the SAXS intensity to account for the isotropic character of the sample. To our knowledge, no analytical approach exist today for the intensity correction of oriented samples with unknown orientation functions. In this work, we decided to follow an empirical approach, where the Lorenz correction factor was chosen between 1.0 and 2.0 in such a way that the CF and IDF are as close as possible to their ideal shapes. Figure III.10 shows the impact of the Lorenz correction factor on these functions. It can be seen that for some values the CF exhibits a spurious secondary maximum at distances around 6-7 nm whereas the IDF becomes negative in the same region. We thus selected the correction factor to avoid these artifacts.

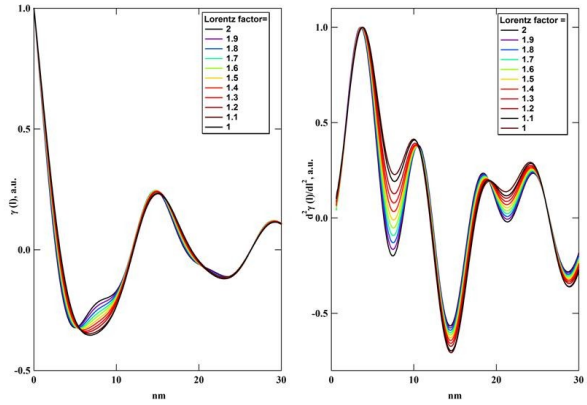

Fig. III.10. Variation of the CF and IDF with the Lorenz correction factor *n*.

III.7 References

89. Basire, C.; Ivanov, D. A. *Phys. Rev. Lett.* **2000**, *85*, 5587.
90. Ivanov, D. A.; Amalou, Z.; Magonov, S. N. *Macromolecules* **2001**, *34*, 8944.
91. We use the data provided with the samples without further characterization.
92. Staton, W. O. *J. Polymer Sci.* **1962**, *58*, 205.
93. W. O. Staton in Newer Methods of Polymer Characterization, B. Ke (editor), Interscience, New York, 1964, Chapter 6
94. Alexander, L.E. X-ray Diffraction Methods in Polymer Science, Wiley- Interscience, New York, 1969.
95. Debye, P.; Bueche, A.M. *J. Appl. Phys.* **1949**, *20*, 518.
96. W. Ruland. *J. Appl. Crystallogr.* **1971**, *4*, 70.
97. Vonk, C.G.; Kortleve, G. *Kolloid Z Z Polym.* **1967**, *220*, 19.
98. Ruland, W. *Colloid Polym Sci* **1977**, *255*, 417.
99. Stribeck, N.; Ruland, W. *J. Appl. Crystallogr.* **1978**, *11*, *535*.

chapter IV Morphology of the PS-b-PEO single crystals

Single crystals of PS-b-PEO diblock copolymers are formed in dilute solutions by folding back and forth of the crystallizable PEO chain to form the crystalline lamellar core. At the same time, the amorphous PS block is rejected outside the growing crystal and accumulates on its basal surfaces. Due to the fact that the single crystal geometry of PS-b-PEO is well defined and the lamellar core is rather uniform in thickness, such system can be considered as a model to study the properties of PS brushes with variable grafting density. Moreover, the constraints imposed by the PS brush on the growing crystal can be studied from the point of view of their impact on the resulting semicrystalline morphology. In this chapter, the microstructure of single crystals of PS-b-PEO has been analyzed with a combination of AFM and SAXS/WAXS measurements. We search for the morphological parameter sensitive to the PS brush stretching regime.

IV.1. Introduction

In this chapter, we will focus on the semicrystalline morphology of PS-*b*-PEO single crystals. Although these systems have been extensively studied since about four decades, the micro-structural information on these systems is still scarce or even missing to our knowledge. It is noteworthy that the interest in these systems has been recently renewed in the perspective of using them as models of grafted amorphous brushes with variable grafting density. Indeed, during crystallization of PEO, the amorphous block, i.e. PS, is rejected from the crystal accumulating on its basal surfaces. Since the crystal thickness formed during isothermal crystallization is a sharply selected value[57], the grafting density of the resulting PS brush is also well defined. Therefore by varying the crystal thickness one can obtain the PS brushes with grafting density varying in a broad range.

In the scope of this work, we investigate the influence of the amorphous block on crystallization of semicrystalline-amorphous block copolymers. Therefore the first step in the study should consist in a careful analysis of the semicrystalline structure of single crystals of PS-*b*-PEO formed from copolymers with different lengths of the PEO block and at different crystallization temperatures. To this end, a

combination of reciprocal and direct-space techniques such as SAXS and AFM will be employed. While AFM experiments will be performed on isolated single crystals, the SAXS investigation will be carried out on mats of single crystals slowly sedimented from the "mother" solution. In this case, the model to be used for the data interpretation is the one-dimensional two-phase system for which the thickness of the amorphous (L_a) and crystalline (L_c) layers are conventionally determined following the correlation function (CF) and/or interface distribution function (IDF) approaches. The results of AFM and SAXS will be critically reviewed and quantitatively compared. The complementarities of these two techniques are expected to provide additional insights as to the crystal shape and distribution.

In the second step of the study, we will try to identify the morphological parameter of this semicrystalline system, which is sensitive to the stretching brush regime of PS and evaluate the corresponding state of the PS brush. We believe that this analysis will contribute to understanding of the polymer crystallization process at the molecular scale and the interplay between the crystallizable and amorphous parts of the system during this process.

IV.2. Morphology of single crystals of PS-b-PEO

In this section, several morphological features of the grown single crystals will be described. Some of the results presented here will be important for the later discussion on the micro-structural parameters and the state of the tethered PS chains on the lamellar surface.

IV.2.1 *Lateral habits of the PS-b-PEO single crystals*

It is noteworthy that not all sample preparations showed perfectly uniform square-shaped crystals as exemplified in Figure II.2. An account of the technical difficulties experienced during sample preparations was given in the experimental chapter. However, the morphological features of the PS-*b*-PEO crystals, which make them different from the ideal uniform platelet with a square shape, cannot be simply assigned to the experimental difficulties alone. Instead they can reveal some intrinsic structural features of these objects. Figure IV.1 shows two micrographs of single crystals, the shape of which significantly departs from that of a square platelet. Thus, in the left panel of figure IV.1, some strongly anisometric objects are observed, which are rather common for the single crystal preparations containing high MW of the

PEO block at high undercoolings. In the right panel of figure IV.1 one can observe a crystal exhibiting non-linear growth faces approaching a dendrite-type of shape.

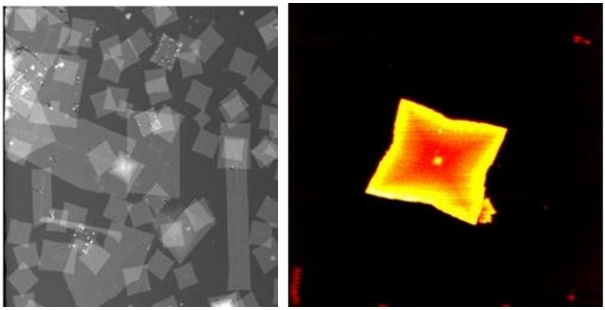

Figure IV.1. STEM image of PS-*b*-PEO (40-680) crystallized at 25°C with some ribbon-like structures (left) and a star-like single crystal of PS-*b*-PEO (190-240) crystallized at 25°C (right).

These morphologies were typically found for copolymers with a high PS/PEO ratio. We speculate that the curvature of the growth faces can be due to a significant fraction of swollen PS coils, which accumulates in front of the crystallization front creating a barrier for the transport of new crystallizable species. The dendritic features become even more prominent at higher crystallization temperatures (cf. Fig. IV.2), where the increased crystal thickness amplifies the steric hindrance imposed on the attaching chains by the strongly squeezed PS coils. Importantly, in this case, the fastest growth axes are not anymore the conventional 120 planes but rather 010 or 100 planes. A pronounced dendrite with a high frequency of

branching can be seen in figure IV.3 for the copolymer with an even higher PS content.

In some instances, nascent truncated shapes were also observed, where the nascent faces were parallel to one of the lattice parameter (i.e., **a*** or **b**). The latter are reminiscent of hexagonal single crystals of linear polyethylene extensively studied in the past[10,100].

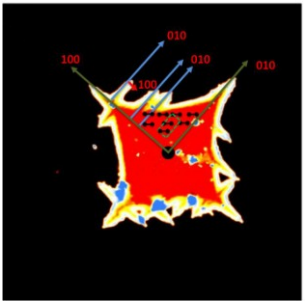

Figure IV.2. Single crystal of PS-*b*-PEO (190-240) grown at 30°C, the preferred growth axes are {010} & {100} axes. The direction of the folds is thus not exclusively parallel to the 120 plane.

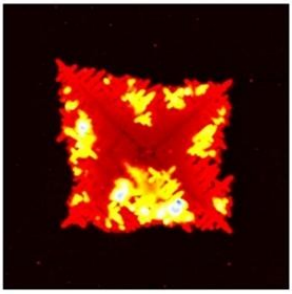

Figure IV.3. Single crystal of PS-*b*-PEO (250-350) formed at 30°C imaged after centrifugation and washing.

Among other structures observed upon crystallization of PS-*b*-PEO from dilute solutions are multilayered structures. They can be considered as intermediate step toward the formation of 3D structures starting from the isolated single crystalline lamella.

Three examples of such multilayer structures are shown for PS-*b*-PEO (40-445) crystallized at 32°C in figure IV.4. In this case, the facets of the overgrowing, or "daughter", crystals are parallel to that of the "mother" crystal. The "daughter" crystals thus form a multi-layer by stacking on top of each other while preserving the same direction of the crystallographic axes. The center of each crystalline layer can be either laterally offset versus that of the previous layer (cf. Fig. IV.4, left) or kept in the same place, leading to the formation of crystalline pyramids (cf. Fig. IV.4, middle and right).

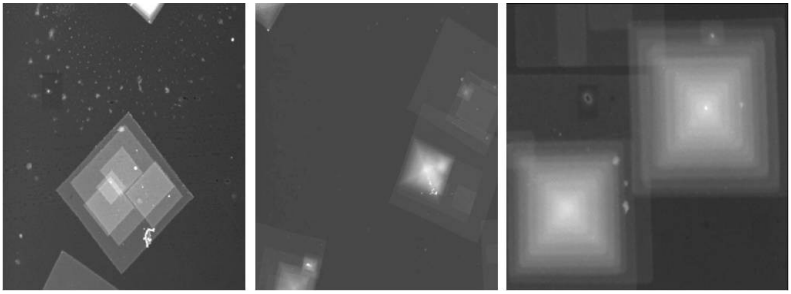

Figure IV.4. STEM images of pyramidal multilayered structures of PS-b-PEO (40-445) crystallized at Tc=32°C.

In some cases the multilayer structures are formed via the giant screw dislocation mechanism, which is particularly frequent in growth of homopolymer crystals[10]. Three other examples of multilayer structures imaged by AFM are presented in figure IV.5.

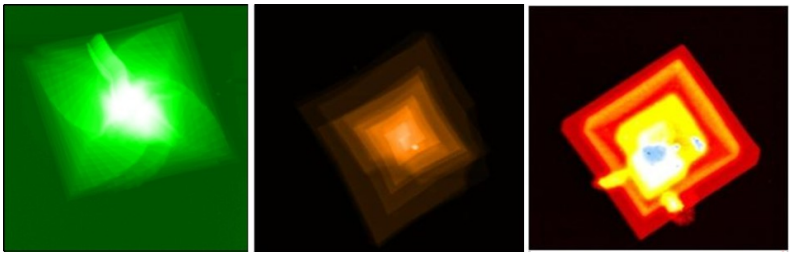

Figure IV.5. AFM height images of three different types of multilayer structures: multilayer formed via giant screw dislocation for PS-*b*-PEO (40-680) crystallized at T_c=25°C (left); multi-terrace structure of PS-*b*-PEO (40-220) crystallized at 25°C (middle) and multilayer structure of PS-*b*-PEO (95-270) formed at T_c=30°C (right).

As far as the morphology of the basal lamellar surface is concerned, the AFM images reveal some inhomogeneities of the surface topography, which consist in a fine surface texture composed of stripes running approximately perpendicular to the growth faces (cf. Fig. IV.6). Similar observations have been made on single crystals of linear PE[88]. The PE crystals showed a fine surface texture of the sectors composed of nanometer-scale surface corrugations. In single crystals of PE deposited on a substrate the orientation of these corrugations

was nearly orthogonal in adjacent crystal sectors, and rather close to that of the much coarser pleats aligned parallel to (530) or (310) planes. The authors supposed that

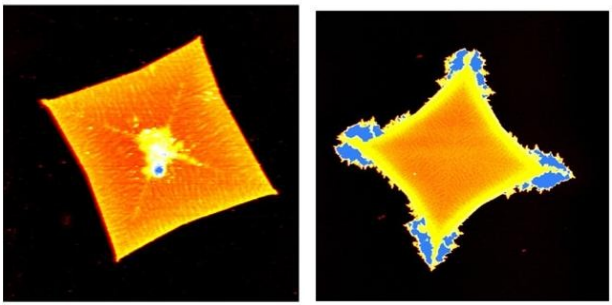

Figure IV.6. Single crystals of PS-*b*-PEO (70-270) and (190-240) formed at 30°C show the surface wrinkles running perpendicular to the {120} plane and four sector boundaries.

these surface features, or wrinkles, originate from crystal flattening on the substrate. For the crystals of PS-*b*-PEO, the problem of flattening on the substrate could not be of relevance as the crystals have already flat configuration in the "mother" solution. In addition, the direction of the wrinkles observed in the present work is different. Therefore, we speculate that these features can be either due to organization of the PS chains on the crystal surface or can be related to the growth mechanism *per se*, i.e. they can reflect the size of the secondary nuclei[101].

IV.2.2 *Lamellar thickness distribution*

When examined with more scrutiny, some crystals reveal regions of different thickness, which often look like a frame formed parallel to the growth faces. Figure IV.7 shows single crystals of PS-*b*-PEO (40-150) generated at 25°C. From the AFM image it is clearly visible that the overall thickness is not constant across the whole crystal. Instead, three regions of different thickness are clearly distinguishable and are highlighted in the figure with different colors such as blue for the crystal interior, red for the outer zone and green for the crystal edges zone. The cross-section profiles traced along the 120 direction are shown using the same color code. The histogram of this crystal was shown previously (cf. Fig. III.2), it reveals a trimodal distribution of the lamellar thickness.

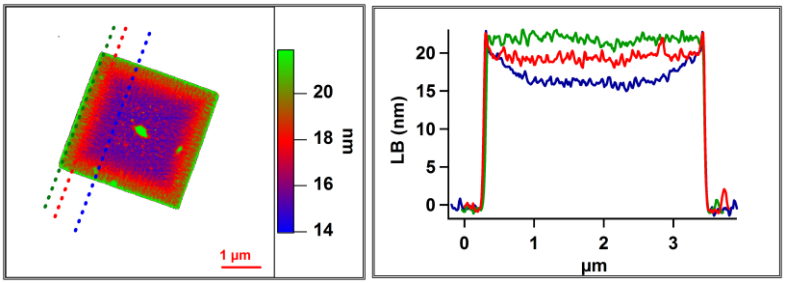

Figure IV.7. Single crystal of PS-*b*-PEO (40-150) generated at 25°C (left) and corresponding cross-sectional profiles (right).

Thus by fitting the histogram to a sum of Gaussian functions, the maxima were found at 15.85 nm, 18.87 nm and 21.94 nm. Interestingly, the difference in thickness of successive zones is very close to 3 nm, i.e., it is on the order of 1.5 times c-parameter of the PEO crystal. The exact reasons for this particular value are not understood yet but it may be related to quantization of the PEO crystal thickness. Figure IV.8 provides another example of single crystals with non-uniform thickness distribution. These are crystals of PS-*b*-PEO (70-270) formed at 30 and 25°C. As for the previous situation, the thicker parts of the crystals are the crystal edges. The height histograms shown in the figure give also an impression of quantized lamellar thickness, although the thickness step is now somewhat smaller than it was previously. One of the reasons for this difference in the height step can be related to the contribution coming from the amorphous PS block, which can modify the overall step value.

Observations of similar lens-shaped crystals were previously reported for PS-*b*-PEO by *Cheng* and co-authors[102], however without specifying the reasons for such a thickness variation across the crystal. It is noteworthy that in our work the lens-shaped crystals are mainly observed for the diblocks

with low MW of PEO, which are formed close to the T_d temperature in solution. This can explain why even a small polydispersity can result in a visible variation of lamellar thickness. With regard to this issue, it can be recalled that the crystal thickness variation becomes steeper in the proximity of

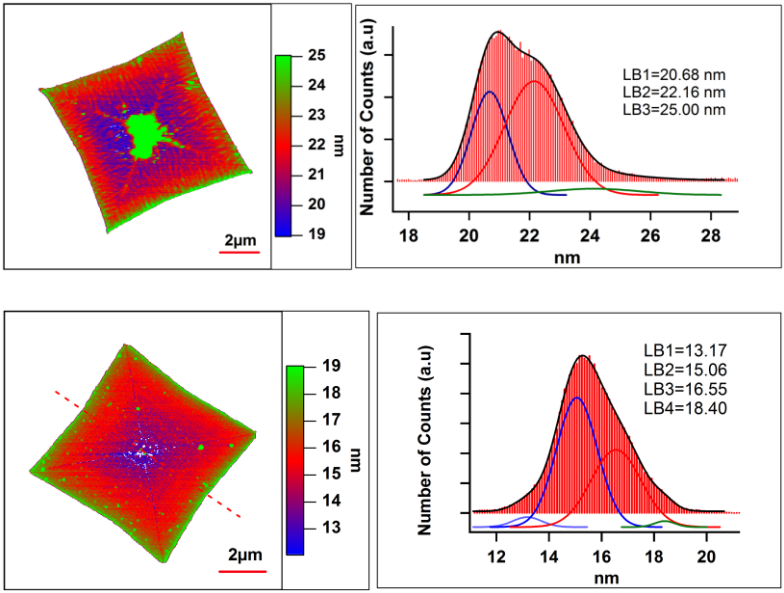

Figure IV.8. Single crystals of PS-*b*-PEO (70-270) formed at 30°C (top left) 25°C (bottom left). The right panels give the corresponding height histograms and fits with Gaussian functions.

the final melting point (cf. Section I.1.5). Therefore in these conditions the chain fractionation accompanying crystallization can bring about a variation of crystal thickness, which is not negligible. The crystal thickness distribution will

be discussed further in the text when comparing the results of AFM and SAXS.

IV.2.3 *Chain orientation in the PS-b-PEO single crystals as measured by WAXS*

Although the chain orientation in single crystals of PS-*b*-PEO has been already addressed in the experimental section, and the evidence was obtained from selected-area ED that the PEO chains are normal to the basal lamella plane, it is quite convenient to check the chain orientation in real time using 2D WAXS in transmission. Figure IV.9 shows WAXS patterns corresponding to the single

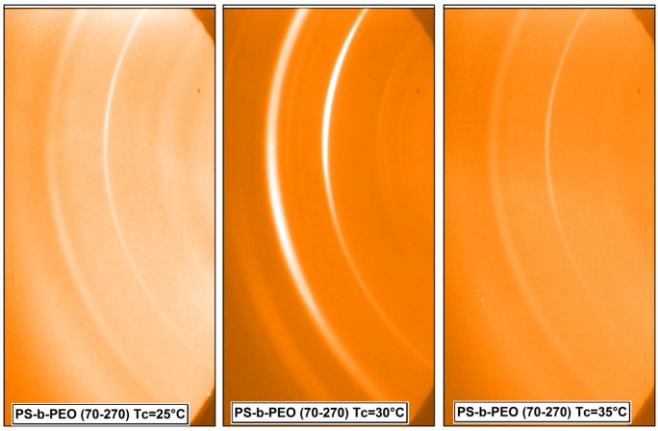

Figure IV.9. WAXS patterns measured on mats of PS-*b*-PEO (70-270) single crystals using an inclined CCD camera. The plane of the sample is roughly horizontal.

crystal preparation of PS-*b*-PEO (70-270) diblock copolymer crystallized at different temperatures. It can be seen that the WAXS patterns are oriented and that the maximum of the first intense peak (i.e. 120) is lying in the equatorial plane. Given the monoclinic lattice of PEO with the angle beta differing from 90 degrees, this means that, on the average, the PEO chains are vertical. Controlling the chain orientation will be very important in further studies involving single crystal annealing because it can shed light on the chain refolding mechanisms.

IV.2.4 *Microstructure of single crystals of PS-b-PEO investigated with SAXS*

The main information on the micro-structural parameters of single crystals of PS-*b*-PEO was obtained from SAXS measurements on sedimented single crystal mats. For this particular purpose, the advantages of SAXS with respect to AFM are mainly due to the fact that, within the global lamellar thickness, the SAXS technique can discriminate the thickness of the constitutive crystalline lamella core (L_c) and amorphous layer thickness (L_a). Moreover, the SAXS signal contains information over billions of single crystals, which is unmatched in terms of the object statistics.

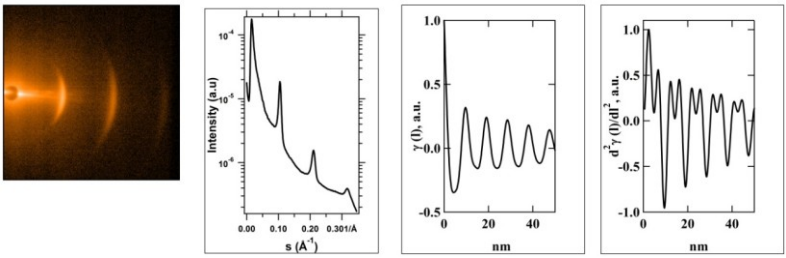

Figure IV.10. Oriented 2D SAXS pattern of a single crystal mat of PS-*b*-PEO (40-680) crystallized at 30°C (left). Right: the corresponding 1D scattering curve, 1D correlation function and interface distribution function.

A typical measurement performed on a single crystal mat of PS-*b*-PEO diblock formed at 30°C is given in figure IV.10. On 2D SAXS pattern, one can see that the scattering intensity is concentrated in the equatorial plane and exhibits at least three orders of the main interference maximum, which indicates good ordering within the single crystal stacks. It is clear that in the ideal case of stacked parallel platelets, the pattern should contain only a series of equatorial spots. The angular spread of the peaks around the equator is due to the varying orientation of the lamellae stacks normal.

A streak visible in the equatorial plane of the pattern most probably originates from pores or cavities appeared during the crystal sedimentation and subsequent solvent drying. These defects located in-between the crystals generate a strong signal

due to a high electron density contrast. The reduced 1D SAXS intensity and 1D correlation and interface distribution functions are also shown in the figure. It can be noticed that the main interference maximum is centered on approximately 10nm, which corresponds to the long period of the system. The 1D correlation function reveals many interference maxima slowly decaying in amplitude. The minima of the CF exhibit flat bottom parts that testify the existence of well defined characteristic distances. Indeed, the interface distribution function allows to clearly separate the first two positive peaks that are conventionally assigned to the crystalline core and amorphous interlayer. Thus, in this case one can determine the most probable values of Lc and La simply by picking the maxima of the corresponding peaks. The first negative peak is assigned to the most probable value of long period.

The SAXS patterns obtained on different PS-*b*-PEO copolymers are exemplified in figure IV.11. The patterns display a progressive decrease of long period (or position of the main interference maximum) when the MW of the PEO block is increased. This trend is also reflected in positions of the first subsidiary maximum of the correlation functions or the first minimum of the interface distribution functions.

Importantly, the interface distribution functions show better resolution of the first two positive peaks when the MW of PEO is increased. The insufficient resolution of the interface distribution functions for the diblock copolymers with low MW of PEO can be accounted for by the lens-shaped single crystals described previously. Indeed, the broad lamellar thickness distribution in this case smears out the crystalline and amorphous layer distributions making them merging. A detailed comparison between the AFM and SAXS results will be given in the next section.

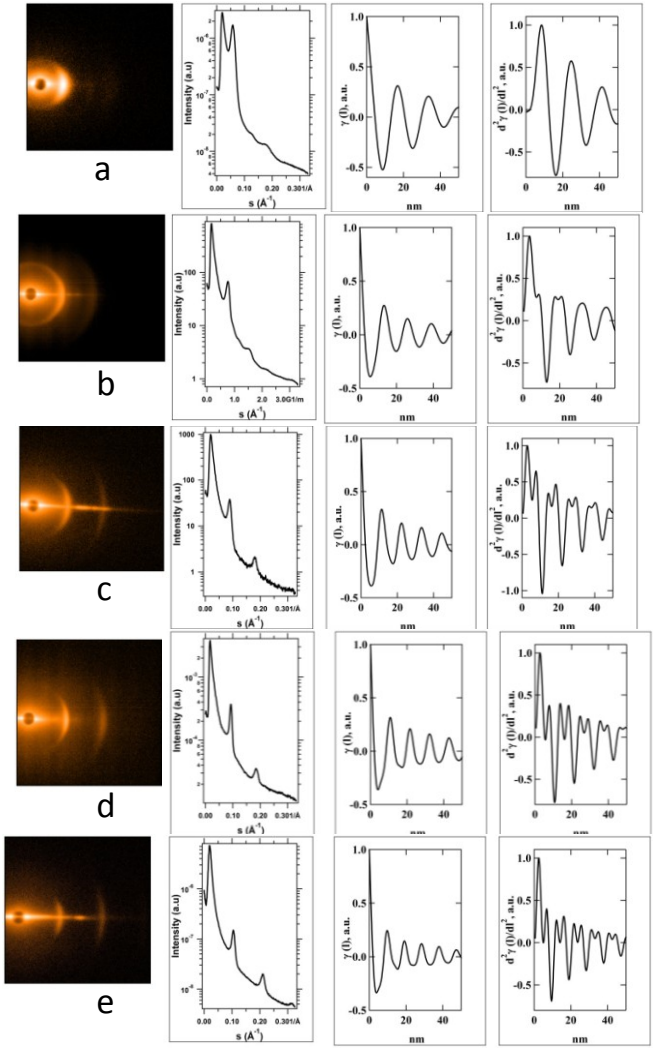

Figure IV.11. SAXS measurements corresponding to single crystal mats of PS-*b*-PEO (40-150) crystallized at T_c of 25°C (a) and PS-*b*-PEO (40-250) (b), PS-*b*-PEO (40-380) (c), PS-*b*-PEO (40-445) (d), PS-*b*-PEO (40-680) (e) crystallized at 30°C. The corresponding 1D scattering curves, 1D correlation and interface distribution functions are shown on the right.

It is instructive to follow the micro-structural evolution on the same PS-*b*-PEO block copolymer crystallized at different temperatures, as illustrated in figure IV.12. It can be clearly seen that the long period increases with Tc, which is the expected behavior. Moreover, at the same time the interface distribution functions display better and better resolution of the crystal and amorphous layer distributions.

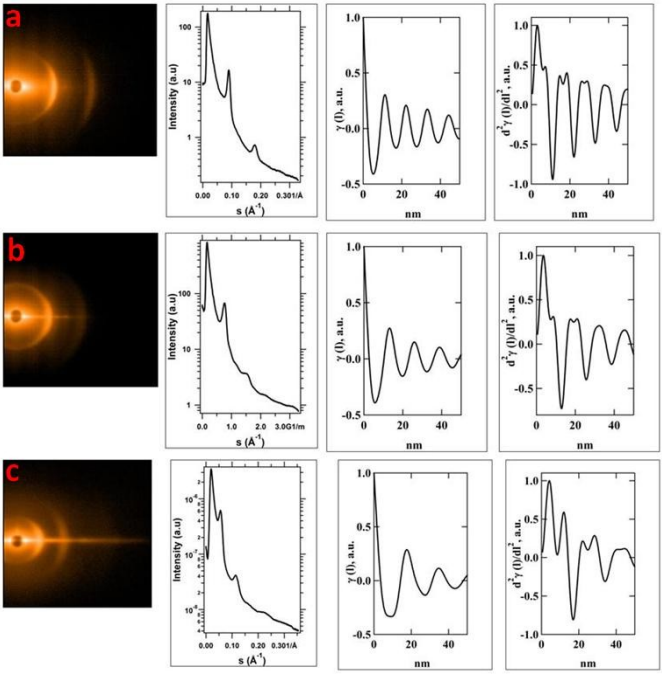

Figure IV.12 2D SAXS patterns, 1D scattering curves and the corresponding correlation and interface distribution functions of PS-*b*-PEO (40-250) single crystal mats formed at 25°(a), 30°(b) and 35°C (c).

At this point it is appropriate to summarize all the SAXS results obtained on the PS-*b*-PEO crystals by displaying the values of L_c, L_a and LB as a function of T_c. Figure IV.13 presents our findings for the series of PS-*b*-PEO block copolymers containing PS blocks of 40 monomers. We show here the SAXS distances found by following both, the correlation and interface distribution function approaches. These two sets of data are denoted with _CF and _IDF, accordingly. The difference between the results obtained with the two approaches is essential mainly for the low MW PEO for which the distances are characterized by broad distributions.

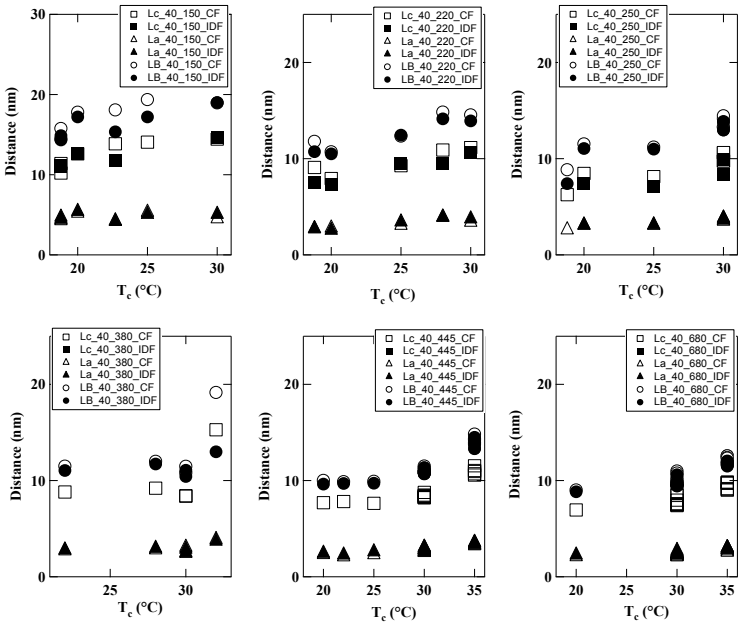

Figure IV.13. SAXS distances L_c, L_a and LB for the series of PS-*b*-PSO block copolymers with the degree of polymerization of the PS block equal 40.

It is important to note that in the attribution of the two SAXS distances we decided to assign the smallest distance to the amorphous interlayer throughout this work. This distance attribution will be discussed in some detail in the following sections. Based on this attribution, it can be seen from figure IV.12 that, in agreement with the data given in figure IV.11, at a constant crystallization temperature the crystal thickness increases when the MW of PEO gets smaller. This reflects the fact that the degree of supercooling of crystals with low MW PEO is smaller. Also, for all the samples the crystal thickness

increases with T_c, which is in line with the general expectations and the results reported in figure IV.12.

Another series of samples presented in figure IV.14 contains PS blocks of variable length, while the length of the PEO block is kept approximately constant. In this case, the increase in the PS length mainly gives rise to the increase of long period.

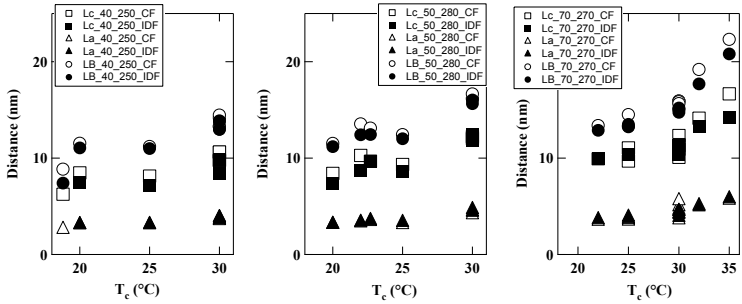

Figure IV.14. SAXS distances L_c, L_a and LB for the series of PS-b-PSO block copolymers with varying degree of polymerization of the PS block and approximately equivalent PEO blocks (i.e. N= 250, 280 and 270).

IV.2.5 *Comparison of the micro-structural parameters obtained from AFM and SAXS*

In this section, we will quantitatively confront the SAXS and AFM data to check their accuracy. It is convenient to start the comparison with the single crystals that are most close to the

shape of the ideal uniform platelet. This is the case of single crystals from PS-*b*-PEO (40-680) copolymer (cf. Fig. IV.15).

The above figure shows an AFM micrograph of a typical crystal together with cross-sections passing through the crystal center and edges. The red and blue cross-section lines show a relatively small difference in the lamellar thickness, which means that the lens-shape feature was visibly not developed here. Therefore the crystal is characterized by a rather uniform thickness. The SAXS intensity acquired on a single crystal mat reveals good orientation and the presence of three orders of the main interference peak. The corresponding correlation and interference distribution functions allow to determine the lamellar stacking periodicity and discriminate the amorphous and crystalline layers. The crucial step in the comparison between the SAXS and AFM data is displayed in the bottom right panel of figure IV.15 where the SAXS interface distribution function is overlaid with the inverted height histogram calculated from the AFM image.

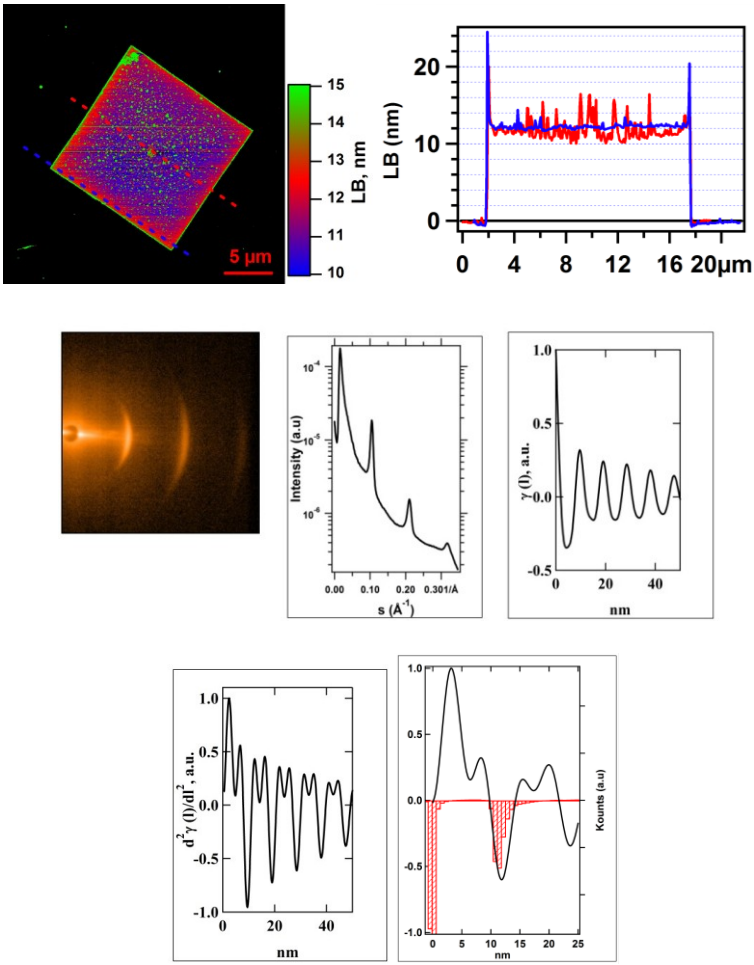

Figure IV.15. Comparison of SAXS and AFM data for the PS-*b*-PEO (40-680) single crystals formed at 35°C. *Top*: AFM image of a typical single crystal with two cross-sections traced through the center and edges of the crystal. *Middle*: 2D SAXS pattern, reduced scattering curve and 1D correlation function. *Bottom*: SAXS interface distribution function alone and with the AFM height histogram (red bars) overlaid.

It is evident that the height, as measured with AFM corresponds to the lamellar thickness including the crystalline lamellar core and amorphous top layer. Therefore, the AFM height should be comparable to the SAXS long period, as was found previously for single crystals of linear PE[103]. In our case, the agreement between SAXS and AFM is quite satisfactory, and this is despite the fact that these two techniques are very different from all points of view, including the spatial calibration procedures.

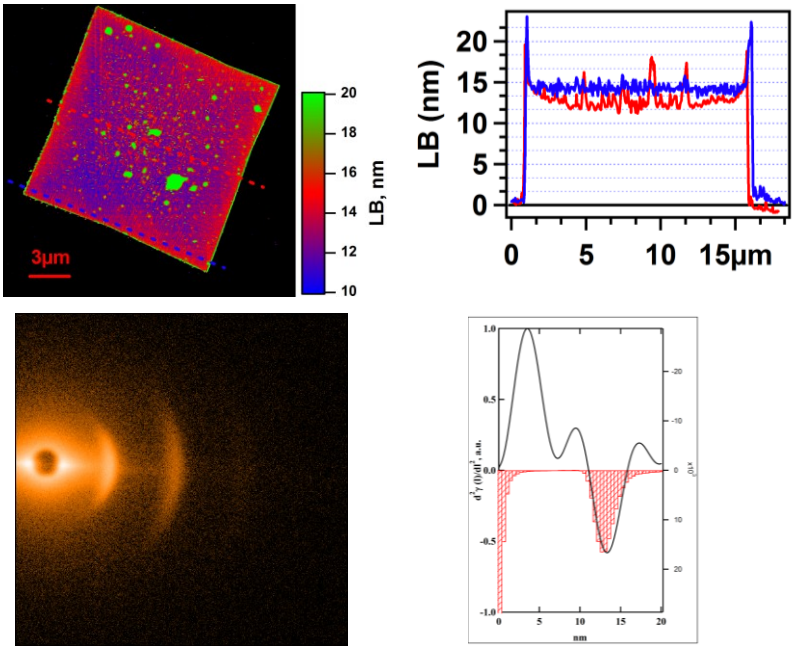

Figure IV.16. Comparison of the SAXS and AFM data for the PS-*b*-PEO (40-445) single crystals formed at 35°C. The legend is similar to figure IV.15.

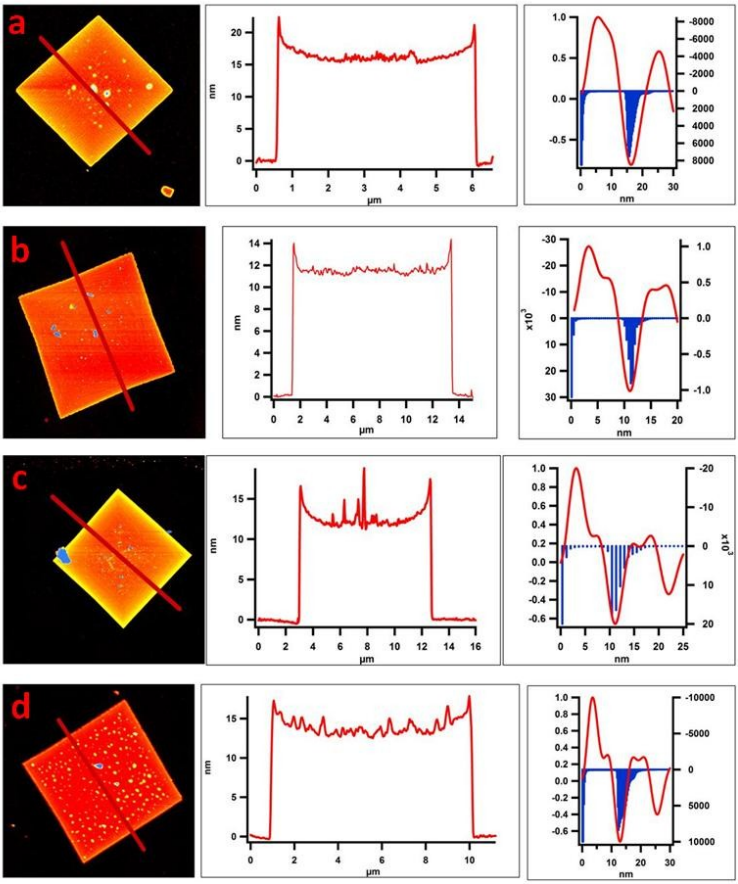

Figure IV.17. Comparison of the SAXS and AFM data for the PS-*b*-PEO copolymers with low MW of PEO. (a) PS-*b*-PEO (40-150) formed at Tc=25°C; (b) PS-*b*-PEO (40-250) formed at Tc=25°C, (c) PS-*b*-PEO (40-250) formed at Tc=30°C and (d) PS-*b*-PEO (40-250) formed at Tc=25°C. The legend is similar to figure IV.15.

The same comparison was attempted for the PS-*b*-PEO (40-445) crystals (cf. Fig. IV.16), and it also reveals very good

agreement. The results of this comparison are already rather encouraging for the quantitative treatment of AFM images in order to extract meaningful morphological parameters.

In figure IV.17, we follow the same type of comparative analysis for single crystals containing low MW PEO, which typically results in the formation of lens-shaped crystals. Indeed, the lens-shapes can be seen for the crystals of PS-*b*-PEO (40-150) and PS-*b*-PEO (40-250) shown in the figure. Thus for the PS-*b*-PEO (40-150) block copolymer the height difference between the crystal center and periphery reaches almost 5nm, or 25% of the overall height. It is thus evident that in the SAXS interface distribution function, we are no more capable of discriminating the amorphous and crystalline layer thickness. Despite this uncertainty, the SAXS and AFM data still agrees very well for the overall lamellar thickness distribution. However, in some instances the distance distribution, as found from SAXS, is somewhat broader than that of AFM, which can be accounted for by the different object statistics probed by these two techniques.

The last point of comparison between SAXS and AFM will performed on PS-*b*-PEO copolymers with longer PS blocks.

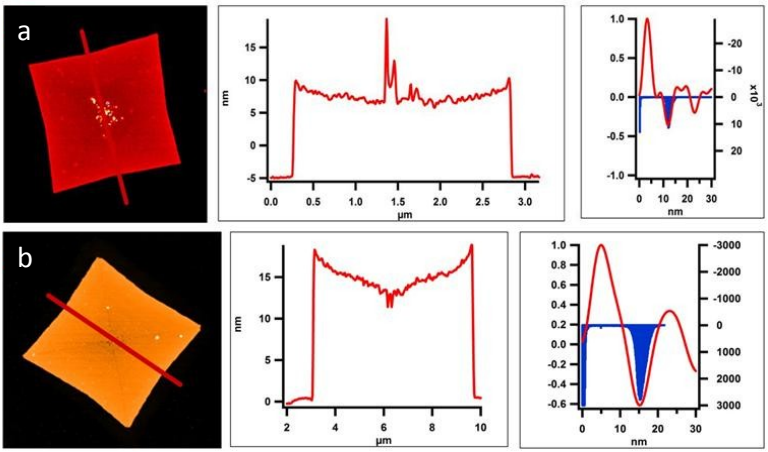

Figure IV.18. Comparison of the SAXS and AFM data for the PS-*b*-PEO copolymers with variable length of the PS block. PS-*b*-PEO (50-280) formed at Tc=25°C (a) and PS-*b*-PEO (70-270) formed at T_c=30°C (b). The legend is similar to figure IV.15.

In this case, the lens-shape feature is even more enhanced, especially for sample PS-*b*-PEO (70-270). Despite this morphology, the lamellar thickness distribution is still in agreement with AFM. We can thus conclude that quantitative analysis of the AFM images of single copolymer crystals can be successfully used to extract the micro-structural parameters such as the long period.

IV.2.6 *Assignment of the SAXS distances L_c and L_a*

Generally, it is well documented that PEO forms thick crystals[10] and that the situation with the SAXS distance assignment here is thus very different from that encountered

for example for aromatic semirigid chain polymers such as poly(ether ether ketone), poly(ethylene terephthalate) or poly(trimethylene terephthalate). Therefore the ambiguity due to the Babinet principle is less dramatic in this case. However, we decided to verify the distance attribution, i.e. the assignment of the largest distance to Lc and the smallest one to La, by investigating the same crystal preparation in the native "mother" solution and in the dry state. To obtain a reasonable signal-to-noise ratio we had to employ higher concentrations of the copolymer for solution crystallization. Therefore the first step in this analysis was to check whether by using these high concentrations we are still capable of generating conventional lamellar crystals. Figure IV.19 (top left) shows indeed that the same lamellar habit was preserved for the crystals of PS-*b*-PEO (40-250) grown from a higher concentration "mother" solution. The 2D pattern of a crystal suspension reveals a clearly distinguishable interference maximum, which indicates that the crystals in suspension are ordered. We believe that the steric repulsion of the swollen PS brush grafted to the crystal surface results in the appearance of some average nearest-neighbor distance between the lamellae, which is reflected as interference in the SAXS curve. Anticipating our later discussion on the state of the PS chains,

it is useful to mention that the interdigitaion of the PS segments

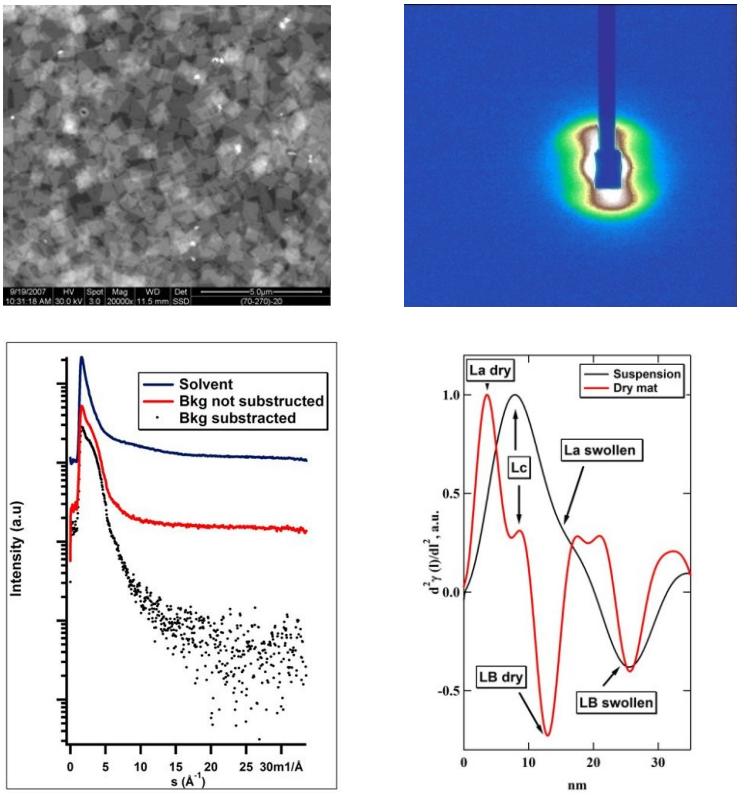

Figure IV.19. (Top left): single crystals of PS-*b*-PEO (40-250) grown in amyl acetate solution with increased concentration at 30°C; (Top right): 2D SAXS pattern corresponding to the single crystal suspension; (Bottom left): reduced 1D SAXS intensity; (Bottom right): interface distribution functions corresponding to the single crystals in suspension and in the dry state.

from the neighboring lamellae is hardly possible for this particular system. Therefore the inter-crystalline distance

should correspond to the double thickness of the PS brush (cf. Fig. IV.20). In addition, the SAXS intensity reveals the crystal orientation in suspension. The latter is of course of little surprise as the crystals are slowly sedimenting and act as small parachutes which are oriented perpendicular to the direction of sedimentation.

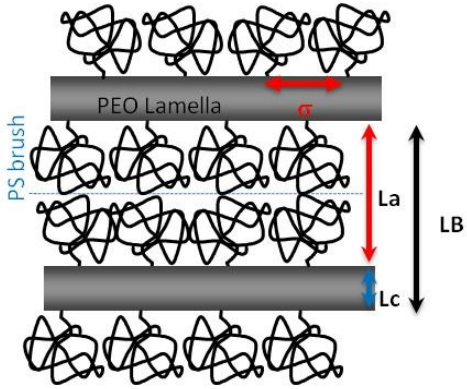

Figure IV.20. Schematics of PS-*b*-PEO single crystals in suspension with strongly swollen PS coils. The sketch does not show the PEO folds.

The interface distribution function was computed after the necessary correction of the scattering intensity for scattering of the pure solvent (cf. Fig. IV.19, bottom panels). Close to the origin, the function shows the main maximum and a shoulder that can be attributed to the two SAXS distances. By comparing the interface distribution functions corresponding to the same crystals of the diblock copolymer in suspension and in the dry state, one can see that one of the distances was

not changed, which is obviously the lamellar crystal thickness. Therefore the proposed distance attribution is confirmed. It is noteworthy that in the swollen state the long period of the system is doubled, while the thickness of the amorphous layer is increased almost by a factor of four with respect to the dry state. This observation seems quite logical because amyl acetate is a good solvent for PS.

The next issue to be tackled in this chapter concerns the state of the PS blocks tethered to the crystal surface. To study the state of PS, we have to carry out a more careful analysis of the SAXS distances to be able to discriminate the contributions of the PS blocks and PEO folds present on the lamellar surface.

IV.3. Conformation of tethered PS brush during crystallization of PS-b-PEO from solution

In the frame of this work, we are interested in determining the impact of the amorphous block on the diblock copolymer crystallization process in dilute solution. It is therefore necessary to figure out what is the key parameter or parameters responsible for this effect. One of the first ideas one can have in mind is to start with estimation of the entropic contribution of the stretched PS brush. This contribution can increase the overall free energy of the lamellar surface and thereby modify the thermodynamics of the crystal formation. From the theoretical point of view, the scaling properties of polymer chains anchored onto planar surfaces were initially elaborated by *de Gennes* and *Alexander.*[104-106] Afterwards, *Semenov*[107], *Milner-Witten-Cates*[108] and *Zhulina-Priamitsyn-Borisov*[109,110] developed a self-consistent-field theory (SCF), which predicted a parabolic form for the density profile and obtained an expression for the free energy of two interacting flat brushes. As far as the crystallizable-amorphous diblock copolymers are concerned the theoretical approaches were developed approximately at the same time[111,112]. In the latter works, the scaling relations between the crystal thickness

and molecular weight of the amorphous block were established by minimizing the total free energy with respect to the area per chain.

IV.3.1 *Evaluating the weight of the amorphous fold and the number of folds in PS-b-PEO crystals*

To better understand the crystal formation conditions, it is thus of interest to evaluate the stretching regime of the PS brush for the single crystal preparations used in this work.

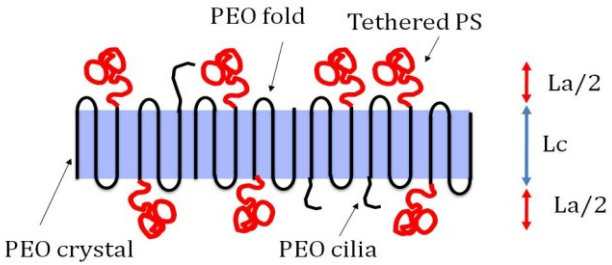

Figure IV.21. Schematics of a single crystal of PS-*b*-PEO structure showing the different structural elements of the system.

For this purpose, we will need to determine the number of folds of the crystallizable block and to compute the surface available for one grafted PS block.

Figure IV.21 presents a schematics of the PS-*b*-PEO crystalline lamella in which different structural elements are

depicted. In the simplest approximation, we can neglect the influence of the chain ends (cilia) and consider that all the chain ends are incorporated in, or tightly bound next to, the crystal surface. Therefore the total mass of the PEO chain can be written as:

$$M_{PEO} = n_{stem} L_c \rho_{PEO}^c A_0 + n_{fold} M_{fold} \qquad \text{IV.1}$$

where the M_{fold} stands for the mass of the amorphous chain fold of PEO. The number of stems n_{stem} is related to n_{fold} as:

$$n_{stem} = n_{fold} + 1 \qquad \text{IV.2.}$$

If one recalls that the PEO lattice accommodates four chains, the surface A_0 occupied on the lamellar basal plane by one stem is given by:

$$A_0 = ab \sin\beta \,/4 \qquad \text{IV.3.}$$

The thickness of the interlamellar amorphous region can be expressed as:

$$L_a = \frac{V}{S} = \frac{(n_{stem} - 1)\frac{M_{fold}}{\rho_{PEO}^a} + \frac{M_{PS}}{\rho_{PS}}}{S} \qquad \text{IV.4.}$$

In Eq. (IV.4), S stands for the half of the surface on the basal lamellar plane occupied by one PEO chain:

$$S = n_{stem}\, A_0 \qquad \text{IV.5.}$$

On the other hand:

$$M_{PEO} = (n_{stem} - 1)M_{fold} + n_{stem}\, L_c \rho^c_{PEO} A_0 \qquad \text{IV.6.}$$

Therefore:

$$n_{stem} = \frac{M_{PEO} + M_{fold}}{M_{fold} + L_c \rho^c_{PEO} A_0} \qquad \text{IV.7.}$$

or

$$n_{fold} = \frac{M_{PEO} - L_c \rho^c_{PEO} A_0}{M_{fold} + L_c \rho^c_{PEO} A_0} \qquad \text{IV.8.}$$

By inserting Eq. (IV.7) into Eq. (IV.4), one obtains the expression for the mass of the amorphous fold:

$$M_{fold} = \frac{\frac{M_{PS}}{\rho_{PS}} L_c \rho^c_{PEO} A_0 - A_0 L_a M_{PEO}}{A_0 L_a - \frac{M_{PEO}}{\rho^a_{PEO}} + \frac{L_c \rho^c_{PEO} A_0}{\rho^a_{PEO}} - \frac{M_{PS}}{\rho_{PS}}} \qquad \text{IV.9.}$$

In the calculations, apart from the known lattice parameters of PEO, we used the following tabulated constants:

- $\rho^c_{PEO} = 1{,}239\ g/cm^3$
- $\rho^a_{PEO} = 1{,}124\ g/cm^3$
- $\rho_{PS} = 1{,}052\ g/cm^3$.

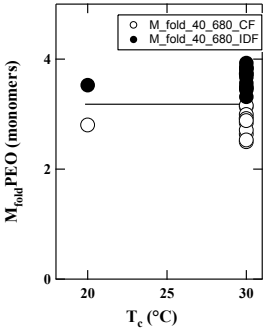

Figure IV.22. Molecular weight of the amorphous PEO fold for single crystals of PS-*b*-PEO (40-680) expressed in number of monomers. The calculations are performed using the correlation function (_CF) and interface distribution function (_IDF) data.

Figure IV.22 shows the amorphous fold mass expressed in number of PEO monomers calculated for single crystals of PS-*b*-PEO (40-680) block copolymer. The computations have been performed using the SAXS distances determined following the correlation and interface distribution function approaches.

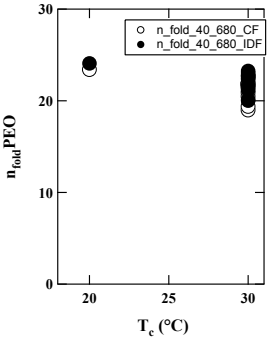

Figure IV.23. Number of folds in the PEO block of PS-*b*-PEO (40-680) single crystal.

Also, by knowing the fold mass, one can compute the crystallinity with respect to the crystallizable block only, i.e. PEO (cf. Fig. IV.24) as follows:

$$\chi_{PEO} = \frac{A_0 L_c \rho_{PEO}^c (n_{fold} + 1)}{A_0 L_c \rho_{PEO}^c (n_{fold} + 1) + M_{fold} n_{fold}} \qquad \text{IV.10.}$$

It can be seen that since the PEO folds are very tight, even for the thinnest crystals of PS-*b*-PEO (40-680) we obtain the weight crystallinity values which are very high, i.e. on the order of 90%.

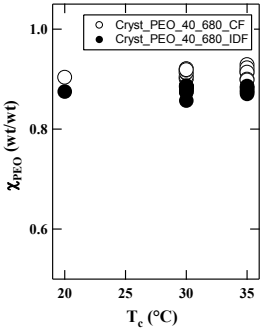

Figure IV.24. Weight crystallinity for the PEO block in single crystals of PS-*b*-PEO (40-680).

We tried to perform similar computations for single crystals of other block copolymers but they were not successful. One of the reasons is that the weight of the amorphous PEO fold is obtained as a small difference of two large values (cf. Eq. IV.9), and that's why the accuracy of this determination critically depends of the relative amount of the amorphous folds in the inter-lamellar layer. This can be illustrated by computing the ratio of PEO and PS in the interlamellar amorphous regions by assuming the same weight of the PEO amorphous fold for all the samples studied. The results are given in figure IV.25. Indeed, it can be seen that for single crystals of PS-*b*-PEO (40-680) copolymer the PEO-PS ratio is the highest and is close to one. We can see that the choice of our samples allow to cover a very broad range of compositions of the interlamellar amorphous regions. When

the MW of the PEO block decreases, the ratio becomes sensitively smaller, and decreases to about 0.09 for single crystals of PS-*b*-PEO (40-150) copolymer. Therefore the amorphous layer of the low MW PEO diblocks contains almost pure PS.

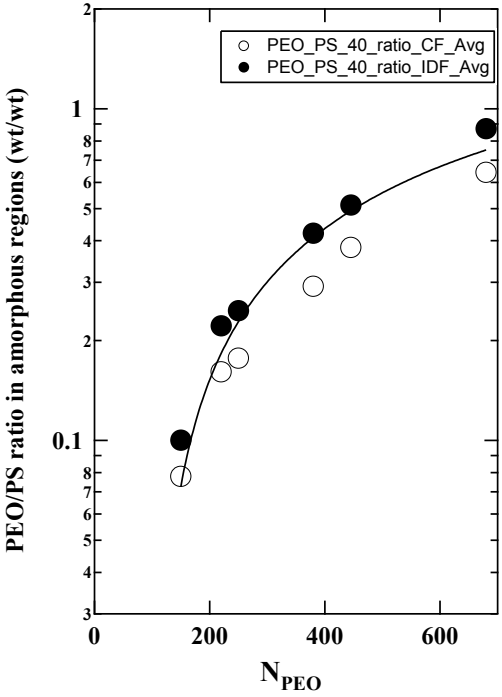

Figure IV.25. Weight ratio of PEO and PS within the interlamellar amorphous regions. The line is a guide to the eye.

It is instructive to calculate the number of folds for all the samples, by setting the PEO fold mass equal to that found for

the PS-*b*-PEO (40-680) crystals. The results of the computations are shown in figure IV.26. In this case, we plot only the average values of n_{fold} for each of the diblock copolymers thereby disregarding its dependence on the crystallization temperature, which is much weaker.

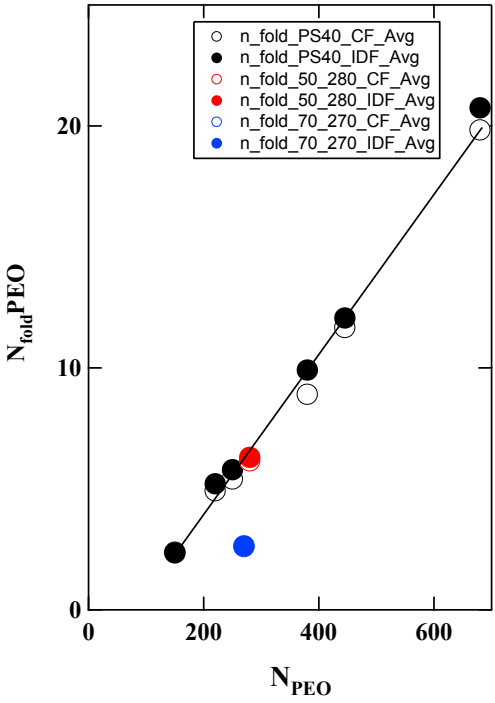

Figure IV.26. Average weight of the amorphous PEO fold expressed in number of monomers. The data comprise PS-*b*-PEO block copolymers with the lengths of the PS block equal 40 (black), 50 (red) and 70 (blue) monomers.

The general trend of n_{fold} is as expected, i.e. the crystals formed from the low MW PEO block exhibit less folds than those containing high MW PEO. Thus on the average the chains of the PS-*b*-PEO (40-150) crystals are folded twice, whereas, as it was already mentioned above, in the crystals of PS-*b*-PEO (40-680) the PEO chain has about twenty folds. Therefore it is clear that spatial confinement for the PS coil varies dramatically with the MW of the PEO diblock. However, in this graph we are not able to observe any particular transition related to a change of the PS brush stretching regime. It is noteworthy that the only point falling out of the general dependence corresponds to single crystals of PS-*b*-PEO (70-270). This sample exhibits much thicker crystals than its companions with the same length of PEO and smaller PS segments. The reason for this particular behavior is not yet fully understood.

IV.3.2 *Analysis of the crystallization line*

It is convenient to analyze the structure of single crystals from the crystallization line of the Gibbs-Thomson equation (cf. Fig. I.16). Here we swapped the axes of the graph to facilitate the comparison with literature data.

Figure IV.27 shows the crystallization line for all the block copolymer samples having the length of the PS block equal 40. It be seen that, despite some scatter in the data, all the slopes of the linear fits are negative, which means that the crystal thickness decreases with crystallization temperature. Also, across the sample series the crystal thickness increases together with decrease of the MW PEO. Apart from these observations, which were already made previously for the set of raw data, the curves do not add much new information. However, if we look in the literature, we can find that exactly these dependences were used to identify the setting of the highly-stretched brush regime for the PS block. The data due to *Cheng*, et al.[102] are given in figure IV.28

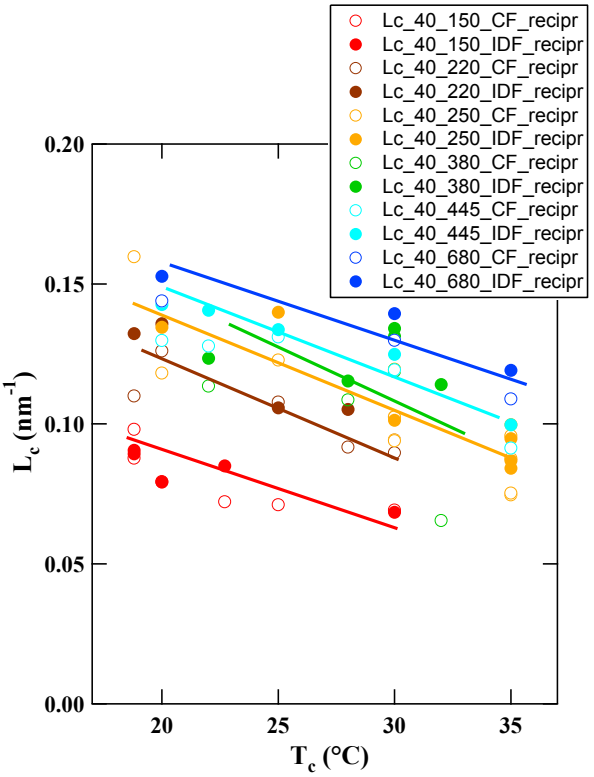

Figure IV.27. Dependence of the reciprocal crystal thickness on the crystallization temperature for all the block copolymers with the PS block length equal 40.

.

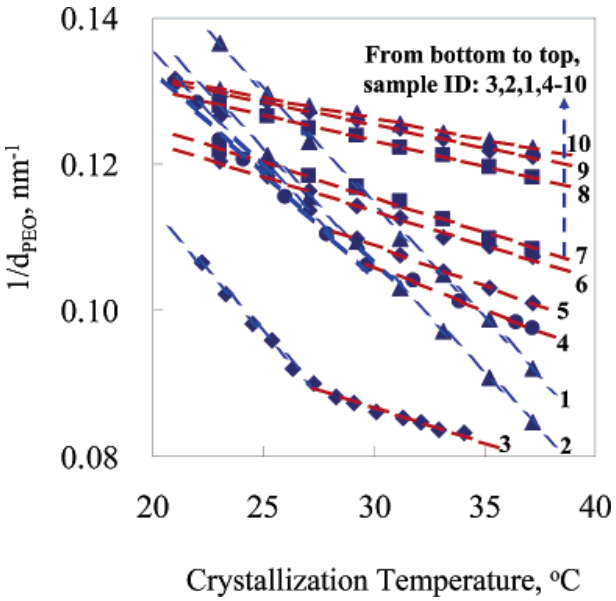

Figure IV.28. Literature data[102]: Relationships between 1/*d*PEO and *T*x for 10 PEO-*b*-PS diblock copolymer (and PEO homopolymer) samples crystallized at different *T*x values in both chlorobenzene/octane (for sample 3 in Table1 only) and amyl acetate (for samples 2-10). From bottom to the top samples 1-10 are (3) PEO-*b*-PS (11.0K-4.6K), (2) PEO-*b*-PS (17.0K- 3.0K), (1) PEO homopolymer, (4) PEO-*b*-PS (40.1K-7.7K), (5) PEO*b*- PS (23.0K-5.0K), (6) PEO-*b*-PS (16.7K-5.0K), (7) PEO-*b*-PS (20.3K-6.8K), (8) PEO-*b*-PS (9.4K-6.7K), (9) PEO-*b*-PS (8.7K- 9.2K), and (10) PEO-*b*-PS (17.0K-11.0K).

In the figure, one can clearly see two different slopes of the linear fits, which is essential for the authors' interpretation of the different stretching regimes of the PS brush. The authors claim that the highly stretching regime is observed in this case for samples starting from N3, which has a break in the slope of the crystallization line. Interestingly, this sample composition is equivalent to (44-250), and is thus very close to

our PS-*b*-PEO (40-250). The curves given in figure IV.28 reveal only a negligible scatter around the linear fits, which would certainly require at least 1.0 Angstrom resolution in determination of crystal thickness. Let us analyze what was the experimental technique allowing to achieve such resolution.

The authors were using two independent methods, both based on AFM height measurements. The first method consisted in completion of solution crystallization of a PS-*b*-PEO copolymer with a pure PEO homopolymer nucleated directly on the copolymer crystal. In this case, it was claimed that the height of the homopolymer crystal exactly matches the crystal thickness of the diblock copolymer lamella. It is however known that during solution crystallization even of a pure homopolymer, its crystal thickness can change in response for example to a change of crystallization temperature. An example of such crystal of linear PE shown in figure IV.29 was previously reported by *Ivanov*[100]. The crystallization of PE was conducted alternatively at two different temperatures, giving rise to what was called the "isochronously-decorated" single crystal. Importantly, it can be seen that, during crystallization, the thinner crystal formed at a lower crystallization temperature was successfully nucleated on a thicker crystal grown at a higher temperature. Moreover, the

opposite situation was also possible. So it can be concluded that the different parts of the crystal formed in different conditions of supercooling do not have the same crystal thickness. Therefore it will be difficult to admit that the crystal of a pure PEO homopolymer preserves the same crystal thickness, which was characteristic of the copolymer crystal.

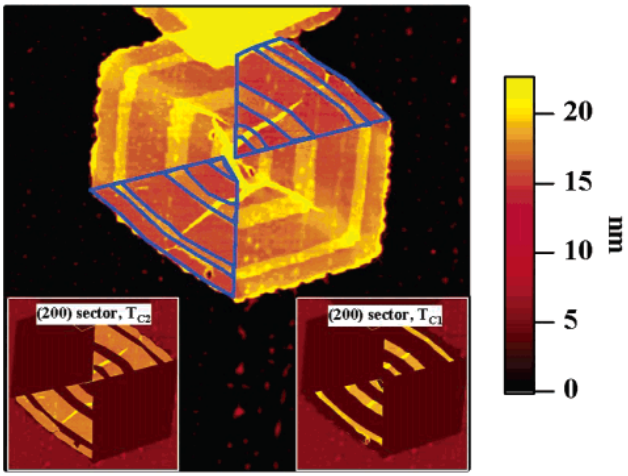

Figure IV.29. Literature data[100]: Tapping mode AFM images (13.0 x 13.0 μm^2) of a single LPE crystal prepared by alternate crystallization at T_{c1}) 98 and T_{c2}) 95 °C from *n*-octane. The crystal has four (110) sectors and two thinner (200) sectors. The most prominent feature of the crystal is a system of stripes of about 1.6 nm high running parallel to the crystal growth faces.

The second method to determine the crystal thickness is based on the overall lamellar thickness measurement and uses the assumption that the crystallinity calculated for the PEO block is constant and equal 95%[113]. This assumption is however difficult to check directly from the SAXS data, as we

have seen that the accuracy of the method does not allow obtaining reasonable values of the mass of the amorphous fold for the interlamellar regions strongly dominated by PS. It is however expected that the crystallinity will be affected by the degree of supercooling. Assuming a constant fold weight of PEO, the crystallinity will increase with the increase of the stem length. In the next section, we will consider the regimes of the PS brush on the surface of our lamellar crystals.

IV.3.3 *Identification of the PS brush stretching regime*

The free energy of a tethered polymer brush can be calculated as follows[105]:

$$f \sim kT\left(\frac{3l^2}{2Na^2}+\frac{\nu N^2 a^3 \sigma}{l}\right) \qquad \text{IV.11.}$$

where the l is the thickness of the tethered chain layer in solution, ν is the excluded volume parameter, a, N are the segmental size and length of the tethered chain and σ is the grafting density, i.e. the reciprocal of the surface per chain. The equilibrium thickness, l, can be obtained by a minimization of the f with respect to l in Eq. (IV.11):

$$l_{eq} \sim N\nu^{1/3}a^{5/3}\sigma^{1/3} \qquad \text{IV.12.}$$

whereas the equilibrium free energy can be written:

$$f_{eq} \sim kTNa^{4/3}\nu^{2/3}\sigma^{2/3} \qquad \text{IV.13.}$$

The corresponding extra-surface energy due to the PS chain stretching can be obtained from Eq. IV.13 by multiplying it by the surface per chain:

$$\gamma_{PS} = \sigma f_{eq} \sim kT\tilde{\Sigma}^{5/3}Na^{-2/3} \qquad \text{IV.14.}$$

In Eq. IV.14, $\tilde{\Sigma}$ stands for the dimensionless tethering density, which is defined as follows :

$$\tilde{\Sigma} = \sigma\pi R_g^2 \qquad \text{IV.15.}$$

In Eq. IV.15 R_g denotes the radius of gyration of a tethered chain in its end-free state in the same conditions. It follows then that the free energy scales with $\tilde{\Sigma}$. It is noteworthy that the given scaling relations are essentially valid for the highly stretched regime.

The reduced tethering density can be computed in our case using the data of *Cheng*[102] on the radius of gyration of sharp fractions of PS in amyl acetate.

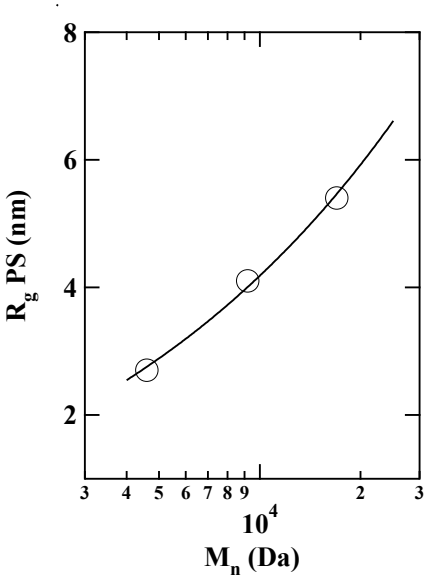

Figure IV.30. Literature data[102]: dependence of R_g of PS in amyl acetate at 30°C on the molecular weight. The solid line is a fit with a power function.

We can now recalculate the data given in figure IV.26 in terms of the dimensionless tethering density. The results are shown in figure IV.31. It can be seen that for the high MW of PEO the spatial confinement for the PS block correspond to just a slightly perturbed coil conformation. However, as soon as one decreases the length of the PEO block, the PS coils get more and more squeezed. Eventually, for the shortest PEO blocks the tethering density reaches quite high values of about 15-17. In this case, the interlamellar amorphous regions contain almost pure PS blocks. The dependence rate of $\tilde{\Sigma}$ on the PEO

length even increases in this region, which is contrary to the trend observed in the works of *Cheng*[102] at the $\tilde{\Sigma}$ values above approximately 3.7. So in our case the PEO crystals with significant thickness can still form by overcoming the steric repulsion of the PS coils.

If one inquires why the transition to the highly stretched regime is not visible in our experiments or maybe simply occurs later than reported by *Cheng*[102], the answer could bring us outside the scope of the conventional scaling and SCF models cited previously. Indeed, in the seminal works of *Kent* and co-authors (cf. for example ref. [114]), it was observed that the surface pressure of PS coils submerged in a good solvent exhibited a much stronger power law dependence on σ than the one predicted by these theories. The experimental observations suggested a soft-sphere-with-hard-core model based on an assumption of limited lateral interpenetration of the polymer coils. However, the values at which the surface pressure was sharply increasing were not scaling precisely with R_g implying that in both good and theta solvents, the chains of higher molecular weight can be compressed to a smaller fraction of *Rg* before the hard-core-like behavior occurs. Also, in some other works[115] the transition to the strongly stretched brush was found to occur at $\tilde{\Sigma}\sim 6$, which could indirectly

support our questioning. Also, in contrast to the scaling and SCF theories, *Kent* and co-authors[114] observed a depletion layer close to the surface. The presence of such layer can probably account for the very possibility of the amorphous PEO folds to coexist with a strongly stretched PS brush.

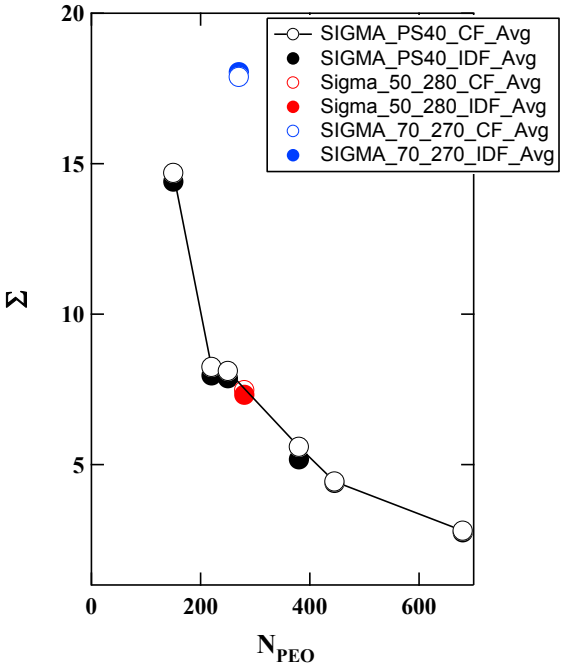

Figure IV.31. Reduced tethering density as a function of the PEO block length. The solid line is a guide to the eye.

IV.4. Conclusions

The semicrystalline morphology of PS-*b*-PEO crystals was addressed in the first part of this chapter. By combining the AFM and SAXS/WAXS data, we have determined the micro-structural parameters of the lamellae such as the crystal and amorphous layer thickness and the nearest-neighbor distance, or long period. It was shown that the crystals formed from the diblock copolymers containing low MW PEO exhibit a characteristic lens-shape, which was tentatively assigned to the sample polydispersity revealed during crystallization-induced chain fractionation. A comparison of the AFM and SAXS distance distributions showed a relatively good agreement in all the cases, including the non-uniform lens-shaped lamellae.

In the second part of the chapter, we analyzed the state of the tethered PS brush and tried to identify the morphological parameter sensitive to the stretching of the PS brush. We failed to visualize the transition to the highly stretched brush regime from the slopes of the crystallization lines in the Gibbs-Thomson coordinates, as it was done previously by the group of Cheng[102,113]. One of the reasons for this failure can be due to a limited accuracy of the crystal thickness measurements by SAXS, which indeed seems by far insufficient for such discrimination. Another reason can be

due to the fact that the slopes of the crystallization lines do not contain the thermodynamic information that one could easily extract. In particular, we believe that one cannot analyze the crystallization lines in the same way as it is done for the melting lines in order to compute for example the surface free energy. In this context, it is appropriate to recall that polymer crystallization is essentially determined by kinetics.

IV.5. References

100. Dubreuil, N.; Hocquet, S.; Dosière, M.; Ivanov, D. A. *Macromolecules,* **2004**, *37*, 1.
101. Alcazar, D.; Thierry, A.; Schultz, P.; Kawaguchi, A.; Cheng, S.Z.D.; Lotz, B. *Macromolecules* **2006**, *39,* 9120.
102. Zheng, J.X.; Xiong, H.; Chen, W.Y.; Lee, K.; Van Horn, R.M.; Quirk, R.P.; Lotz, B.; Thomas, E.L.; Shi, A.-C.; Cheng, S.Z.D. *Macromolecules* **2006**, *39,* 641.
103. Hocquet, S.; Dosière, M.; Thierry, A.; Lotz, B.; Dubreuil, N.; Ivanov, D. A. *Macromolecules,* **2003,** *36*, 8376.
104 De Gennes, P.G. *J. Phys. (Paris)* **1976**, *37*, 1443.
105 De Gennes, P.G. *Macromolecules*, **1980** *13*, 1569.
106 De Gennes, P.G. *C.R. Acad. Sci. (Paris)* **1985**, *300*, 839.
107 Semenov, A.N. *Sov. Phys. JETP* **1985**, *61*, 733.
108 Milner, S.T.; Witten, T.A.; Cates, M.E. *Macromolecules* **1988**, *21*, 2610.
109 Zhulina, E.B.; Priamitsyn, V.A.; Borisov, O.V. *Polym. Sci. USSR* **1989**, *31*, 205.
110 Zhulina, E.B.; Borisov, O.V.; Priamitsyn, V.A. J. *Colloid. Interf. Sci.* **1990**, *137*, 495.
111. DiMarzio, E. A.; Guttman, C. M.; Hoffman, J. D. *Macromolecules* **1980**, *13*, 1194.
112. Birshtein, T. M.; Zhulina, E. B. *Polymer* **1990**, *31*, 1312.
113. Chen, W. Y.; Zheng, J. X.; Cheng, S. Z. D.; Li, C. Y.; Huang, P.; Zhu, L.; Xiong, H.; Ge, Q.; Guo, Y.; Quirk, R. P.; Lotz, B.; Deng, L.; Wu, C.; Thomas, E. L. *Phys. Rev. Lett.* **2004**, *93*, 028301.
114 Kent, M. S.; Majewski, J.; Smith, G. S.; Lee, L. T.; Satija, S. *J. Chem. Phys.*, **1998**, *108*, 5635.
115 Wu, T.; Efimenko, K.; Genzer, J. *J. Am. Chem. Soc.* **2002**, *124*, 9394.

chapter V Morphological evolution of PS-b-PEO single crystals on heating

The thermal reorganization of single crystals of PS-b-PEO diblock copolymers is studied by a combination of in-situ AFM and variable-temperature SAXS/WAXS. We explore the differences in the reorganization behavior of single crystals formed by PS-b-PEO diblock copolymers with different lengths of the PEO block and try to correlate them to the stretching regime of the PS brush formed on the lamella surface.

V.1. Introduction

In the previous chapter, we analyzed the semicrystalline morphology of single crystals of PS-b-PEO block copolymers grown from dilute solutions in an attempt to correlate it to the stretching regime of the PS brush. Here the same goal is pursued using the thermal annealing of our single crystal preparations. To this end, a combination of in-situ AFM and variable-temperature SAXS/WAXS is used to explore in-depth the lamellar thickening on heating.

It is clear that the reorganization behavior in the course of annealing experiments depends on several factors such as the initial organization of the polymer chains within the lamella, the overall thermodynamic parameters of the crystal and the details of the possible thermally-activated diffusion motion of the chains. In the literature, numerous examples show the irreversibility of lamellar thickening with annealing temperature or time. Several models[116,117] were proposed for interpretation of the morphological changes occurring on annealing. Thus, it was found that for the melt-crystallized spherulite morphology, the chain entanglements often prevent the stems from sliding along the longitudinal chain direction

within the crystalline lamellae, which results in the melt-recrystallization to occur upon annealing. In contrast, for the less entangled solution-crystallized crystals, the lamellar thickening becomes probable. *Spells* and co-workers[118] have shown that the lamellar thickening during the annealing of a solution-grown crystal mat could happen without melting, depending on the annealing conditions such as the annealing temperature and heating rate.

In our studies we will perform the annealing experiments in order to clarify the temperature- and time-dependence of the semicrystalline morphology for single crystals of PS-*b*-PEO block copolymers having different lengths of the PEO block. The obtained SAXS results will be discussed using the Gibbs-Thomson plots to evaluate the temperature evolution of the lamellar morphology and extract the main thermodynamic parameters of the PS-*b*-PEO single crystals.

V.2. *Annealing of PS-b-PEO single crystals, as visualized with AFM*

In this section, we will present selected variable-temperature Tapping Mode AFM measurements carried out on single crystals of PS-*b*-PEO diblock copolymers. In the discussion, we will start from the two extreme cases identified in the previous chapter, i.e. the crystals of PS-*b*-PEO (40-150) and PS-*b*-PEO (40-680) copolymers.

V.2.1 Annealing of single crystals of PS-b-PEO (40-150)

The results of a typical variable-temperature AFM experiment conducted on single crystals of PS-*b*-PEO (40-150) formed at 25°C is given in figures V.1 through V.3. In this experiment, the sample temperature was raised in steps of 1.0 deg after capture of each image. Therefore the resulting heating program can be assimilated to a slow heating ramp, the rate of which is approximately 0.05°C/min.

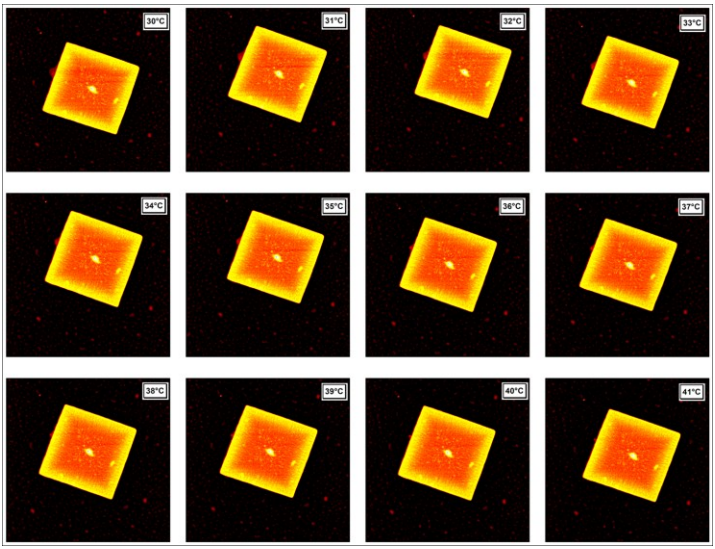

Figure V.1 Variable-temperature AFM images corresponding to heating of a single crystal of PS-*b*-PEO (40-150) starting from 30°C. The size of the image is 7.0 x 7.0 μm², the full vertical scale is 40 nm. The temperature of the AFM stage was increased in steps of 1.0 deg after capture of each image.

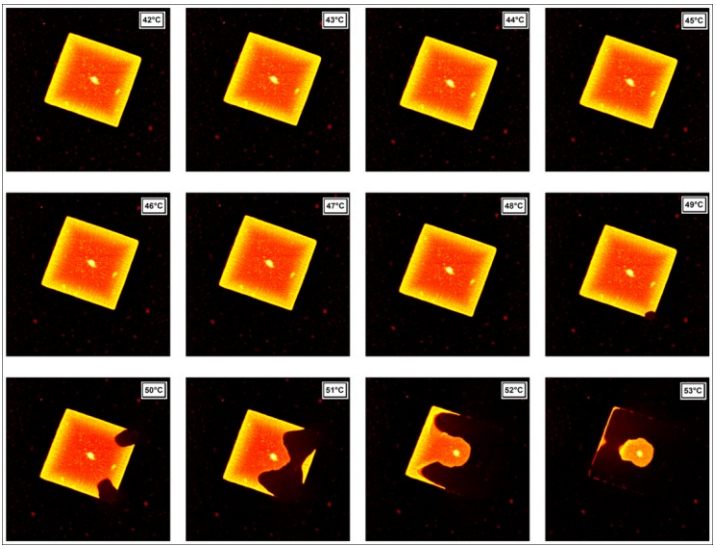

Figure V.2. Variable-temperature AFM images corresponding to heating of a single crystal of PS-*b*-PEO (40-150). The legend is similar to that of figure V.1.

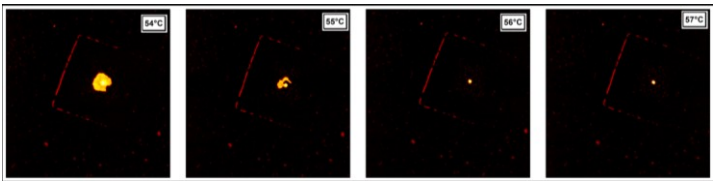

Figure V.3. Variable-temperature AFM images corresponding to heating of a single crystal of PS-*b*-PEO (40-150). The legend is similar to that of figure V.1.

The studied crystal show the conventional square habit described in detail in Chapters II and IV. The chosen color code allows visualizing the height distribution across the crystal and, in particular, the pronounced lens-shape feature, which, as we have seen

previously, is characteristic of diblock copolymers with low MW of PEO.

From the image sequence, it can be seen that there is almost no modification of the crystal morphology till about 48°C. Starting from 49°C, the crystal melting sets. First it affects the crystal corners and later on, in the range of temperatures from 51 to 53°C, it spreads over the entire crystal surface. At 53°C, only a part of the crystal interior remains in the solid state, although even this region is not intact anymore because it has already undergone some thickening. The last several images acquired at temperatures above 54°C (Fig. V.3) show a largely molten object where the remnants of the initial crystal can be only guessed from the contour line of the melt. Summarizing, the investigated single crystal show a very limited extent of reorganization on heating. More detailed information on the crystal evolution on heating can be extracted from the corresponding height histograms.

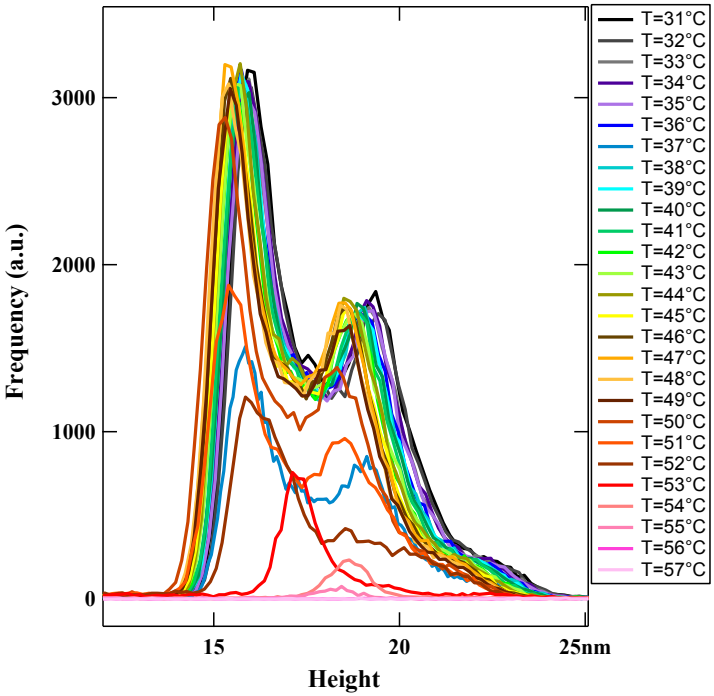

Figure V.4. Height histograms corresponding to the AFM image sequence given in figures V.1 through V.3.

Figure V.4 shows the height histograms corresponding to this heating experiment overlaid. The bimodal height distribution reflects the morphology of the initial lens-shaped crystal where the crystal center and periphery are located at smaller and larger heights, respectively. It can be seen that, even before the melting sets in, the positions of both maxima slightly move to smaller height. This height variation may be related to some softening of the

PS blocks decorating the lamellar surface and consequently to a larger deformation of the lamella induced by the tapping tip. Starting from 52°C, the amplitude of both distribution peaks strongly decreases due to crystal melting. Interestingly, the amplitude of the second height distribution, i.e. the one at larger heights, decreases even faster than that of the first one. Eventually, at 53°C, only the crystal center remains, but the height of these regions has been slightly increased so that the remaining peak is located in-between the two peaks of the initial bimodal height distribution.

It is important to understand whether the single crystals formed from PS-*b*-PEO (40-150) can thicken in principle or the result that we just described is valid notwithstanding the annealing conditions. To check this, we decided to perform another heating experiment but at a much slower heating rate. In this case, the temperature was increased from one AFM image to the next in steps of only 0.1 deg. The results are shown in figures V.5 through V.8. Due to a large number of AFM images, we show only the ones acquired above 52°C.

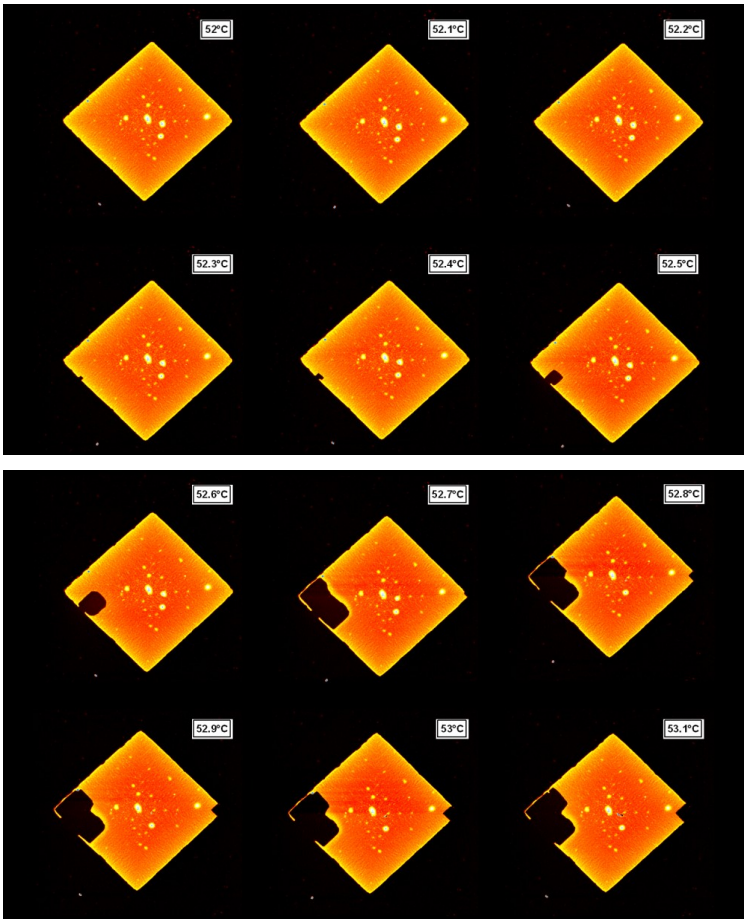

Figure V.5. Variable-temperature AFM images corresponding to heating of a single crystal of PS-*b*-PEO (40-150) starting from 30°C. The size of the image is 10.0 x 10.0 μm², the full vertical scale is 40 nm. The temperature of the AFM stage was increased in steps of 0.1 deg after capture of each image.

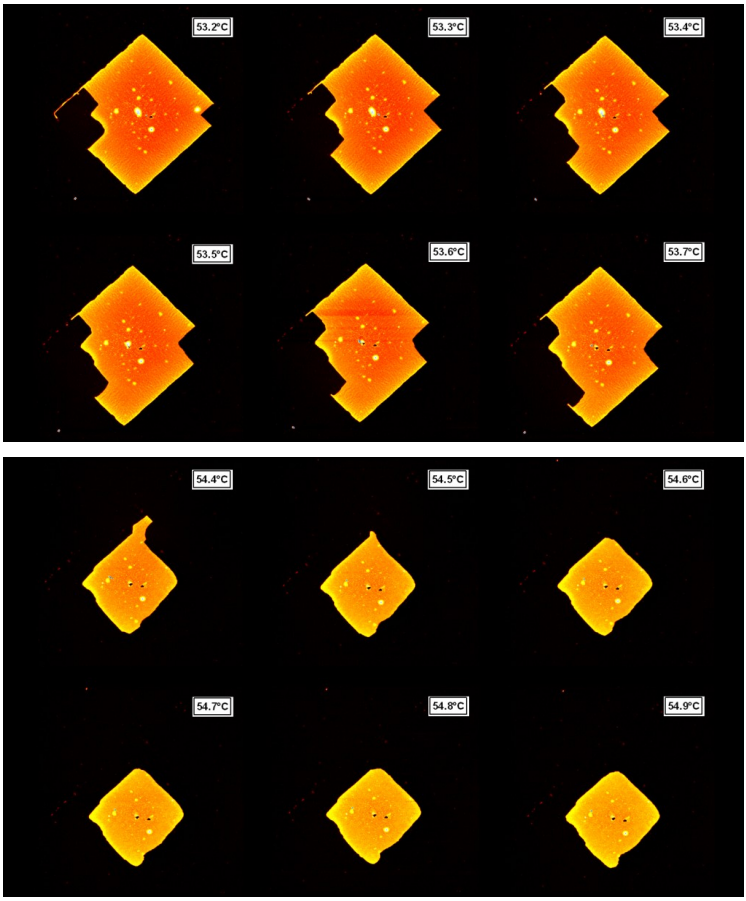

Figure V.6. Variable-temperature AFM images corresponding to heating of a single crystal of PS-*b*-PEO (40-150). The legend is similar to that of figure V.5.

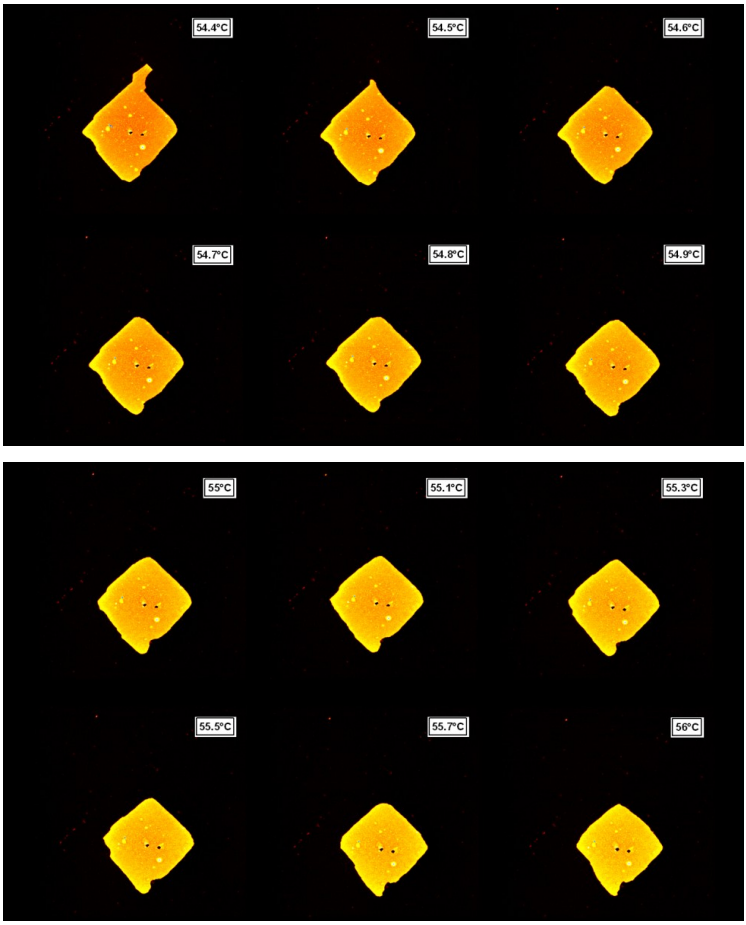

Figure V.7. Variable-temperature AFM images corresponding to heating of a single crystal of PS-*b*-PEO (40-150). The legend is similar to that of figure V.5.

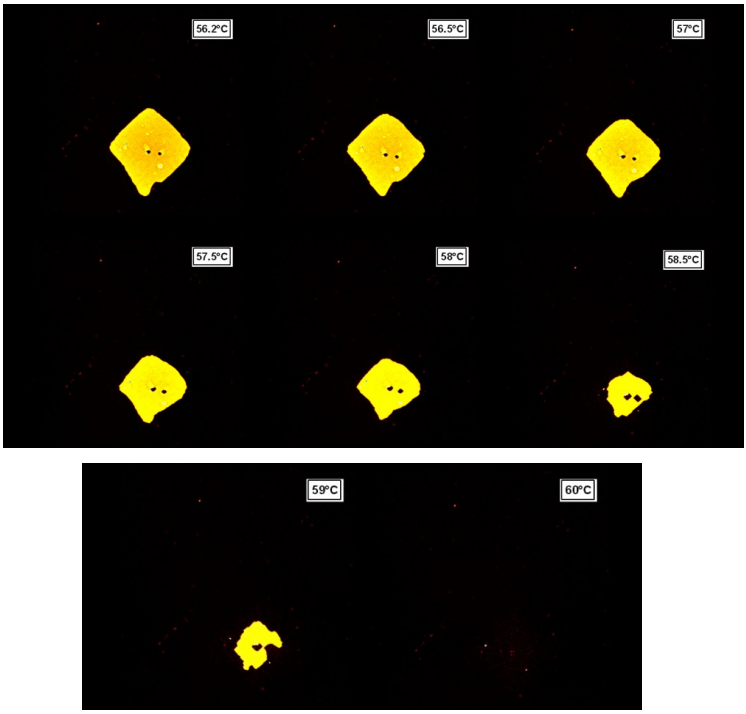

Figure V.8. Variable-temperature AFM images corresponding to heating of a single crystal of PS-*b*-PEO (40-150). The legend is similar to that of figure V.5.

Even a rapid examination of the image sequence given in figures V.5-V.8 shows that at this extremely slow heating rate the thermal behavior of the crystal is very different from the one discussed before. First of all, the melting process does not extend over the entire crystal surface as rapid as it was previously. Instead, the molten areas stay delimited by well defined boundaries, which run perpendicular or parallel to the main growth faces of

the crystal. Second, the crystal survives to a much higher temperature, i.e. approximately 59°C versus 54°C in the previous case. Third, the color code of the presented images clearly shows that the regions of the crystal surviving to such high temperatures are visibly thickened. Thus, the crystal center seems to be fully reorganized above approximately 55°C. To examine the crystal evolution with more scrutiny we turn to consideration of the corresponding height histograms.

Figure V.9 shows the height histograms calculated from images in figures V.5 through V.8. It can be seen that upon annealing the amplitude of the histogram peak decreases while its maximum shifts toward larger heights. Therefore, the crystal thickening, although being limited, is clearly operational during this heating ramp. The full range of the lamellar thickness increase is from approximately 16 to 22 nm.

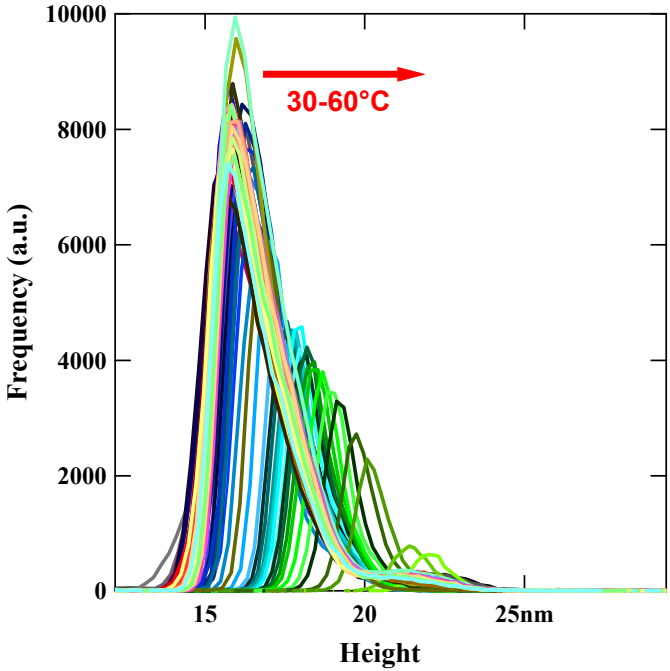

Figure V.9. Height histograms corresponding to the AFM image sequence given in figures V.5 through V.8.

The comparison of the height histograms given in figures V.4 and V.9 prompts us suggesting that the crystal thickening kinetics does play a role in the thermal behavior of PS-*b*-PEO crystals. Therefore the time-dependence of the reorganization processes occurring on heating cannot be fully disregarded in the analysis of the thermodynamic stability of these crystals. Importantly, the observed increase of the lamellar thickness is continuous, i.e. the transitions between the different IF

forms are not detected. If at the beginning the crystals of PS-*b*-PEO (40-150) contain essentially twice-folded chains, the thickening transition should bring them at some point to the state of once-folded chain crystals, which should be accompanied by a crystal thickness increase of 6.8 nm. In addition, the PS brush will also increase its height due to the increased lateral squeezing. Thus the total lamellar thickness increase accompanying the IF2→IF1 transition should be equal to 11.7 nm. The observed height increase is clearly smaller (ca. 6 nm), which can probably be accounted for softening of the PS block with temperature increase, similar to what was pointed out in the discussion of height histograms given in figure V.4. Therefore it cannot completely ruled out that this extremely slow heating ramp brings the F2 crystals to the F1 state. Due to the continuity of the height histogram variation this transition likely occurs via the NIF forms.

At the present stage, it does not look realistic to explore the thickening kinetics within a broader time-scale as the duration of the experiments will become unreasonably high. However even the range of heating rates explored in this work allows to clearly show that the

reorganization behavior of the PS-*b*-PEO crystals is in fact time-dependent, which adds more complexity for the analysis of the thermodynamic parameters of these systems.

V.2.1 Annealing of single crystals of PS-b-PEO (40-680)

In this section, we present AFM annealing experiment conducted on single crystals of PS-*b*-PEO (40-680) formed at 35°C.

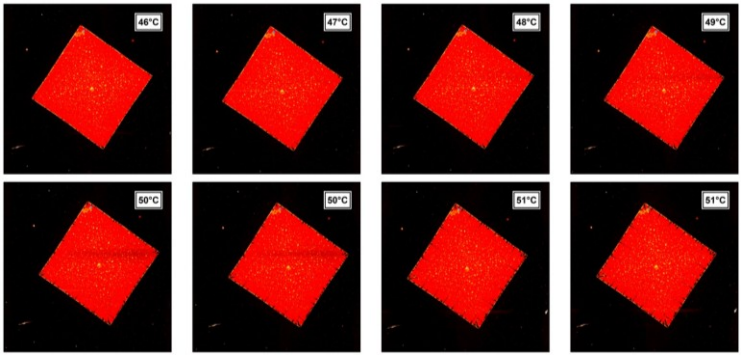

Figure V.10. Variable-temperature AFM images corresponding to heating of a single crystal of PS-*b*-PEO (40-680) formed at 35°C. The size of the image is 30.0 x 30.0 μm², the full vertical scale is 30 nm. The temperature of the AFM stage was increased in steps of 1.0 deg after capture of each image.

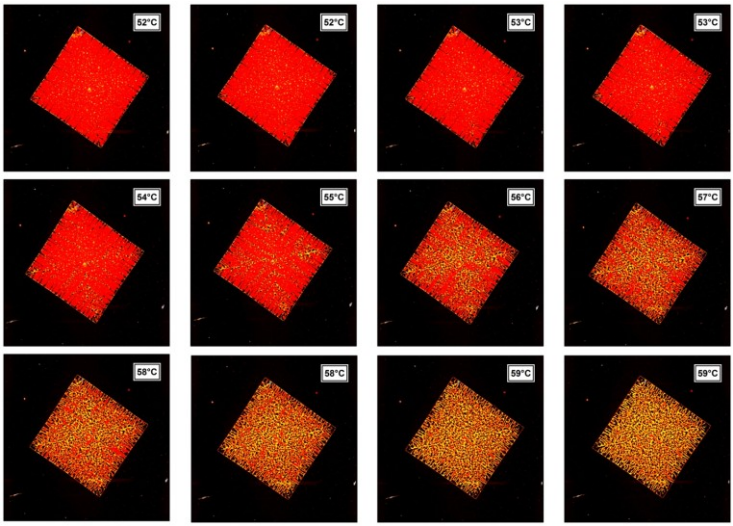

Figure V.11. Variable-temperature AFM images corresponding to heating of a single crystal of PS-*b*-PEO (40-680). The legend is similar to that of figure V.10.

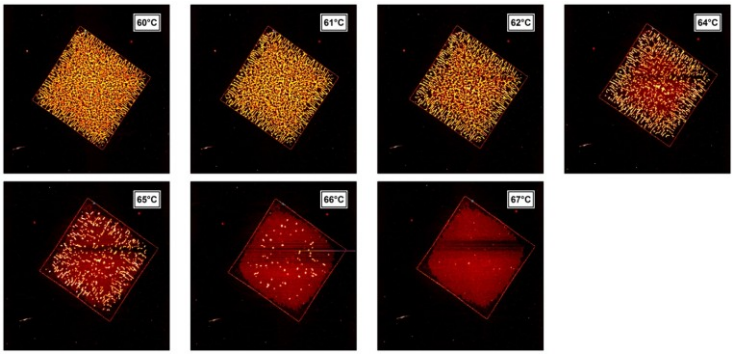

Figure V.12. Variable-temperature AFM images corresponding to heating of a single crystal of PS-*b*-PEO (40-680). The legend is similar to that of figure V.10.

The morphological evolution of the crystal is obviously very different from what we have seen previously for PS-*b*-PEO (40-150) crystal. The thermal reorganization starts approximately at 49°C by visible "cracking" of the crystal edges. The molten regions appear in the form of thin stripes running perpendicular

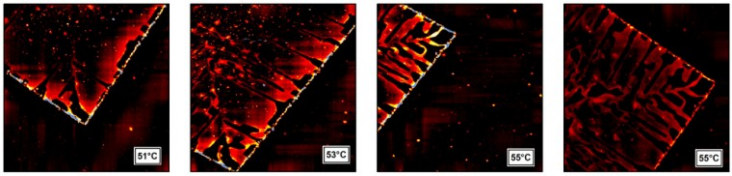

Figure V.13. Higher resolution images of PS-*b*-PEO (40-680) acquired during heating of a single crystal (cf. Fig. V.10-V.12). The size of the images is 5.0 x 5.0 μm².

to the crystal edges. Interestingly, the stripes are stopped by the sector boundaries and are thus confined to the same sector. Selected magnified views of this morphology are given in figure V.13. Here one can see more clearly the formation of "cracked" faces, thickened regions bordering the molten stripes and crystal sector boundaries.

At an even more advanced stage of the crystal reorganization, i.e. above approximately 59°C, all the remaining regions have already undergone significant

thickening. Starting from this temperature, the fraction of the remaining regions decreases while their height keeps on increasing. The crystal melts completely at 67°C. This is much higher than the melting point of the PS-*b*-PEO (40-150) crystal heated at the same rate. The main reason for that is a significant morphological reorganization accompanying the heating ramp of the PS-*b*-PEO (40-680) crystal. More information on the height evolution can be obtained from the corresponding AFM histograms.

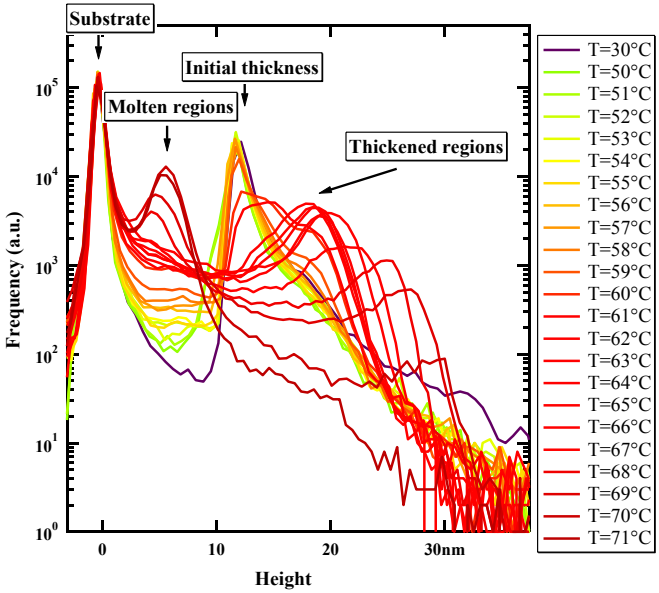

Figure V.14. Height histograms corresponding to the AFM image sequence given in figures V.10 through V.12.

Figure V.14 shows height histograms computed for the AFM image sequence shown in figures V.10-V.12. For convenience, the data is displayed in a semi-log graph. Apart from the substrate peak, which was set at zero height, the histograms at the beginning of the experiment show the main peak located at about 11.5 nm. Although this peak stays invariable till approximately 56°C, a shoulder appears at larger heights already at 55°C. Starting from 56°C, the main peak reveals a complex bimodal shape, with the second component being centered at 18.5 nm. Later on, the first component at the position of the initial peak disappears at the expense of the second one. The gradual shift of the latter to larger heights continues till the final melting of the crystal. The maximum crystal thickness detected in this experiment is about 30 nm, which means that the initial crystal was thickened almost by a factor of three. This corresponds to an approximate change from F19 to F6 crystals.

The fact that in a certain temperature range we observe a coexistence of regions having the initial and increased thickness likely suggests that during heating the crystal dwells in a metastable state and the thickening

kinetics is important, similar to what was found for the PS-*b*-PEO (40-150) crystal.

V.3.1 Annealing of single crystals of PS-b-PEO (40-250)

In this section, we present an AFM image sequence corresponding to annealing of one additional block copolymer, which is intermediate between the two extreme cases of the studied diblock copolymer crystals, the PS-*b*-PEO (40-250) crystal.

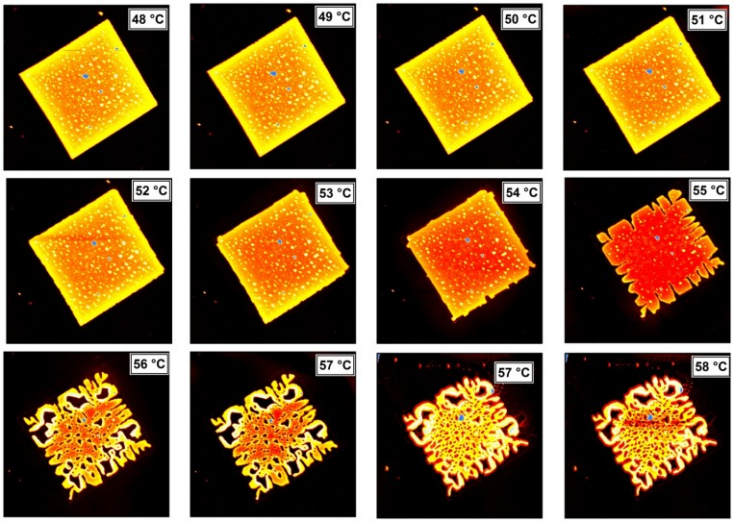

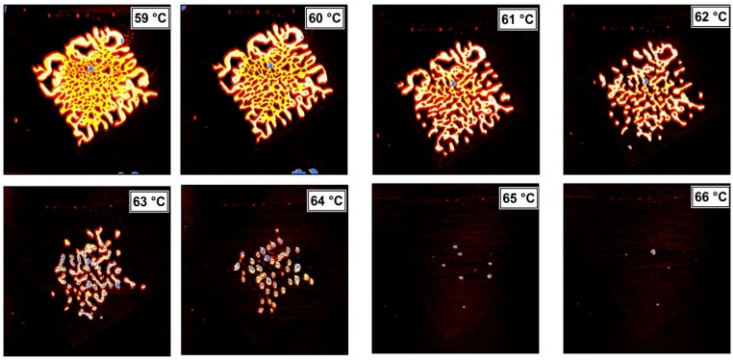

Figure V.15. Variable-temperature AFM images corresponding to heating of a single crystal of PS-*b*-PEO (40-250) formed at 30°C. The size of the image is 15.0 x 15.0 μm², the full vertical scale is 30 nm. The temperature of the AFM stage was increased in steps of 1.0 deg after capture of each image.

As can be seen in figure V.15, the thermal behavior of this crystal reveals some similarities with that of the previously studied PS-*b*-PEO (40-680) crystal. In particular, the reorganization starts with "cracking" of the crystal facets, as it has just been documented before. However, in this case, the size of the forming stripes is much larger. We speculate that the stripes can be related to the secondary nuclei formed during crystallization from solution, as it has been visualized by *Lotz*[101] for single crystals of isotactic poly(vinyl cyclohexane), PVCH. Although AFM does not provide information on the molecular structure, as it is the case of dark field TEM in the work on PVCH, it is still reasonable to assume that

the grain boundaries between the secondary nuclei are constrained and melt earlier than any other regions of the crystal. Importantly, the orientation of these stripes and their width change in agreement with the predictions of the secondary nucleation theory. Indeed, for example the same type of morphology can be observed also for the PS-*b*-PEO (40-150) crystal at the extremely low heating rate applied (cf. Figs. V.5-V.6). The squared-shape molten regions can be assigned to the secondary nuclei, the size of which is comparable to that of the crystal. It is thus logical to assume that crystallization of the PS-*b*-PEO (40-150) proceeds in the mono-nucleation regime (regime I) as this compound indeed crystallizes most closely to its dissolution temperature. As soon as we increase the length of the PEO block, the crystallization temperature will move farther away from T_d, which will make the nucleation rate higher. Thus for the PS-*b*-PEO (40-250) crystal described above, the width of the stripes is intermediate between that of PS-*b*-PEO (40-150) and PS-*b*-PEO (40-680).

Apart from "cracking" of the growth front on heating, the PS-*b*-PEO (40-250) crystal undergoes significant thickening. For example, it can be seen (Fig.

V.15) that at 56 and 57°C the intact central regions coexist with somewhat thickened regions at the crystal edges. Figure V.16 shows the corresponding height histograms. First it can be noticed that the position of the initial peak slightly moves back on heating, which could be again accounted for by softening of the PS block. Second, starting from 56°C the shape of the peak significantly changes and new thickened regions appear. As in the case of the PS-*b*-PEO (40-680) crystal, the regions with different lamella thickness coexist in a certain temperature range. The ultimate lamella thickening ratio achieved just before the final melting point corresponds to approximately a factor of two.

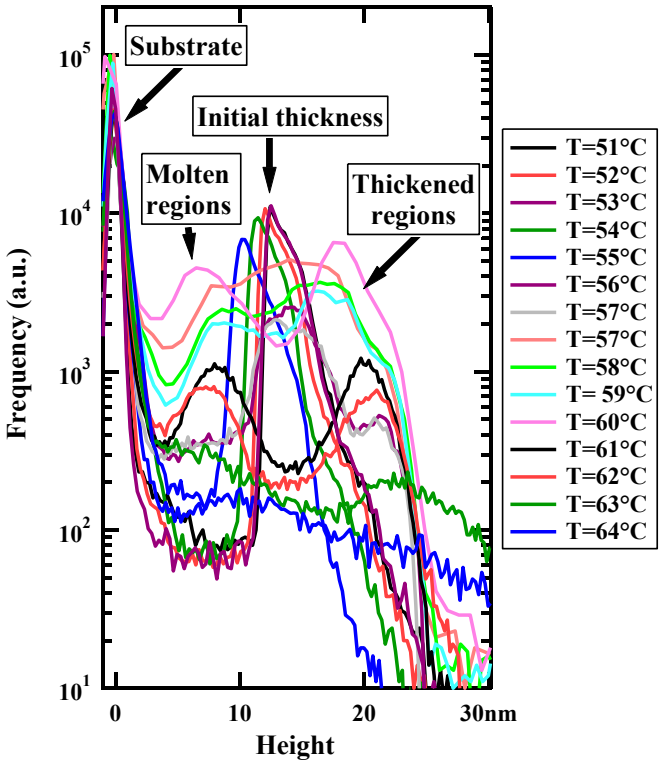

Figure V.16. Height histograms corresponding to the AFM image sequence given in figure V.15.

V.3. *Chain orientation in annealed PS-b-PEO single crystals: WAXS measurements*

In discussing the lamellar thickening based on AFM height histograms, it is essential to know the crystallographic orientation of the unit cell with respect to

the lamella basal plane. For example, it is crucial to know how the PEO chains are oriented in such a lamella. In the absence of such information, the AFM height histograms will not provide any information of the lamella thickness. As we have seen previously, in the initial crystals formed from solution, the PEO chains are normal to the lamella surface. This was confirmed by selected-area ED and also by WAXS measurements on oriented single crystal mats. However, it is also important to check the PEO chain orientation in real time during heating.

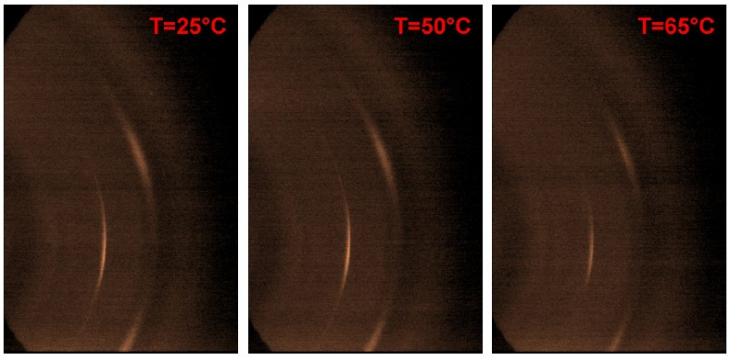

Figure V.17. Variable-temperature WAXS patterns corresponding to heating of a single crystal of PS-*b*-PEO (40-680) formed at 30°C.

Figure V.17 shows WAXS patterns corresponding to heating of PS-*b*-PEO (40-680) single crystal formed at 30°C. In figure V.17 we have selected three frames of this heating ramp to show that the PEO chain orientation stays always normal to the lamella basal plane. Therefore,

one can indeed quantitatively compare the height histograms for example with the results if variable-temperature SAXS. The fact that the chain orientation stays invariant during the thickening process indicates on the solid-state mechanism of this process. Thus it can be assumed that the thickening occurs via reputation motion of the chain within the crystal, without melting/recrystallization to occur.

V.4. *Annealing of PS-b-PEO single crystals: SAXS measurements*

In this section, variable temperature SAXS measurements corresponding to selected heating experiments on PS-*b*-PEO single crystal mats will be described.

V.4.1 Annealing of a single crystal mat of PS-b-PEO (40-150)

Figure V.18 displays the SAXS curves corresponding to a heating ramp carried out on a mat of single crystals of PS-*b*-PEO (40-150) formed at 25°C. The SAXS curves show the main interference maximum at approximately 0.006 $Å^{-1}$, which corresponds to the long period of the

system. It can be seen that the peak disappears shortly above 50°C. Moreover, the position of the peak does not change during the entire heating ramp. Therefore on can conclude that during this variable-temperature SAXS measurement the crystals of PS-*b*-PEO (40-150) behave in a similar way as in the AFM heating experiment at one degree per image, where the lamella thickness stayed practically constant. Thus at this and higher heating rates the crystal reorganization in PS-*b*-PEO (40-150) does not occur. It is therefore clear that to observe the lamellar reorganization at reasonable heating rates, one has to examine the copolymers with higher MW of PEO.

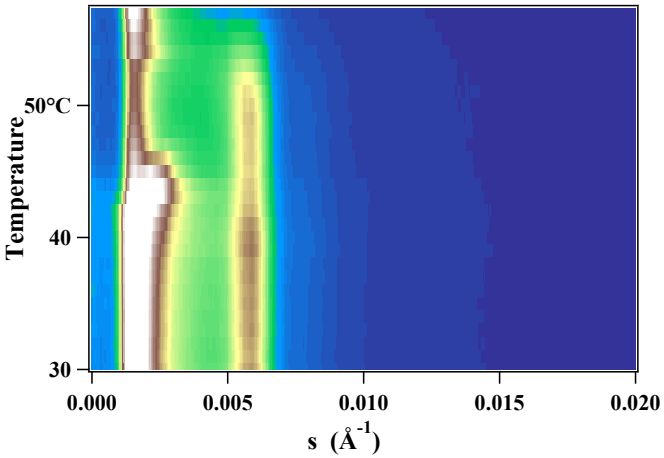

Figure V.18. SAXS intensity as a function of temperature corresponding to a heating ramp of PS-*b*-PEO (40-150) crystals formed

at 25°C. The heating rate is 2.5°C/min.

V.4.2 Annealing of a single crystal mat of PS-b-PEO (40-380)

When the degree of polymerization of the PEO block is increased to 380, one can indeed detect some traces of the lamellar reorganization.

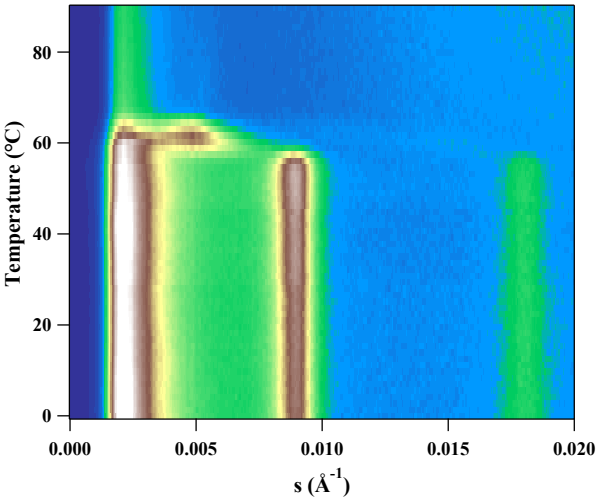

Figure V.19. Lorenz-corrected SAXS intensity as a function of temperature corresponding to a heating ramp of PS-*b*-PEO (40-380) crystals formed at 30°C. The heating rate is 3.5°C/min.

Indeed, as can be seen in figure V.19, above approximately 56°C the main interference peak disappears and, in a very small temperature range, one

can see the scattering from the thickened lamellae around 0.005 $Å^{-1}$. It is noteworthy that in this case the initial long period is significantly smaller than that of the PS-*b*-PEO (40-150) crystal.

The temperature range of reorganization observed for the PS-*b*-PEO (40-380) crystals is however too short to be addressed in detail. Therefore we have to increase even more the MW of the PEO block to observe this process clearly.

V.4.3 Annealing of a single crystal mat of PS-b-PEO (40-680)

The SAXS heating experiment on PS-*b*-PEO (40-680) single crystal mat is shown in figure V.20. The position of the main interference maximum stays invariant till approximately 55°C, and starts rapidly evolving thereafter.

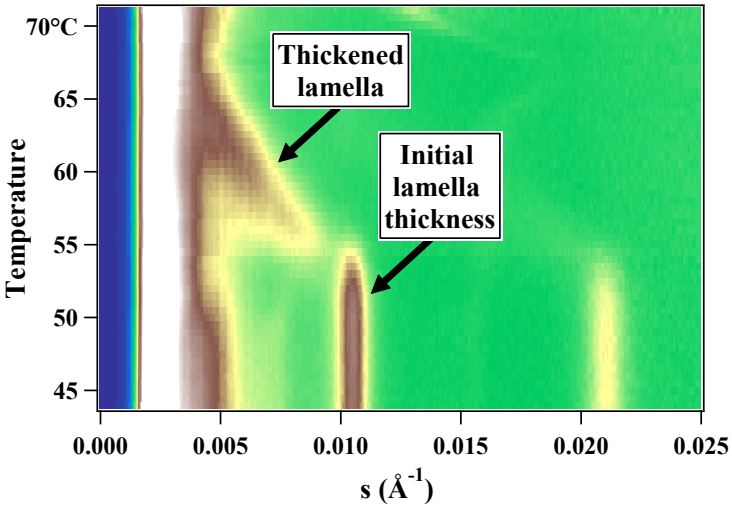

Figure V.20. Lorenz-corrected SAXS intensity as a function of temperature corresponding to a heating ramp of PS-*b*-PEO (40-680) crystals formed at 30°C. The heating rate is 1.0°C/min.

It is important to note that at the beginning of the structural evolution the change in the characteristic distance is discontinuous. Thus at approximately 55°C, two characteristic distances, i.e. the ones pertinent to the initial and thickened lamellae, coexist. This observation is in line with our AFM annealing experiments described previously. The coexistence of crystals with different thickness provides additional support to the view of the reorganization process as a sequence of metastable states, which are strongly dependent on the time-scale of experiment. Importantly, for this diblock copolymer with

the longest PEO block the thickening process occurs over more than ten degrees on heating, which is interesting to examine using the Gibbs-Thomson plot.

V.6. *Thermodynamics of the PS-b-PEO single crystals reorganization on heating: Gibbs-Thomson plots*

The Gibbs-Thomson plots corresponding to heating ramps of the PS-*b*-PEO (40-680) single crystals formed at 30 and 35°C are shown in figure V.21. The crystal thickness was evaluated according to the interface distribution function approach. The GT curves start at different values of crystal thickness, according to the crystallization temperature applied. At some temperature, the thermal reorganization sets in, which can be visualized as a departure of the GT curves from the initial vertical lines. Further thickening of the two single crystal preparations goes almost along the same line, and the final melting temperature of both samples is close. Therefore the initial state of the sample seems to be of minor importance for the thermal reorganization.

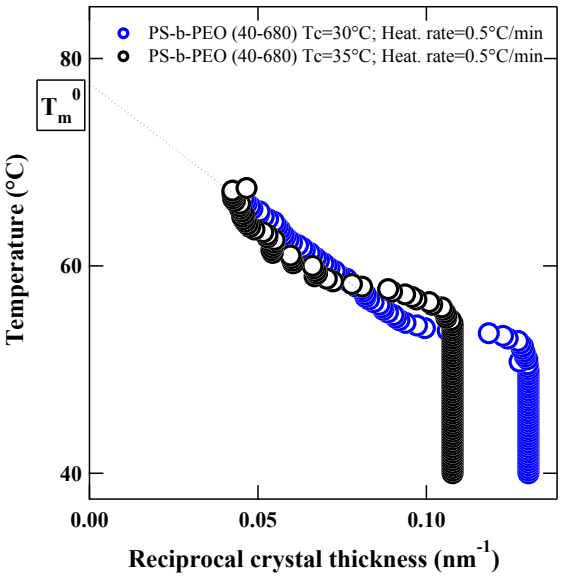

Figure V.21. Gibbs-Thomson plot corresponding to a heating ramp of PS-*b*-PEO (40-680) crystals formed at 30 and 35°C. The heating rate is 0.5°C/min.

If one assumes that the GT melting line corresponds to the coexistence line of the crystalline phase and melt, one can use it to extract the equilibrium melting temperature T_m^0 and fold surface energy of the lamellar crystals σ_e. Although we have already seen that the metastability of the crystal plays an important role in its evolution on heating, we decided to perform these simple estimations. Upon extrapolation of the linear fit to the origin, one gets T_m^0 of 78°C, which is in the range of the values widely accepted for PEO[119]. Using the theoretical

enthalpy of melting of 100% crystalline PEO of 200 J/g[119], one obtains from the slope of the GT curves the surface energy σ_e of 89 J/m^2. This value is close to the one used for example by *Cheng*[39] for PEO chains of large MW. At the same time, this value is much bigger than the σ_e used by other authors (cf., ref. 120). As far as linear PE is concerned, the σ_e values of 90 J/m^2 are conventionally used for the analysis of the crystallization kinetics.[121]

Figure V.22 shows the GT curves corresponding to the PS-*b*-PEO (40-445) single crystals. In this case, we were also able to detect by SAXS the thermally-induced crystal reorganization, which extended over several degrees.

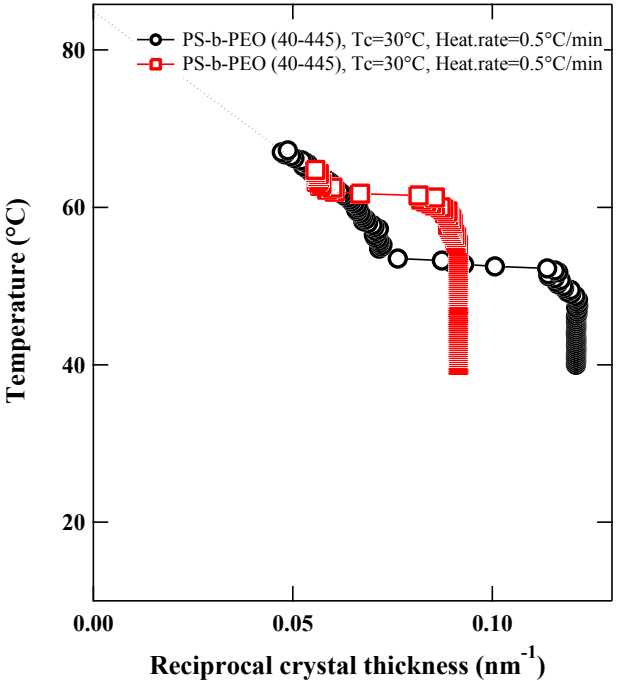

Figure V.22. Gibbs-Thomson plot corresponding to a heating ramp of PS-*b*-PEO (40-445) crystals formed at 30 and 35°C°C. The heating rate is 0.5°C/min.

The curves shown on the plot correspond to two different crystallization temperatures employed. It can be seen that in the final stage of reorganization the two curves merge on one reorganization line. Thus the thermal behavior of these crystals exhibit the same tendency observed for PS-*b*-PEO (40-680) single crystals. However in this case the extent of the linear portions of the curves does not provide enough accuracy in

evaluating the thermodynamic melting temperature and the surface energy.

V.7. *Conformation of the tethered PS brush during annealing of PS-b-PEO single crystals*

It is clear that the size of PS coils in a good solvent

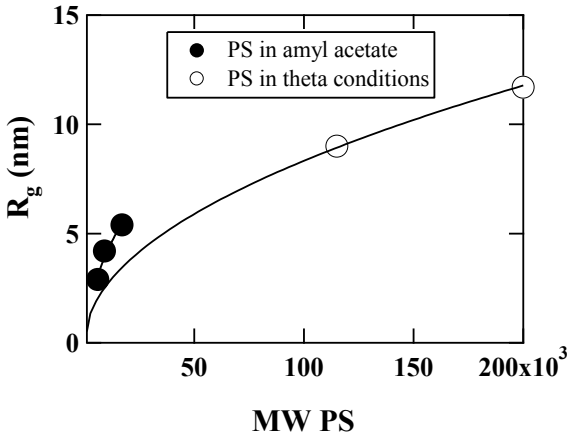

Figure V.23. Literature data on the size of PS coils in amyl acetate[102] and in a θ-solvent[122]. The solid lines are power law fits to the data.

such as amyl acetate is rather different from that in the melt. Figure V.23 shows the literature data on the radius of gyration of PS in amyl acetate and in a theta-solvent as a function of molecular weight. From this data, one can

estimate the relative swelling of PS in a good solvent with respect to theta conditions. Thus for the length of PS block equal 40, the swelling ratio equals approximately 1.8. This value will be important for understanding the state of the PS brush during thermal annealing of PS-*b*-PEO crystals.

Thus if we start our consideration from the PS-*b*-PEO (40-150) single crystals, one has to note that upon solvent drying the dimensionless tethering density of PS decreases from 15 to about 4.4. Therefore in the dry state the PS brush is in a much more relaxed state than it was in the "mother" solution, which is in line with results described in section IV.2.6. It is thus not surprising that the PS-*b*-PEO (40-150) single crystals can thicken upon annealing. Indeed, the supposedly observed structural transition from F2 to F1 crystal does not even bring the PS brush to the same level of constraints as it was in the initial solution. As far as block copolymers with high MW of PEO are concerned, the observed crystal thickening does not increase the reduced tethering density to the values where one could expect to see the consequences on the crystal's thermodynamics. Therefore probably the only way to detect the impact of the PS brush stretching

will be to perform an extremely slow heating of PS-*b*-PEO (40-150) single crystals to visualize their possible transition to the extended-chain state.

Another point to address is the glass transition temperature of PS and its influence on the structural evolution of crystals on heating. Indeed, if one measures the glass transition temperature of sharp fractions of PS, it can be found for example that T_g for PS of 3.9 kg/mol is about 81°C (cf. Fig. V.24). Although in our experiments the vitrification of the PS layer decorating the PS-b-PEO crystals was not found to control the crystal reorganization as it was for example the case in a previous work,[82] some softening of the PS block on heating is supposedly happening. Therfore we believe that the glass transition temperature of the PS-decorated lamella surface occurs at about room temperature.

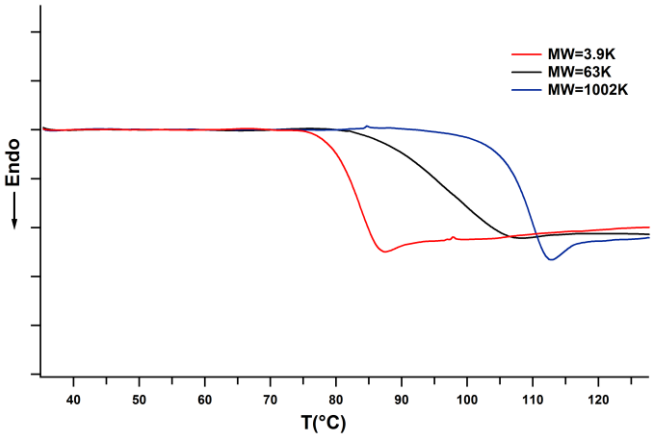

Figure V.24. DSC curves corresponding to sharp fractions of PS.

A possible reason for this could be the glass transition temperature depression of the PS layer due to spatial confinement, as was discovered for example by *Keddie*, *Jones*, and *Cory*[123] on the basis of ellipsometric measurements.

V.8. Conclusions

The studies of the thermal annealing behavior of PS-*b*-PEO single crystals with the help of *in-situ* AFM and variable-temperature SAXS show that the crystals undergo thermally-induced thickening. The thickening process is the most pronounced for the block copolymers containing long PEO blocks, whereas it stays rather limited for the PEO blocks of shorter length.

During the lamellar thickening process, the chain orientation of the PEO is kept perpendicular to the lamella basal plane. This indicates on the solid-state chain diffusion as the main mechanism of the lamellar thickening process, i.e. the crystals thicken without melting/reorganization process to occur. This is similar to the mechanisms for the NIF→IF transitions reported previously.

By analyzing the lamella thickening occurring at different heating rates it was found that the thickening process is largely time-dependent. Thus the single crystals of PS-*b*-PEO (40-150) do not exhibit thickening at heating rates above approximately 0.05 deg/min. However, they do thicken at much lower heating rates. Therefore the thickening process occurs via a sequence of metastable states such as NIF forms.

The temperature evolution of single crystals starts from a discontinuous variation of the lamellar thickness whereby regions with different thickness coexist.

The lamella thickening for the same block copolymer was found to be largely independent of the initial lamella thickness. Thus the Gibbs-Thomson melting lines

corresponding to single crystals formed at different crystallization temperatures merge at the final stage of the lamella reorganization.

V.9. References

116 Wunderlich B. Macromolecular physics. New York: Academic Press, 1976.

117 Bassett DC. Principles of polymer morphology. London: Cambridge University Press, 1981.

118 Sadler DM, Spells SJ. Macromolecules 1989;22:3941

119 Yang, Z.; Cooke, J.; Kyriakos Viras; Gorry, P.A.; Ryan, A. J.; Booth, C. *J. Chem. Soc., Faraday Trans*. **1997**, 93, 4033.

120 Huang, X. D.; Goh, S. H. *Macromolecules* **2001**, *34,* 3302.

121 Hoffman, J.D.; Miller, R.L. *Polymer*, **1997**, *38*, 3151.

122 Melnichenko, Yu. B.; Wignall, G. D. *Physical Review Letters* **1997**, *78*, 686.

123 Keddie, J.L. ; Jones, R.A.L, Cory, R.A. *Europhys. Lett*. **1994**, *27*, 59.

Summary

Understanding the interplay between the amorphous and crystalline parts of the semicrystalline polymer structure is a long-standing issue in polymer physics. In particular, for linear crystalline-amorphous diblock copolymers the amorphous block can control the crystallization process and the resulting semicrystalline morphology.

In the present work, we have undertaken a structural study of PS-*b*-PEO single crystals to elucidate the influence of the state of the PS block on crystallization from dilute solution and on subsequent thermal annealing at elevated temperature. It is noteworthy that the interest in these systems has been recently renewed in the perspective of using them as a model of grafted amorphous brushes with variable grafting density. Indeed, during crystallization of PEO, the amorphous block, i.e. PS, is rejected from the crystal accumulating on its basal surfaces. Since the crystal thickness formed during isothermal crystallization is a sharply selected value, the grafting density of the resulting PS brush is also well defined. Therefore by

varying the crystal thickness one can obtain the PS brushes with grafting density varying in a broad range.

In our study, a combination of reciprocal and direct-space techniques such as SAXS/WAXS and AFM was employed. While AFM experiments were performed on isolated single crystals, the SAXS investigation was carried out on oriented mats of single crystals slowly sedimented from the "mother" solution. In this case, the one-dimensional two-phase system model was used for the data interpretation where the thickness of the amorphous (L_a) and crystalline (L_c) layers are conventionally determined following the correlation function and interface distribution function approaches.

1. We have shown that the crystals formed from the diblock copolymers containing low molecular weight PEO exhibit a characteristic lens-shape, which was tentatively assigned to the sample polydispersity revealed during crystallization-induced chain fractionation. A comparison of the AFM and SAXS distance distributions showed a relatively good agreement in all the cases, including the non-uniform lens-shaped lamellae.

2. In contrast to previous reports, we failed to visualize the transition to the highly stretched brush regime from the slopes of the crystallization lines in the Gibbs-Thomson coordinates. A possible reason for this can be due to a limited accuracy of the crystal thickness measurements by SAXS. Another reason can be due to the fact that the slopes of the crystallization lines do not contain the thermodynamic information that is easily extractable. In particular, we believe that one cannot analyze the crystallization lines in the same way as it is done for the melting lines in order to compute for example the surface free energy.
3. The studies of the thermal annealing behavior of PS-*b*-PEO single crystals show that the crystals undergo thermally-induced thickening. The thickening process is the most pronounced for the block copolymers containing long PEO blocks, whereas it stays rather limited for the PEO blocks of shorter length.
4. During the lamellar thickening process, the chain orientation of the PEO is kept perpendicular to the lamella basal plane. This indicates on the solid-state chain diffusion as the main mechanism of the lamellar thickening process, i.e. the crystals thicken without melting/reorganization process to occur.

5. By analyzing the lamella thickening occurring at different heating rates we found that the thickening process is largely time-dependent. Thus the single crystals of PS-*b*-PEO (40-150) do not exhibit thickening at heating rates above approximately 0.05 deg/min. However, they do thicken at much lower heating rates. Therefore the thickening process occurs via a sequence of metastable states.
6. The temperature evolution of single crystals starts from a discontinuous variation of the lamellar thickness whereby regions with different thickness coexist.
7. The lamella thickening for the same block copolymer was found to be largely independent of the initial lamella thickness: the Gibbs-Thomson melting lines corresponding to single crystals formed at different crystallization temperatures merge at the final stage of the lamella reorganization.

Résumé

La compréhension des interdépendances entre les régions amorphes et cristallines d'un polymère semicristallin est un sujet classique de la physique des polymères. Par exemple, pour des copolymères linéaires bi-séquencés contenant un bloc cristallisable et un bloc amorphe, il est connu que dans certaines conditions le bloc amorphe peut contrôler le processus de cristallisation et la morphologie semicristalline résultante.

Dans le travail actuel, nous avons entrepris une étude structurale des monocristaux de polystyrène-polyoxyde d'éthylène (PS-*b*-PEO) pour élucider l'influence de la conformation du bloc de PS sur la cristallisation de PEO à partir d'une solution diluée. Nous avons également étudié le comportement des monocristaux lors d'une chauffe.

Il est à noter que depuis des années 60 les monocristaux de PS-*b*-PEO ont fait l'objet de nombreuses études réalisées par l'équipe de recherche de *Lotz* et *Kovacs* de l'Institut Charles Sadron à Strasbourg. Ces auteurs étaient parmi les premiers à étudier l'influence du bloc amorphe sur la cristallisation des

copolymères bi-séquencés contentant un bloc cristallisable et un bloc amorphe. Leurs études ont permis d'aborder d'une façon intéressante des problèmes classiques qui existent dans le domaine de cristallisation des polymères et tirer des conclusions générales quant aux mécanismes moléculaires de cristallisation des homopolymères.

Récemment l'intérêt dans ces systèmes a été réapparu en vue de l'utilisation des monocristaux de copolymères pour générer des brosses amorphes uniformes. Lors de la cristallisation du PEO, le bloc amorphe, c. à d. le PS, est rejeté du cristal et s'accumule donc sur les surfaces basales des lamelles cristallines. Puisque l'épaisseur cristalline qui résulte d'un processus de cristallisation isotherme a une valeur bien définie, la densité de greffage de PS l'est aussi. Ainsi en changeant l'épaisseur du cristal nous pouvons générer des brosses de PS ayant des densités de greffage très variées.

Dans notre étude, nous avons employé une combinaison des techniques d'analyse qui sont opérationnelles dans l'espace directe et réciproque telles que l'AFM et le SAXS/WAXS. Les expériences AFM ont été réalisées sur des monocristaux isolés tandis que les mesures SAXS/WAXS ont été faites sur des gâteux de monocristaux orientés qui ont été préparés par

sédimentation lente à partir d'une solution diluée. L'interprétation des résultats SAXS se base sur le modèle à deux phases où les épaisseurs des régions cristallines (L_c) et amorphes (L_a) peuvent être déterminées en suivant les approches conventionnelles qui utilisent la fonction de corrélation ou la fonction de distribution des interfaces.

Le premier chapitre de la thèse est une ébauche générale sur des systèmes étudiés. Après une brève revue du phénomène de cristallisation des polymères, nous décrivons le premier modèle structural du polymère semicristallin qui est le modèle de micelle à franges. Ensuite, nous présentons les principaux résultats des travaux de *Keller* qui a mis en évidence le phénomène de repliement de chaînes dans des cristaux polymères en utilisant la microscopie électronique à transmission.

De façon générale, la morphologie d'un monocristal polymère se distingue essentiellement par ses facettes latérales régulières et par son épaisseur uniforme. Les facettes du cristal correspondent aux plans cristallographiques ayant la vitesse de croissance la plus élevée et dépendent donc essentiellement des conditions de cristallisation. L'épaisseur du cristal présente elle aussi une forte dépendance par rapport aux

conditions de cristallisation, ce qui signifie que la morphologie semicristalline est largement déterminée par la cinétique. Il est à noter que le monocristal polymère dont la forme habituelle est une lamelle plane de quelques microns en largeur ayant une épaisseur nanométrique fond à une température plus basse comparée à un cristal infiniment épais. Cette dépression du point de fusion peut être décrite par l'équation de Gibbs-Thomson qui tient compte de l'énergie libre surfacique du cristal. Puisque les monocristaux polymères sont toujours en état métastable, il est parfois possible d'induire leur évolution structurale par un traitement thermique. Ainsi les cristaux polymères peuvent diminuer leur énergie libre en se réorganisant pour donner lieu à des lamelles plus épaisses. Les mécanismes proposés pour expliquer ce phénomène de réorganisation structurale impliquent le glissement des chaînes dans la phase cristalline.

En ce qui concerne la structure du polymère utilisé dans ce travail, la maille de PEO a une symétrie appartenant au groupe d'espace $P2_1/a$. La maille contient quatre chaînes qui ont une conformation hélicoïdale de type 7_2.

Les clichés de diffraction électroniques enregistrés a l'aide d'un microscope électronique à transmission montrent que

l'axe **c** de la maille est perpendiculaire à la surface basale de la lamelle. En plus, les facettes des cristaux sont parallèles aux plans 120 qui correspondent donc aux fronts de la croissance cristalline.

Le deuxième chapitre de la thèse est divisé en deux parties. La première partie est dédiée à la description des échantillons de copolymères à bloc utilisés et à la stratégie de préparation des monocristaux. La deuxième partie est dédiée à la description des dispositifs expérimentaux.

Les matériaux utilisés dans la présente étude sont des copolymères linéaires bi-séquencés de *polystyrène-bloc-poly(oxyde d'éthylène)* (PS-*b*-PEO). Ces copolymères ont une masse moléculaire moyenne allant de 6,500 à 30,000 Kg/mol pour le PEO et avec une masse moléculaire moyenne de 4000Kg/mol pour le PS. La préparation des monocristaux suit la stratégie menée par *Lotz* et *Cheng*, à savoir la méthode d'auto-ensemencement. Selon cette procédure, une solution diluée de copolymère est portée au-dessus de sa température de dissolution dans un solvant non-préférentiel pour les des deux blocs puis trempée dans un bain réglé à la température de cristallisation désirée. Ensuite la solution est de nouveau portée à une température T_s qui est légèrement en-dessous de

la température de dissolution pour laisser des germes a partir desquelles les monocristaux vont croitre à la température de cristallisation isotherme T_c pour produire des monocristaux uniformes en taille.

Comme mentionné plus haut, les deux techniques expérimentales essentiellement utilisées dans ce travail sont la l'AFM en mode contact intermittent et la diffusion des rayons-X. Les mesures AFM ont été réalisées avec un microscope MultiMode de VEECO couplé à un contrôleur Nanoscope IV. Le mode utilisé est le Tapping Mode. Le microscope MultiMode offre la possibilité de réaliser des mesures de recuit contrôlées à partir de la température ambiante et jusqu'au-delà de la température de fusion des monocristaux.

Les mesures de diffusion des rayons-X aux petits et aux grands angles ont été menées à l'ESRF de Grenoble. Les dispositifs disponibles sur les lignes BM26 et ID02 permettent de réaliser des mesures en temps réel avec une résolution temporelle d'une fraction de seconde.

Le troisième chapitre décrit la méthodologie de traitement de données AFM et SAXS.

Les images topographiques mesurées par AFM sont analysées en utilisant des histogrammes de hauteur calculés après une correction adéquate du fond de l'image. Ces histogrammes permettent d'évaluer l'épaisseur globale des monocristaux et suivre son évolution lors des expériences de chauffe.

Les clichés SAXS subissent une série de corrections avant d'y extraire des informations structurales. Tout d'abord, les clichées sont corrigés par la sensibilité du détecteur. Ensuite l'intensité parasite est soustraite et la norme du vecteur de diffusion est calibrée à l'aide d'une référence comme par exemple le behenate d'argent. Enfin, l'intensité du signal est corrigée par un facteur géométrique dit de Lorenz. L'application du modèle à deux phases permet de calculer la fonction de corrélation, ainsi que celle de la distribution des interfaces qui donnent des informations sur les épaisseurs cristallines et amorphes.

La fonction de corrélation uni-dimensionnelle (1D CF), ou $\boldsymbol{\gamma_1(r)}$, est calculée à partir de l'intensité diffusée par une transformé de Fourier. L'analyse de la fonction de corrélation donne accès à l'épaisseur cristalline et amorphe. La fonction de distribution des interfaces (IDF), ou $g_1(r)$, constitue une

autre approche pour analyser des systèmes à deux phases. Elle se calcule soit par une dérivée seconde de la fonction de corrélation ou par une transformée de Fourier de la fonction d'interférence. L'évaluation de la fonction IDF donne accès à aux épaisseurs cristalline et amorphe, ainsi qu'à leurs distributions.

Les chapitres quatre et cinq de la thèse présentent les résultats essentiels obtenus dans ce travail qui peuvent être résumés comme suit :

1. Nous avons démontré que les monocristaux formés par des copolymères contenant un bloc de PEO court ont une forme particulière dite de lentille. L'apparition des cristaux ayant cette forme a été attribuée à la polydispersité des copolymères qui se révèle lors de la cristallisation accompagnée par un fractionnement de chaînes. Une comparaison entre les distributions des épaisseurs lamellaires telles que déterminés par AFM et par SAXS montre un bon accord, y compris pour des monocristaux en forme de lentille.
2. Contrairement aux données de la littérature, nous n'avons pas réussi à visualiser la transition vers un état de chaînes de PS étirées en utilisant les lignes de cristallisation dans

les coordonnées de Gibbs-Thomson. Cela peut être du à la précision insuffisante de la technique SAXS. Néanmoins, il est aussi possible que les pentes de la ligne de cristallisation ne contiennent pas d'informations thermodynamiques telles que l'énergie surfacique de cristaux, ce qui est s'obtient facilement à partir de la ligne de fusion.

3. Les expériences sur les recuits thermiques des monocristaux de PS-*b*-PEO montrent que ces derniers s'épaississent lors des chauffes. L'épaississement est le plus prononcé pour des copolymères contentant des blocs de PEO longs.
4. Lors de l'épaississement thermique l'orientation des chaînes de PEO reste toujours perpendiculaire au plan basal des lamelles. Cela indique que le mécanisme de l'épaississement est la diffusion des chaînes à l'état solide, sans que les cristaux fondent et recristallisent.
5. En analysant l'épaississement lamellaire, nous avons trouvé que ce processus dépend nos seulement de la température mais aussi du temps. Par exemple les monocristaux de PS-*b*-PEO (40-150) ne s'épaississent pas lors des chauffes à des vitesses supérieures à 0.05 °C/min. Par contre, ils s'épaississent bien lors des chauffes à des vitesses beaucoup plus lentes. Nous en avons conclu que

le processus de l'épaississement se déroule en passant pas des états métastables.

6. L'évolution en fonction de la température de l'épaisseur lamellaire montre des discontinuités lorsque plusieurs épaisseurs cristallines coexistent.
7. Nous avons trouvé que l'épaississement lamellaire ne dépend pas fortement de l'épaisseur initiale car à la fin des chauffes les lignes de fusion des lamelles formées à des températures différentes se superposent.